# Towards a Quantitative Understanding of the Electrophysiological Role of Cardiac Fibroblasts

–

# Zu einem Quantitativen Verständnis der Elektrophysiologischen Rolle von Kardialen Fibroblasten

**Diploma Thesis**

presented by

**cand. phys. Bettina C. Schwab**

Institut für Biomedizinische Technik
Prof. Dr. rer. nat. Olaf Dössel

Institut für Theoretische Physik
Prof. Dr. rer. nat. Margarete Mühlleitner

Karlsruher Institut für Technologie

Nora Eccles Harrison Cardiovascular Research and Training Institute
Dr.-Ing. habil. Frank B. Sachse

University of Utah

2012

Supervisors:
Dr.-Ing. Gunnar Seemann
Dr.-Ing. habil. Frank B. Sachse

Eidesstattliche Erklärung

Hiermit erkläre ich an Eides statt, dass ich die vorliegende Diplomarbeit selbständig und ohne unzulässige fremde Hilfsmittel angefertigt habe. Die verwendeten Literaturquellen sind im Literaturverzeichnis vollständig angegeben.

Karlsruhe, den 09.03.2012

# Contents

# List of Figures

# List of Tables

# 1

# Zusammenfassung

Die rechnergestützte Modellierung des Herzens ist eine erfolgreiche Methode zur Untersuchung der kardiologischen Physiologie und Pathologie. In den letzten Jahrzehnten wurden eine Reihe von mathematischen Modellen der Myozyten (Herzmuskelzellen) entwickelt, um Erregungsausbreitung und Kraftentwicklung in Gewebemodellen nachzubilden. Die Einbindung anderer Zelltypen wurde nicht als notwendig angesehen, da Myozyten sowohl für die elektrische Erregung als auch für die Kopplung zur Kraftentwicklung verantwortlich sind. Myozyten sind untereinander elektrisch durch Gap Junctions verbunden und ermöglichen so gleichmäßige Erregungswellen über das gesamte Myokardium.

Im Herzen sind jedoch eine große Anzahl verschiedener Zellen vorhanden. Neben Myozyten sind der Anzahl nach auch Fibroblasten dominant. Fibroblasten sind Zellen des Bindegewebes und nehmen Rollen in der Wundheilung ein. Nach Verletzungen des Herzens, insbesondere beim Myokardinfarkt, können sie stark vermehrt sein. Durch die Vermehrung der Fibroblasten werden vermehrt weitere Teile des Bindegewebes gebildet, vor allem Kollagen. Man spricht hierbei von Fibrose. Vor allem im Zusammenhang mit einem Myokardinfarkt gilt Fibrose in der Medizin als starker Risikofaktor für ventrikuläre Arrhythmien, die oft tödlich verlaufen. Die genauen Mechanismen der Entstehung dieser Arrhythmien sind noch unbekannt.

Studien mit Zell-Kulturen haben gezeigt, dass Myozyten und Fibroblasten sowie Fibroblasten untereinander ebenfalls elektrisch über Gap Junctions verbunden sind. Dies legt den Verdacht nahe, dass diese Verbindungen auch im lebenden Organismus vorkommen und die Elektrophysiologie möglicherweise entscheidend beeinflussen können. Da Fibroblasten jedoch sehr dünn sind, ist die direkte Messung ihrer elektrischen Eigenschaften im lebenden Gewebe stark erschwert. Bisher gibt es nur Hinweise für eine in-vivo Kopplung von Myozyten und Fibroblasten durch Gap Junctions im Sinusknoten. Infarktsituationen wurden ebenfalls als mögliche Szenarien für Myozyten-Fibroblasten-Kopplung vorgeschlagen. Eine Vermehrung der Gap Junctions in fibrotischen Regionen wurde festgestellt; die genaue Lokalisierung von Gap Junctions auf der Fibroblastenmembran ist jedoch schwierig.

Verschiedene Modelle des kardialen Gewebes aus Myozyten und Fibroblasten wurden entwickelt, um die Einbindung der Fibroblasten nachzubilden. Hierfür wurden mathe-

matische Modelle der Fibroblasten entwickelt und an vorhandene Myozyten-Modelle gekoppelt. In diesen Modellen wurde ein großer Anteil der verwendeten Gewebeparameter lediglich geschätzt oder über einen sehr großen Bereich variiert. Quantitative experimentelle Daten über Volumenanteile von Fibroblasten, Myozyten und extrazellulärer Matrix, Leitfähigkeiten der verschiedenen Komponenten und insbesondere der Kopplung von Myozyten und Fibroblasten sind rar. Die in-silico Modelle zeigen weitreichende Folgen der Fibroblasten-Einbindung für den Fall von stark gekoppelten Fibroblasten mit einem hohen Volumenanteil im Myokardium. Aufgrund der Unsicherheit über diese Parameter ist die Aussagekraft der genannten Studien eingeschränkt.

Das Ziel dieser Arbeit ist es, die Kluft zwischen qualitativer experimenteller und quantitativer rechnergestützter Forschung zu verringern. Die quantitative Analyse konfokalmikroskopischer Aufnahmen soll genutzt werden, um realistische Parameter für in-silico Modelle zu extrahieren. Durch die Anpassung der Rechnermodelle an direkte experimentelle Evidenzen soll in Zukunft deren Aussagekraft vergößert und eine realistischere Abbildung des Einflusses von Fibroblasten erlangt werden.
In dieser Arbeit werden Modelle von Myozyten (des Hasen) und Fibroblasten vorgestellt und miteinander verglichen. Eine Evaluation der Myozytenmodelle führte zu einer Bevorzugung des Modells von Mahajan et al., da es die experimentellen Daten bei physiologischen und erhöhten Herzraten des Hasen am genauesten wiedergibt. Bei den Fibroblasten-Modellen wird die Verwendung eines aktiven Modells empfohlen. Hierbei stehen das McCannell et al. und das Sachse et al. Modell zur Verfügung. Die beiden Modelle beruhen auf den gleichen experimentellen Daten.
Verschiedene Gewebemodelle für die Einbindung von Fibroblasten wurden beschrieben. Hierbei fällt eine Tendenz zum Multidomain-Modell auf, das von Sachse et al. für Studien der Myozyten-Fibroblasten-Interaktion vorgeschlagen wurde. Es handelt sich um eine Erweiterung des häufig genutzten homogenen Bidomain-Modells: Zusätzlich wird ein intrazellulärer Raum der Fibroblasten eingeführt, der ebenfalls mit Hilfe einer Poisson-Gleichung für statische elektrische Felder beschrieben wird. Dieses Modell ist jedoch nur angebracht, wenn eine ausreichende elektrische Kopplung zwischen Myozyten und Fibroblasten bzw. zwischen Fibroblasten untereinander besteht. Weiterhin vernachlässigt es durch seine Homogenisierung die geometrischen Eigenschaften der Mikro-Struktur des Gewebes.

Im experimentellen Teil der Arbeit wurden mit Hilfe von Konfokalmikroskopie dreidimensionale Aufnahmen von kardialem Gewebe erstellt.
Hierfür wurden Biopsien aus den Ventrikeln von gesunden und infarktgeschädigten Hasenherzen genommen. Bei den Infarkt-Herzen wurden verschiedene Regionen berücksichtigt, die sich durch ihren Abstand zur Narbe unterscheiden. Die Biopsien wurden mit einem Kryostaten in Scheiben von 60–100 $\mu$m Dicke geschnitten. Von den erhaltenen Gewebeproben wurden nur jene aus der Mitte der Herzwand berücksichtigt. In einem Vorgang von drei bis fünf Tagen wurde das Labeling der Proben mit Fluoreszenzmarkern durchgeführt, um bestimmte Proteine und Strukturen abbilden zu können. Jeder der Marker hat einen spezifischen Absorptions- und Emissionsbereich, sodass eine parallele Aufnahme von bis zu vier Markern mit dem Konfokalmikroskop möglich ist. Diese Arbeit setzt sieben verschiedene Marker ein: 4',6-Diamidin-2-phenylindol (zur Identifikation der Zellkerne), Anti-Vimentin (zur Identifikation der Fibroblasten), Anti-Connexin 43

(zur Identifikation von Gap Junctions des Connexin 43 Typs), Anti-Connexin 45 (zur Identifikation von Gap Junctions des Connexin 45 Typs), Weizenkeimagglutinin (zur Identifikation des Extrazellulärraums), Anti-N-Cadherin (zur Identifikation des mechanischen Zusammenhalts zwischen Zellen) und $\alpha$-Anti-Aktin der glatten Muskulatur (zur Identifikation von Myofibroblasten). Verschiedene Kombinationen der Marker wurden verwendet, um alle wichtigen Korrelationen darstellen zu können.

Die hochaufgelösten Rohdaten der Konfokalmikroskopie wurden zunächst vorverarbeitet. Es wurde das Hintergrundrauschen subtrahiert und das Signal in tieferen Schichten exponentiell verstärkt, um Dämpfungsartefakte auszugleichen. Dekonvolution wurde eingesetzt, um die Auflösung der Aufnahmen um ca. einen Faktor zwei zu erhöhen. Hierfür war die experimentelle Bestimmung von Point Spread Functions, den Bildern von Punktquellen, notwendig. In dieser Arbeit wurde ein Verfahren entwickelt, um Cross-Talk in den Aufnahmen zu korrigieren. Hierbei handelt es sich um eine Vermischung der Signale verschiedener Aufnahmekanäle, verursacht durch Überlagerung von Absorptions- oder Emissionsspektren oder durch Cross-Reaktionen von Antikörpern während des Labelings. Die Methode beruht auf der Inversion einer linearen Abbildung.

Im Hauptteil der Arbeit wurden die vorverarbeiteten Aufnahmen quantitativ analysiert. Zunächst wurden die Volumenanteile von Fibroblasten, Extrazellulärraum und Myozyten bestimmt. Fibroblasten und Extrazellulärraum wurden über ein Schwellwertverfahren segmentiert. Der verbleibende Raum wurde Myozyten zugeordnet. Hierbei ergaben sich in gesundem Gewebe Volumenanteile von ca. 4,8 % für Fibroblasten, 19,0 % für den Extrazellulärraum und 76,2 % für Myozyten. Diese Werte entsprechen durchgängig dem Bereich von bisherigen Messungen, die auf anderen Methoden basieren. Im Infarktgewebe veränderten sich die Volumenanteile bis zu ca. 6,5 % für Fibroblasten, 24,7 % für den Extrazellulärraum und 70,2 % für Myozyten, abhängig von der Region. Im Allgemeinen entsprechen diese Resultate etwa den Erwartungen. Erstaunlich war jedoch der nur sehr geringe Anstieg des Fibroblastenvolumens im Infarktgewebe. Genaue Werte zum Vergleich dieser Parameter liegen in der aktuellen Literatur nicht vor.
Die Leitfähigkeit des Extrazellulärraums wurde auf Basis der gemessenen Weizenkeimagglutinin-Intensitätsverteilung mit Hilfe numerischer Berechnung elektrischer Felder bestimmt. Dabei wurde Voxeln, deren Intensitäten über einem Schwellwert (identisch mit dem Schwellwert für die Segmentierung) lagen, eine lokale Leitfähigkeit mit einem allgemein anerkannten Wert für die Leitfähigkeit von reiner extrazellulärer Flüssigkeit zugeordnet. Bei Voxeln mit niedrigeren Intensitäten wurde diese Leitfähigkeit proportional zur Intensität skaliert. Somit wurde der Intensität Null auch die Leitfähigkeit Null zugeordnet. An zwei gegenüberliegenden Seiten des Grauwertbildes wurden Elektroden mit hoher Leitfähikeit angefügt. Zusätzlich wurden dort Dirichlet-Randbedingungen für ein konstantes Potential definiert. Durch numerisches Lösen der zugehörigen Poisson-Gleichung mit Hilfe der Finiten-Elemente-Methode ergab sich die lokale Verteilung der extrazellulären Potentiale. Daraus konnte die Verteilung der Stromdichten berechnet werden, woraus sich auf die homogenisierte Gesamtleitfähigkeit des Extrazellulärraums schließen ließ. Dies wurde für alle drei Raumrichtungen durchgeführt, um einen Leitfähigkeitstensor und Anisotropieverhältnisse bestimmen zu können. Die longitudinale Leitfähigkeit in gesundem Gewebe lag bei ca. 0,264 S/m. Ein Vergleich mit experimentellen und anderen rechnergestützten Studien ergab eine gute

Übereinstimmung aller berechneten Werte in gesundem Gewebe. Für den Infarktfall konnte eine Erhöhung der longitudinalen Leitfähigkeit auf bis zu 0,400 S/m in einer Region gefunden werden. Insbesondere verringerte sich das Anisotropieverhältnis hier von 2,1 in gesundem Gewebe auf bis zu 1,3.
Die Verteilung von Connexin 43 auf Myozyten wurde mit Hilfe einer bereits publizierten Methode quantifiziert. Durch die kleine Anzahl der berücksichtigten Myozyten ist die Aussagekraft sehr gering. Es ergab sich jedoch eine deutliche Tendenz zu vermehrten lateralen Gap Junctions in gesundem und infarktgeschädigtem Hasengewebe. Dies steht im Gegensatz zur Verteilung der Gap Junctions auf Ratte-Myozyten.
Um die Kopplung von Fibroblasten durch Gap Junctions abzuschätzen, wurde die Verteilung von der Connexin 43-Dichte relativ zu Vimentin quantifiziert. Im Vergleich zur Connexin 43-Dichte fern der Fibroblasten-Membran ergab sich in gesundem Gewebe ein Abfall der Connexin 43-Dichte nahe der Fibroblasten-Membran, während im Infarktgewebe ein deutlicher Anstieg an gleicher Stelle zu erkennen war. Diese Häufing der Connexin 43-Dichte wird als Zeichen für eine Kopplung von Fibroblasten durch Gap Junctions gedeutet. Die Ergebnisse in gesundem Gewebe sprechen für eine geringe oder fehlende Kopplung. In den Bereichen nahe der Fibroblasten-Membran sind die Standardabweichungen der Daten gering.
In dieser Arbeit wurden keine funktionalen Parameter der Gap Junctions bestimmt. Ein berechtigter Einwand ist die fehlende Überprüfung der Funktionalität der detektierten Gap Junctions. Diese Überprüfung ist sehr aufwendig. In einem Versuch, das Labeling für Gap Junctions zu bestätigen und die Wahrscheinlichkeit für ihre Funktionalität zu erhöhen, wurde ein Labeling mit Anti-N-Cadherin durchgeführt. Eine hohe Kolokalisationsrate von Connexin 43 mit N-Cadherin zeigt, dass sich die detektierten Gap Junctions in einem mechanisch stabilen Umfeld befinden und damit eine wichtige Bedingung für ihre Funktionalität gegeben ist.
Connexin 45 wurde in der quantitativen Analyse vernachlässigt, da es in den untersuchten Proben nur in sehr geringem Maß vorhanden war. Im Infarktgewebe wurden einzelne kleinere Häufungen von Connexin 45-Signal im Zusammenhang mit Vimentin-Signal beobachtet. Dies spricht für eine Kopplung der Fibroblasten über Connexin 45, die jedoch nur selten vorzukommen scheint.
Ein Labeling mit $\alpha$-Anti-Aktin der glatten Muskulatur hat ergeben, dass in den betrachtenen Proben kaum Myofibroblasten vorhanden waren. Die durch Anti-Vimentin markierten Zellen werden somit den Fibroblasten zugeschrieben.

Die Beschränkung dieser Arbeit ist hauptsächlich im Bereich der Auflösung der Konfokalmikroskopie (ca. 400 nm nach Bildverarbeitung), der Funktionalität der Gap Junctions, des unspezifischen Labelings und besonders der geringen Anzahl an verwendeten Proben zu finden. Funktionelle Parameter, wie beispielsweise Leitfähigkeiten von Gap Junctions, wurden nicht bestimmt.
Eine ausführlichere Analyse mit umfangreicheren Daten ist für sichere Aussagen nötig. Insbesondere sollten Infarktherzen mit verschiedenem Alter des Infarkts verwendet werden, da es hier Hinweise auf deutliche Unterschiede in der Ausprägung der Veränderungen gibt.
Es wird erhofft, dass die berechneten Gewebecharakteristiken die Modellierung von kardialem Gewebe mit Fibroblasten verbessern und insbesondere quantifizieren können. Dadurch soll der möglicherweise pathologische Einfluss der Fibroblasten auf die Elek-

trophysiologie und Entstehung von Arrhythmien untersucht werden.
Eine direkte klinische Anwendung der beschriebenen Methode für die Quantifizierung von kardialem Gewebe ist denkbar, aber sehr aufwendig. Nach der Entnahme von Biopsien aus dem Herzen eines Patienten müssten die Proben über mehrere Tage präpariert werden. Die Rechenleistung der vorgestellten Methode ist nicht unerheblich und nicht für den personalisierten Gebrauch optimiert. Dennoch kann die Methode für eine detaillierte Diagnostik und personalisierte Therapieplanung richtungsweisend sein.

# 2

# Introduction

## 2.1 Motivation

Since Alan Hodgkin and Andrew Huxley developed a quantitative model of a squid giant axon in 1952 [1], the progress of computational cell models experiences a steady advancement, leading to more accurate and complex descriptions. During the past decades, several models of myocytes have been developed in order to reconstruct the electrophysiology of the heart. Myocytes are the cell types that both generate the electrical activation of the heart and do the mechanical work. Thus, other types of cardiac cells were not taken into account. Traditionally, other cell types such as cells of connective tissue and especially fibroblasts were neglected or merely seen as passive electrical barriers. However, fibroblasts are abundant in cardiac tissue. Their ratio by number to myocytes ranges between 0.5 and 2.4 [2], significantly larger ratios can be found in cardiac disease such as myocardial infarction (MI) [3]. In particular, the excessive formation of fibrous connective tissue after MI, fibrosis, is suspected to favor arrhythmogenic events [4].
It is well established that cardiac myocytes are electrically coupled by gap junction channels of low resistance. Studies of cell culture have shown that those connections also exist to fibroblasts and in-between fibroblasts [5]. Though, there is only evidence for in-vivo coupling between myocytes and fibroblasts for the sino-atrial node (SAN) [6]. Uncovering the effects of fibroblasts in cardiac tissue has been impeded because direct measurement of electrical coupling of fibroblasts in cardiac tissue in situ and assessment of the effects is difficult. A number of in-silico studies suggest various influences of fibroblasts on cardiac physiology [7, 8, 9, 10, 11, 12, 13] in case that this coupling should also exist in-vivo. Here, mathematical descriptions of cardiac fibroblasts have been worked out and applied in computational simulations to gain insights into electrical interactions between fibroblasts and myocytes. In these simulations, established mathematical models of ventricular myocytes have been electrically coupled to membrane models of cardiac fibroblasts.
The contribution of fibroblasts to cardiac electrophysiology is still not well understood and their role in cardiac diseases is controversially discussed. In-silico models suffer of a lack of quantitative experimental data. Many parameters have to be estimated or varied over large ranges, strongly affecting the results. It is therefore crucial to couple experiment and theory in order to develop a realistic in-silico model of cardiac tissue including fibroblasts. The basic understanding of myocyte-fibroblast interactions in the heart can lead to a better knowledge on potentially fatal ventricular arrhythmias during fibrosis. Pharmaceutical products might be developed to control pathological extents of this interaction.

## 2.2 Objectives and Organization

This work aims at establishing confocal imaging and quantitative image analysis as a basis for computational modeling of electrophysiology in normal and diseased cardiac tissue. Gaps in the provision of quantitative experimental data should be decreased. Special interest is drawn to fibroblasts and their relation to gap junction channels. Different in-silico models are introduced that can be appropriate to simulate the interactions between myocytes and fibroblasts.
In section 3, an introduction to cardiac physiology of cells and tissue is given. It also summarizes the pathologies that are important in this work: MI and fibrillation. The basic modeling of this electrophysiology is described in section 4. Present in-silico cell models of myocytes, fibroblasts as well as tissue models are introduced. It gives an overview of present computational modeling of cardiac tissue including fibroblasts. An overview of confocal microscopy and the processing of the observed images is given in section 5. Section 6 introduces the methods for this study. The main focus is the quantitative analysis of cardiac tissue, including the extraction of parameters for simulations. The results of this study are shown in section 7. Quantitative parameters for modeling studies are listed here and can directly be applied. A discussion of these results can be found in section 8, also including limitations of this study. Section 9 provides an outlook on future work in this field.
A major part of this thesis, mainly including confocal imaging, image reconstruction and quantitative analysis, has been submitted for publication [14].

# 3

# Cardiac Cells and Tissue

The heart of humans and animals has the function of maintaining blood flow through the vessels by periodic contractions and relaxations [25]. Its physiology and anatomy is complex, so research often concentrates on smaller parts of the heart and its function. This chapter describes the characteristics of cells and tissue in the ventricles. For a more detailed review of the physiology and anatomy of the whole heart, [25] is suggested as an appropriate introduction.

## 3.1 Tissue Architecture

Cardiac tissue is composed of various cells and fluids. The interstitial space between the cells is filled with fluid and an interconnected extracellular matrix comprised mostly of collagen [16, 17]. Capillary vessels are present in the whole myocardium.
Cardiac cells mainly consist of myocytes, fibroblasts, endothelial, vascular smooth muscle and neuronal cells. Myocytes and fibroblasts make up the majority with respect to cell number, myocytes dominate in their volume fraction; these cells are described in detail in sections 3.3.1 and 3.3.2. Other cell types are assumed to be comparably rare in cardiac ventricular tissue. Quantity, density, and morphology of cardiac cells vary significantly during development, amongst different species, for each type of cardiac tissue and in heart diseases [2, 18, 19].
Layered sheets of cardiac muscle cells are visualized in Fig. 3.1A in pink. The voids in-between are filled with un-labeled non-myocytes. Fig. 3.1B shows a confocal microscopic image of myocytes (in red), fibroblasts (in blue) and Cx 43 (Cx43) gap junctions (in green) in healthy rabbit ventricular myocardium. Fibroblasts are arranged in the clefts between myocytes [3].

## 3.2 Cell Electrophysiology

### 3.2.1 Cell Membrane and Ion Channels

The membrane of a cardiac cell is about 4-5 nm thick [20] and serves for separation of intra- and extracellular space [21]. It consists of a lipid bilayer and, depending on the cell type, different contingents of phospholipids, cholesterol and glycolipids. It is schematically shown in Fig. 3.2 [21].

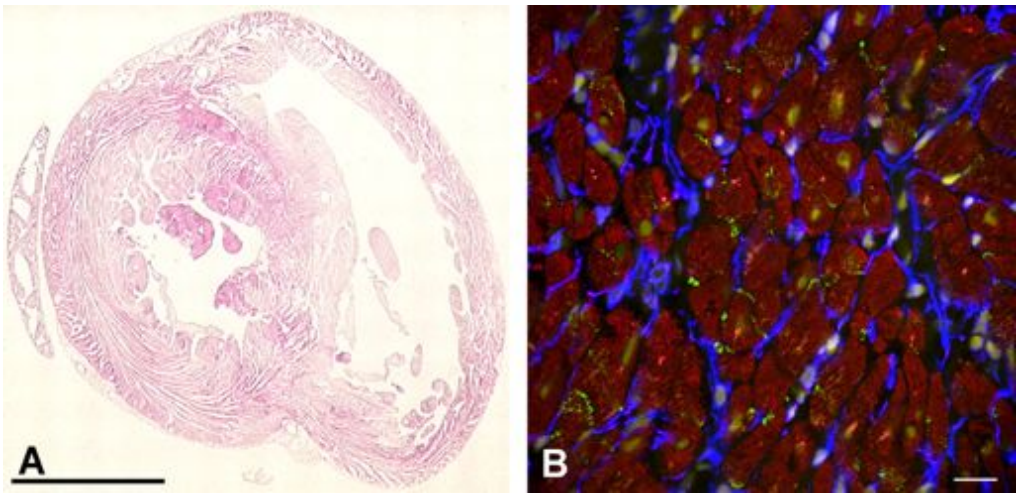


**Fig. 3.1.** The structure of cardiac tissue. (A) Transversal cross-section of gross histological view of rabbit ventricular myocardium showing layered sheets of cardiac muscle cells in pink, separated by voids that are filled with un-labelled non-myocytes. (B) Confocal microscopy tissue cross-section of larger magnification view of ventricular myocardium, myocytes labeled with anti-myomesin in red and fibroblasts labeled with anti-vimentin in blue, showing the dense network of fibroblasts that surrounds myocyte clusters of 2-4 cells. The bright green dots are Cx43 gap junctions, the pale yellow-green patches are nuclei labeled with DAPI (4'-6-Diamidino-2-phenylindole). Scale bars in A: 5 mm and B: 20 $\mu$m. Figs. from [3].

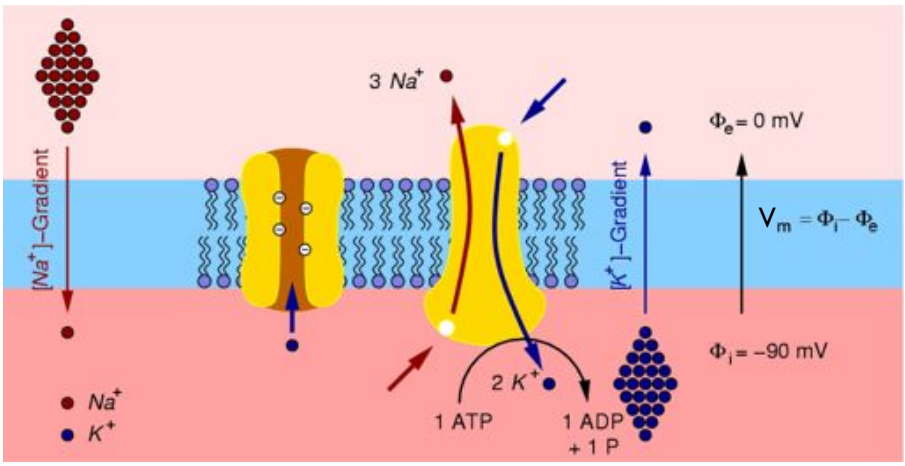


**Fig. 3.2.** Schematic of the cell membrane, membrane proteins (ion channels and ion pumps) and ionic concentrations for $K^+$ and $Na^+$. Fig. from [21].

The main characteristic of the cell membrane is its selectivity concerning ion passaging, which is regulated by different ion channels and pumps. Due to different ionic concentrations on the two sides of the cell membrane, intra- and extracellular space, an electric potential gradient and a transmembrane voltage ($V_m$) are present. Passive ionic currents seek to decompose this unbalance, whereas the pumps make ionic currents against the gradient possible. Without external influences, this leads to a dynamic equilibrium with a fixed $V_m$, the resting potential, which is about -80 mV for rabbit ventricular myocytes. The sign convention defines that the voltage is measured from intra- to extracellular space. This dynamic equilibrium of the membrane is described by the Goldman-Hodgkin-Katz equation:

$$E_m = \frac{RT}{F} ln \left( \frac{\sum p_I [I^+]_0 + \sum p_I [I^-]_i}{\sum p_I [I^+]_i + \sum p_I [I^-]_0} \right) \tag{3.1}$$

for the type of ion I. F is Faraday's constant, R is the Gas constant, $[I^{+/-}]_{o/i}$ is the extracellular/intracellular ionic concentration and $p_I$ are the relative membrane permeabilities for each ion. The reversal voltage $E_I$ of a specific ion is the membrane potential at which there is no absolute flow of this ion through the membrane. It is defined by the Nernst equation, which is equation 3.1 for only the specific type of ion:

$$E_I = \frac{RT}{F} ln \frac{[I]_o}{[I]_i} \tag{3.2}$$

The membrane itself can be described as a capacitor:

$$\frac{dV_m}{dt} = -\frac{I_{ion} + I_{stim}}{C_m} \tag{3.3}$$

$I_{ion}$ is the ionic current through the membrane, $I_{stim}$ the stimulus current and $C_m$ the capacitance of the cell.
Ion channels underlie gating mechanisms that let the channel open or close. Those pores have varied selectivities, i. e. their opening and closing mechanisms are dependent on different triggers, mainly $V_m$, specific ions and time. Channels are furthermore characterized by their kinetic and the maximum conductance in the open state. A voltage-gated ion channel is shown in Fig. 3.3 in the hyperpolarized and depolarized state [22].

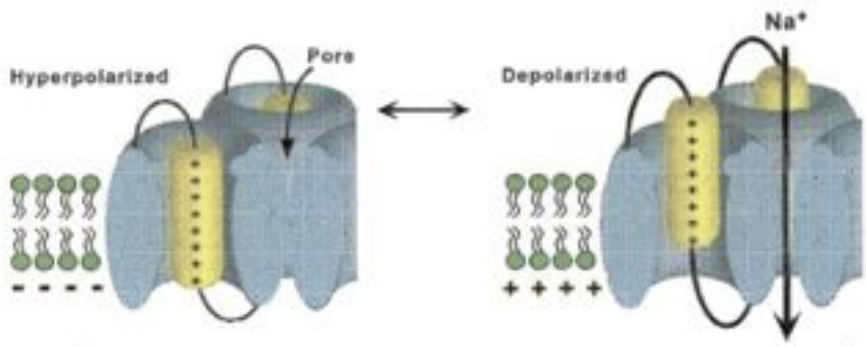


**Fig. 3.3.** Schematic of a voltage-gated ion channel in the hyperpolarized and the depolarized state. Fig. from [22].

In excitable cells (cells that are able to generate action potentials (APs), e. g. myocytes), voltage gated ion channels open after depolarization. Different channels open with distinct delays, which leads firstly to further depolarization, subsequently to an "overshoot" (positive $V_m$) and finally to repolarization. This course of the $V_m$ in dependence of time after sufficient depolarization is called AP and is shown in Fig. 3.4 [23].
Directly after the AP, no further AP or only a small AP can be initiated. These intervals refer to the absolute and the relative refractory period, respectively. This mechanism allows a controled excitation propagation as it prevents early re-excitation or re-entry. Normally, the channels become re-activated again when $V_m$ falls below a certain threshold

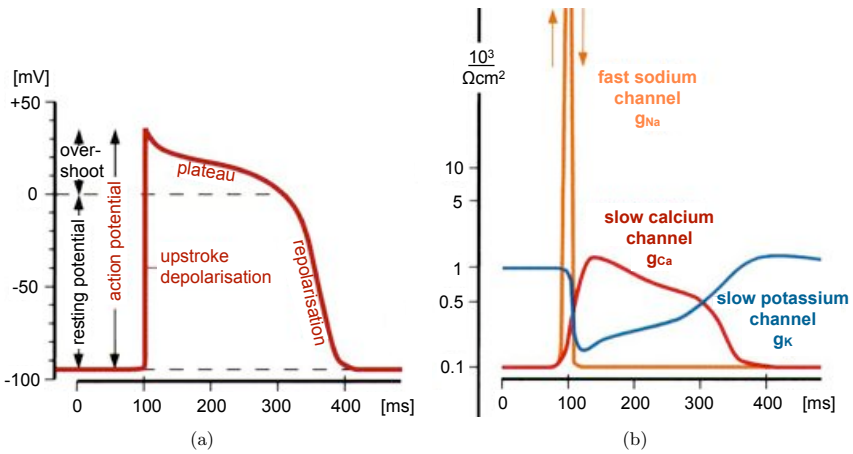


**Fig. 3.4.** (a) An example AP of the working myocardium. (b) Diagram of the mainly participating ion channel conductances responsible for the AP. Fig. from [23].

– this means, the refractoriness in healthy tissue is dependent on the action potential duration (APD). Fig. 3.5 illustrates absolute and relative refractory periods [24].

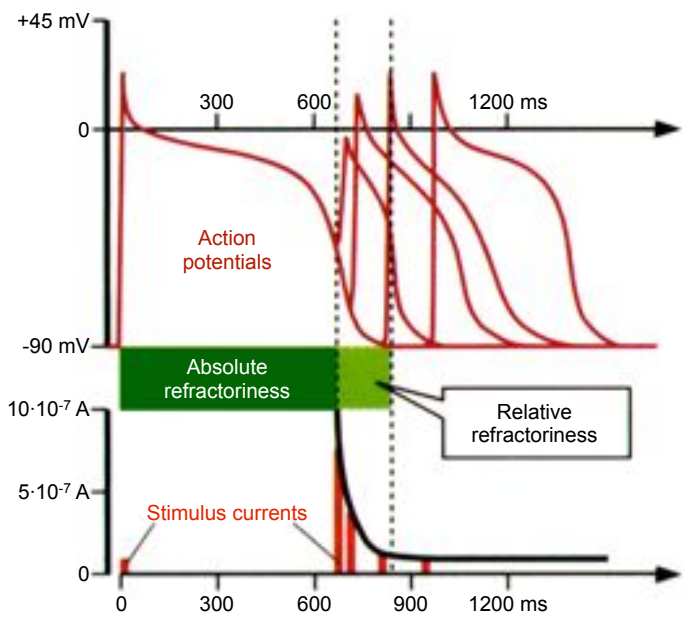


**Fig. 3.5.** Illustration of the absolute and the relative refractory period. High stimulus currents are needed to evoke an AP in the relative refractory period. No AP can be initiated in the absolute refractory period. Fig. from [24].

### 3.2.2 Gap Junctions

Myocytes and also other cell types are electrically coupled to each other by gap junctions. These are specialized proteins formed in a bundled manner with a low electrical resistance pore [25]. One important requirement for their functionality is the location in a mechanically stable environment, marked by the presence of N-Cadherin (NC). This is a glycoprotein that mediates calcium-dependent adhesion of cells [26].
Gap junctions have the form of cylinders or barrels with a length of 2–12 nm and a diameter of 1.5–2 nm, bridging a gap of 2–3 nm between two cells [25]. Smaller molecules like ions, nutrients and metabolites are able to pass the hydrophilic channel [27, 28].

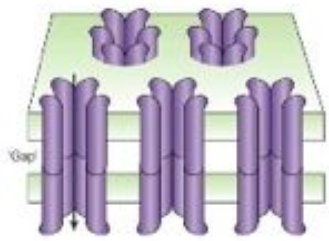


**Fig. 3.6.** Schematic of gap junction channel, formed by two connexons, each consisting of six Cxs. The arrow marks an axial channel, providing a direct connection between the adjacent cells. Fig. from [25].

Fig. 3.6 shows the schematic of gap junction channel. Two connexons, one from each cell, join at the gap of two adjacent cells and form the gap junction. Those connexons are made out of six connexins (Cxs). Cardiomyocytes are able to express three different types of Cx: Cx40, Cx43 and Cx45 [29, 30]. They form gap junction channels of potentially different conductance [5] and vary in their expression within the myocardium and especially during MI [30]. In ventricular tissue, Cx43 and Cx45 were found; Cx40 was only present in vascular endothelium [30]. Density and distribution of gap junctions also alter strongly with the tissue type and influence tissue specific characteristics like conduction velocity (CV) and anisotropy [31]. In healthy cardiac rat tissue, gap junctions were mainly found in the intercalated discs at the ends of cells, but also on their lateral sides [32].

## 3.3 Cell Types and their Interaction

### 3.3.1 Cardiac Myocytes

Myocytes account for 30 - 40 % of all cardiac cells and occupy about 75 % of tissue volume in the heart [3]. They contain actin and myosin for contraction. Therefore, myocytes are able to generate the electrical activation of the heart and do the mechanical work via a process called excitation contraction coupling [25].
Their length ranges from 50 to 120 $\mu$m, their diameter from 5 to 25 $\mu$m. In the adult heart, myocytes have a cylindrical shape and are mechanically as well as electrically coupled mainly at the intercalated discs at the cell ends [32, 33]. Gap junction distribution on the cell membrane of myocytes depends on their developmental stage [32]. In neonatal cells, Cx43 is relatively uniform distributed [34, 35]. In later stages, it progresses to a mature

condition where it is polarized at the intercalated discs [32, 36]. The distribution remodels to the sides of myocytes in aging tissue as well as during heart disease [37, 38, 39].
For the support with oxygen and nutrients needed for metabolism, each myocyte is linked to one or more capillaries [25]. The intracellular space consists mainly of the nucleus, mitochondria, the sarcoplasmic reticulum and myofibrils.
Myocytes in different regions of the ventricular myocardium differ with respect to electrophysiology, response to pharmacological agents, expression of pathologies and mechanical function [40].

### 3.3.2 Cardiac Fibroblasts

The majority of non-myocytes in cardiac tissue are fibroblasts, organized in a three-dimensional network [3, 41]. Their ratio (by number) ranges from 0.5 to 2.4, depending on species, tissue type and stage of development [2]. Besides myocytes, they form a predominant cardiac cell type, are the primary producer of myocardial extracellular matrix proteins [42] and contribute to electrical, biochemical, structural and mechanical proprties in the myocardium.
In cardiac tissue, fibroblasts can be found all-over the myocardium, surrounding myocytes and interconnecting neighbored myocardial tissue layers; in normal cardiac tissue, every myocyte is closely related to one or more fibroblasts. Though, fibroblasts are not only found interspersed with myocytes, but also forming islands consisting largely of connective tissue only [3].
A pathological increase of collagen due to fibroblast proliferation, so-called fibrosis, is observed in ischemic and rheumatic heart disease, inflammation, hypertrophy and infarction. Traditionally, one defines fibroblasts as cells of mesenchymal origin that produce interstitial collagen [3]. Nowadays, cell classification is usually based on morphological characteristics and proliferative potential. In general, fibroblasts tend to have sheet-like extensions or multiple processes. Fibroblasts are principally motile cells containing actin and myosin, but they are electrically inexcitable [43]. Normally, the fibroblast content increases with development and aging. The volume fraction of connective tissue reaches about 5 - 6 % in the normal adult myocardium and exceeds 50 % of the adult human sino-atrial node (SAN) [6].
Studies from animal coronary occlusion [3] show that fibroblast infiltration of damaged tissue occurred within hours of MI, playing a key role in healing processes. The density of fibroblasts increased with time after infarction and reached a maximum after one week. Fibroblast content increased even in remote tissue areas that were not directly affected by the infarct. In general, pathologies cause fibroblast proliferation and mobilization, and support their spread into apparently unaffected tissue [3]. Following MI, fibroblasts in the infarction scar can change their phenotype to the activated form myofibroblasts, having greater expression of contractile proteins and the ability to secrete different factors [44]. This phenotypic change also occurs in culture [45].
In the aged and hypertrophic heart, fibroblasts produce collagenous septa, which may act as a barrier for electrical conduction [3, 43]. Interstitial fibrosis and collagen accumulation are a relevant source of local anisotropy in ischaemia and hypertrophy, which enhances predisposition to cardiac arrhythmogenesis [46].
Cx occurrence in fibroblasts is dependent on the species [47]. In a study with isolated murine ventricular cells [48], fibroblasts were found to express both Cx43 and Cx45. Specific data for rabbit fibroblasts has not been found in the current literature.

### 3.3.3 Interactions between Fibroblasts and Myocytes

Fibroblasts seem to contribute to cardiac electrophysiology not only by acting as passive electrical insulators, but also by interacting with myocytes [49, 50, 51]. Electrical coupling of myocytes via gap junctions and electrical signaling through these, initiating contraction coupling of the heart, is well established in cardiology. In cell culture, electrical coupling via gap junction channels has also been reported between myocytes and fibroblasts as well as in-between fibroblasts [5, 44]. In the SAN, evidence for functional coupling in-situ is provided by immunohistochemical and confocal imaging studies [6]. Electrical coupling between myocytes and fibroblasts as well as in-between fibroblasts seems to be of lesser degree compared to in-between myocyte coupling, arising from gap junction channels of lower conductance [8]. In early studies of cell cultures from mouse and rat embryos, electrical coupling via fibroblasts was hypothesized to underlie synchronization of contraction among individual myocytes [52, 53].
Camelliti et al. [30] used a sheep coronary occlusion infarct model to detect the organization of cardiac myocytes and fibroblasts as well as changes in gap junction protein expression in confocal microscopic images during and after MI. They found various structural changes of cardiac micro-structure. Cx43 became redistributed from the intercalated discs to the lateral surface of structurally compromised myocytes within 12 days of MI. Cx45 expressing fibroblasts infiltrated the infarcted region within 24 hours. Later, Cx43 expressing fibroblasts were observed. Cx40 was only seen in vascular endothelium.
In 2006, Miragoli et al. studied the effect of fibroblast density on CV [54]. They found that CV was first increased and then decreased when fibroblast density was raised. Two years later, Zlochiver et al. demonstrated a reverse course of CV and detected increased vulnerability to reentry in two-dimensional tissue slices with an increased number of fibroblasts.
Miragoli et al. also showed in 2007 the ability of myofibroblasts to depolarize myocyte membrane potential sufficiently to facilitate automaticity [55].
In 2011, Baum et al. [56] investigated the coupling of myocytes and myofibroblasts in a dog MI heart by confocal microscopy. They did not find gap junctions between myocytes and fibroblasts.
Kohl and Camelliti [57] found colocalization of gap junctions and fibroblasts in their two-dimensional confocal images in 2012. In the rabbit ventricle, gap junctions colocalized to about 95.8 % with myocytes, to 7.4 % with fibroblasts and thus to 3.2 % with both. It is hard to state weather these colocalizations are a sign for coupling between myocytes and fibroblasts and/or in-between fibroblasts. With a resolution of about 1 $\mu m$ along the optical axis in 2D image slices without deconvolution, gap junctions cannot be allocated on a certain cell membrane.
Besides direct electrical coupling, other types of interaction between myocytes and fibroblasts have been proposed [51]. Those have been suggested to be signaling through components of the extracellular matrix or integrins, paracrine signals from fibroblasts impacting myocytes such as cytokines or growth factors as well as paracrine factors like calcium or adenosine-5'-triphosphate. Quantifying their influence on electrophysiology is hard – however, those interactions seem to be of much lesser degree compared to direct electrical coupling.

Contribution of fibroblasts to cardiac electrophysiology is still not well understood and their role in pathologies is controversially discussed. In particular in regions where myocytes are isolated by collagenous septa or scars, fibroblasts have been suggested to increase electrical coupling; other studies describe fibroblasts forming electrical bridges or current sinks, taking a malignant arrhythmogenic role. Direct measurement of electrical coupling between fibroblasts and myocytes in tissue in situ and assessment of its effects has been difficult.

## 3.4 Pathologies

In Germany, cardiac diseases are the most common cause of death [58] — a situation that can be found in the majority of industrialized countries in the world.
Several cardiac pathologies involve fibrosis, the excessive formation of fibrous connective tissue. Among them is MI (section 3.4.1). The increase of fibroblasts relative to other cells seems to be due to healing processes [59], but may influence cardiac electrophysiology in a pathological way and especially is suspected to favor arrhythmia [60].

### 3.4.1 Myocardial Infarction

MI reflects the pathological state of cardiac cell death due to prolonged ischaemia, caused by an interruption of blood supply to a region in the myocardium [61]. As such, MI is an acute coronary syndrome occurring during atherosclerosis [59]. Long-term coronary occlusion generally results in a progressive growth of the infarct region.
A schematic of an MI in the anterior region of the myocardium is given in Fig. 3.7 [62]. Blood supply is interrupted due to a blocked coronary artery, leading to death of myocytes and other cells in the affected region.

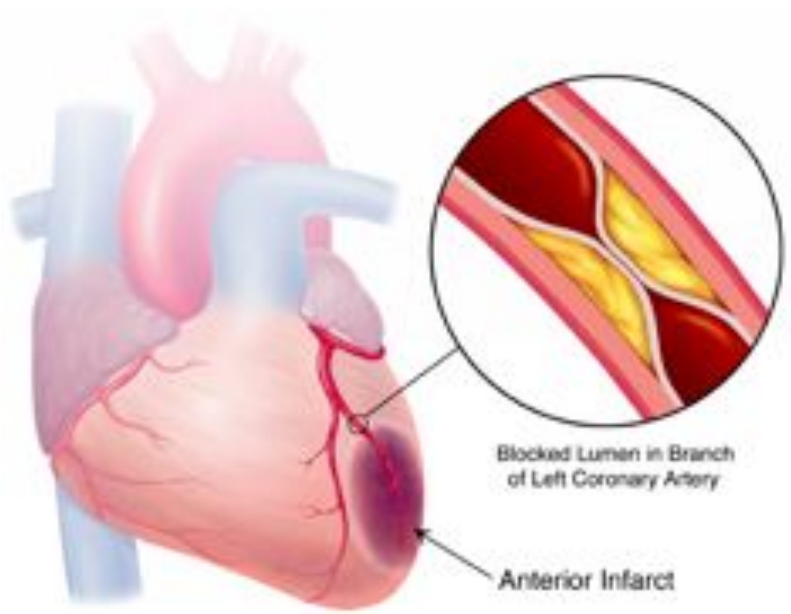


**Fig. 3.7.** Schematic of an MI in the anterior region of the myocardium. Blood supply is interrupted due to a barred coronary artery. Fig. from [62].

The acute phase of MI is characterized by the presence of polymorphonuclear leukocytes [63]. Infarction healing is characterized by the presence of fibroblasts and the absence of polymorphonuclear leukocytes. The entire process leading to a healed infarction usually takes at least 5-6 weeks, with the healed state manifested as scar tissue without cellular infiltration.
Structural remodeling of the marred myocardium may lead to adverse changes in myocyte electrophysiology due to alterations in their ion channels and changes in the extent and organization of the extracellular matrix [60]. Especially at the infarct border zone, the risk of arrhythmia is increased: within the epi-/endocardial border zone consisting of a thin sheet of surviving myocytes, the large number of fibroblasts beneath might slow conduction considerably.

### 3.4.2 Fibrillation

Ventricular Fibrillation (VF) is defined as a rapid, disorganized and asynchronous electrical activation and contraction of the ventricular muscle [64]. The heartbeat is frenzied and irregularly disturbed [65]. After a few seconds, this state may degenerate to asystole, the state of no cardiac electrophysiological activity.
Without treatment, VF may cause death due to undersupply of the body with blood. In the industrial world, this arrhythmia is the leading cause of sudden cardiac death. It is most often seen in patients with structural cardiac abnormalities or genetic defects [25].


**Fig. 3.8.** Experimental detection of fibrillation in a canine right ventricle. Electrodes were placed on the epicardium and detected the potential, in this image shown in different colors. The activation fronts are shown in pink. Spiral wave re-entry can be detected. Fig. from [66].

In the case of this pathology, multiple vortex-like ("re-entrant") waves of electrical excitation meander erratically through the ventricular muscle [67]. These rotors may occur during tachycardias [65]. Usually, progress begins with a more orderly stage, consisting of only one or a pair of spiral waves, but shortly breaking down into the multi-spiral disordered state of VF. This convulsive incoordination stage lasts for about 14-40 seconds. The individual waves in VF have short lifetimes, for which reason both the breakdown into

VF and the continued maintenance of it require a continual formation of new waves. This occurs in a process of wave break, splitting a single wave in two. Reasons for this wave break are either founded in pre-existing electrophysiological and anatomical heterogeneity or in dynamic heterogeneity arising from cardiac restitution properties. The restitution hypothesis states that large oscillations in APD cause wave break [66].
Fig. 3.8 shows the experimental detection of fibrillation in a canine left ventricle [66]. The measured potentials at each electrode on the epicardium are shown as colored points, the activation fronts are pink. Re-entry can be detected.
VF can exist as a stable state that is self-sustained and independent of the initiating event. This may be treatable by defibrillation, conducting an electrical current through the chest in order to depolarize all myocytes simultaneously. An alternative treatment may be antiarrhythmic agents.

# 4

# Modeling Cardiac Cells and Tissue

Computational models of cardiac electrophysiology aim to integrate multiple data sets into a consistent biophysical framework, encapsulating physiological understanding in order to provide quantitative predictions of the electrophysiological function [68].
In 1949, the computational reconstruction of cellular electrophysiology emerged with the model of Hodgkin and Huxley, describing the dynamic electrophysiology of a squid giant axon [1, 25]. In a seminal work of bringing together experiment and theory, they found a set of equations reconstructing the measured data. Most of the electrophysiological cell models in cardiology are based on those formalisms. A range of other cell models were developed with a view to reconstruct the electrophysiology of cell types in different species and regions of the heart, among them also the rabbit ventricular models of Puglisi and Bers [69] (section 4.1.1) and Mahajan et al. [70] (section 4.1.2). Those cell models seem in general to reproduce cardiac electrophysiology quite well (section 7.1.2); nevertheless, they are only an approximation of a complex biological system. Based on different experimental data and on different descriptions of the modeling equations, two models of the same cell type can differ strongly.
For fibroblasts, only a small number of model have been developed, and experimental data on their electrophysiology are rare (section 4.2).
The models need to be solved numerically, for example via the Euler method (most common), the Runge-Kutta method or the Rush-Larsen method.
For modeling the electrical flow in tissue, the cells need to be electrically coupled, considering the exchange of ions between adjacent cells. The bidomain model (section 4.3.1) consists of a homogeneous extra- and intracellular space. In the multidomain model (section 4.3.2), also the intracellular space of the fibroblasts is considered.
This chapter does not describe basic modeling of the cell membrane, gating kinetics, ion channels, pumps and exchangers. For an appropriate introduction see [25].

## 4.1 Models of Rabbit Ventricular Myocytes

Three current models of rabbit ventricular myocytes exist: The Mahajan et al. model (published 2008), the Puglisi-Bers model (published 2001) and the Shannon et al. model (published 2004). Since the models of Mahajan as well as Puglisi and Bers are most common and frequently applied, emphasis was focused on the description of these two models. The model of Mahajan et al. is supposed to replicate cardiac dynamics especially at rapid heart rates, whereas the Puglisi-Bers model is adapted to electrophysiology at

physiological heart rates. Fig. 4.1 shows the APs of the Puglisi-Bers model (green) and the Mahajan et al. model (red).
The models are adjusted to experimental data; nevertheless, they show significant differences. This is mainly due to a great variation of the measured data with region of the heart, temperature, rabbit age and experimentalist. Inclusion of different descriptions of the modeling equations may also have an effect.

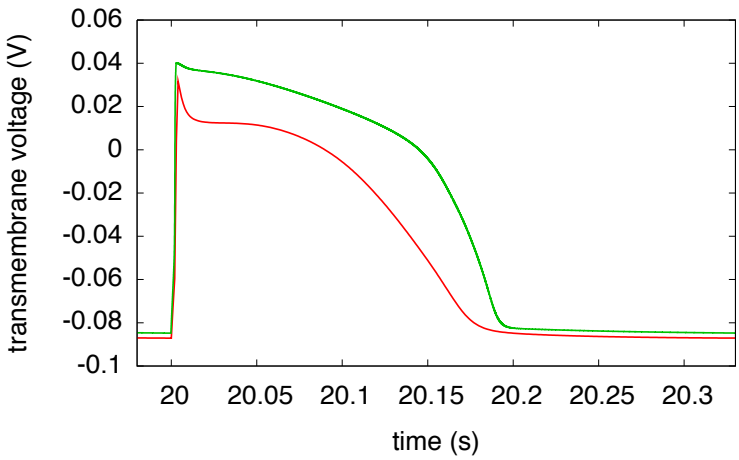


**Fig. 4.1.** APs calculated with the models of Puglisi-Bers (green) and Mahajan et al. (red) at a pacing cycle length of 333 ms and a precalculation time of 20 s.

### 4.1.1 Puglisi-Bers Model

For simulating the AP, ionic currents and $Ca^{2+}$ handling mechanisms of a rabbit ventricular myocyte, the Puglisi-Bers model has been developed in 2001 [69]. A schematic of the model is shown in Fig. 4.2.
The equations of the Luo-Rudy model [72, 73] were adapted to rabbit ventricular myoctes. A transient outward $K^+$ current ($I_{to}$) and a $Ca^{2+}$-activated $Cl^-$ current ($I_{Cl(Ca)}$) were included. The kinetics of the T-type Ca channel ($I_{Ca,T}$) and the rapid component of the delayed rectifier $K^+$ current ($I_{Kr}$) were modified. Several conductances were rescaled to correspond better to the results in the rabbit ventricle.
$I_{to}$ can contribute to ventricular repolarization. The formulation was taken from Winslow et al. [74]:

$$I_{to} = G_{to} X_{to} Y_{to} (V - E_K) \tag{4.1}$$

$$\alpha_{Xto} = 0.04561 \exp(0.03577V) \tag{4.2}$$

$$\beta_{Xto} = 0.0989 \exp(-0.06237V) \tag{4.3}$$

$$\alpha_{Yto} = 0.005415 \frac{\exp[-\frac{(V+33.5)}{5}]}{1 + 0.051335 \exp[-\frac{(V+33.5)}{5}]} \tag{4.4}$$

$$\beta_{Yto} = 0.005415 \frac{\exp[\frac{(V+33.5)}{5}]}{1 + 0.051335 \exp[\frac{(V+33.5)}{5}]} \tag{4.5}$$

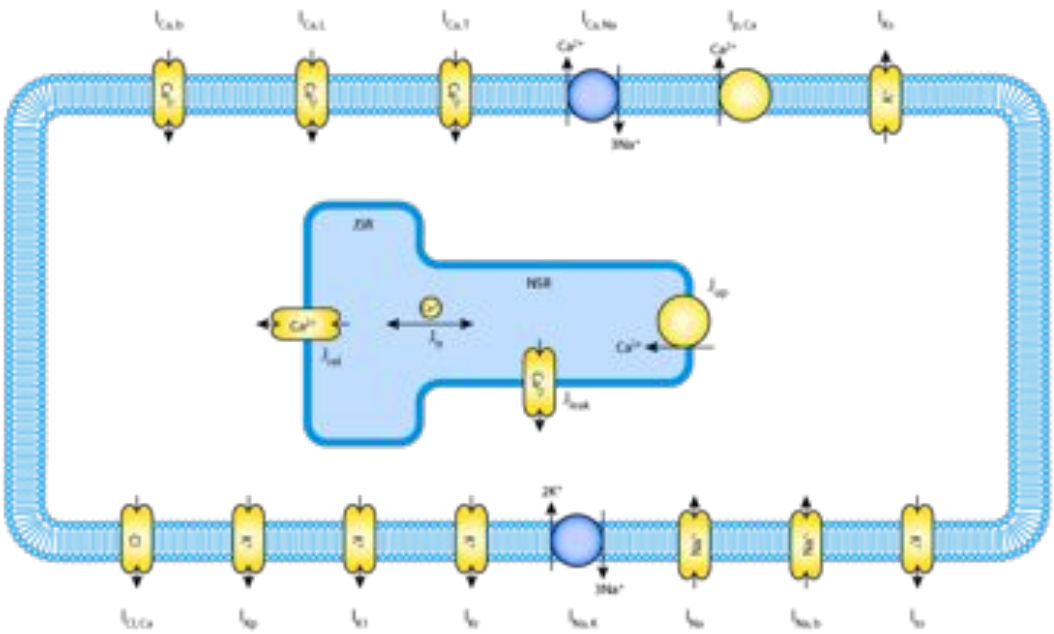

**Fig. 4.2.** A schematic diagram of the Puglisi-Bers rabbit ventricular myocyte model, describing the current flows across the cell membrane. Fig. from [71].

where $G_{to}$ is the channel conductance, $X_{to}$ is the activation parameter, $Y_{to}$ is the inactivation parameter and $E_K$ is the reversal potential for $K^+$.
$I_{Cl(Ca)}$ is modeled as

$$I_{Cl(Ca)} = G_{Cl}\frac{(V - E_{Cl})}{1 + \frac{K_{mCa}}{[Ca]_i}} \tag{4.6}$$

where $G_{Cl}$ is the Cl conductance (set to 10 mS/$\mu$F), $E_{Cl}$ is the reversal potential for $Cl^-$ and $[Ca]_i$ is the intracellular $Ca^-$ concentration. The $Ca^{2+}$ dependence is incorporated as a Michaelis-Menten factor with $K_{mCa} = 0.10\,\mu M$. The values were chosen to fit experimental records of Puglisi et al.
The $I_{Ca,T}$ equation was set to

$$I_{Ca,T} = L_{Ca,T}bg(V - E_{Ca}) \tag{4.7}$$

$E_{Ca}$ is the Nernst potential for $Ca^{2+}$ and the gating parameters are as follows:

$$b_\infty = \frac{1}{1+\ \exp[-\frac{(V+48)}{6.1}]} \tag{4.8}$$

$$\tau_b = 0.1 + \frac{5.4}{1+\ \exp[\frac{(V+100)}{33}]} \tag{4.9}$$

$$g_\infty = \frac{1}{1+\ \exp[-\frac{(V+66)}{6.6}]} \tag{4.10}$$

$$\tau_g = 8 + \frac{32}{1+\ \exp[\frac{(V+65)}{5}]} \tag{4.11}$$

These equations accurately reproduce the I-V relationship for $I_{Ca,T}$.
The kinetics of $I_{Kr}$ were modified as follows

$$I_{Kr} = G_{Kr} X R (V - E_{Kr}) \tag{4.12}$$

$$G_{Kr} = 0.02612\sqrt{\frac{[K]_0}{5.4}} \tag{4.13}$$

$$X_\infty = \frac{1}{1+\ \exp[-\frac{V+50}{7.5}]} \tag{4.14}$$

$$R = \frac{1}{1+\ \exp[\frac{V+33}{22.4}]} \tag{4.15}$$

$$\tau_X = \frac{1}{0.00138\frac{V+7}{1-\ \exp[-0.123(V+7)]}} + 0.00061\frac{(V+10)}{\exp[0.145(0.145(V+10))-1]} \tag{4.16}$$

All remaining parameters are identical to those in the Luo-Rudy model or only rescaled to fit better to the rabbit myocyte characteristics.

### 4.1.2 Mahajan et al. Model

The model of Mahajan et al. reproduces the dynamics of the cardiac rabbit AP and intracellular calcium ($Ca_i$) cycling at rapid heart rates [70]. A schematic of the model is shown in Fig. 4.3.
Using the rabbit ventricular AP model of Shannon et al. [75] as a platform, two key aspects were reformulated:

1. A minimal seven-state Markovian formulation of $I_{Ca,L}$, that reproduces Ca- and voltage-dependent kinetics
2. The dynamic $Ca_i$ cycling component of Shiferaw et al. [76]

*Markovian Formulation of $I_{Ca,L}$*

In general, a Markov model is a stochastic model following the Markov property. The Markov property determines the distribution for this variable: it depends only on the previous state. This is also called a memoryless process. The Markov chain, a simple Markov model, describes the state of a system with a random variable that changes through time. In the case of this cell model, every protein configuration is modeled by one state with transitions between the states.

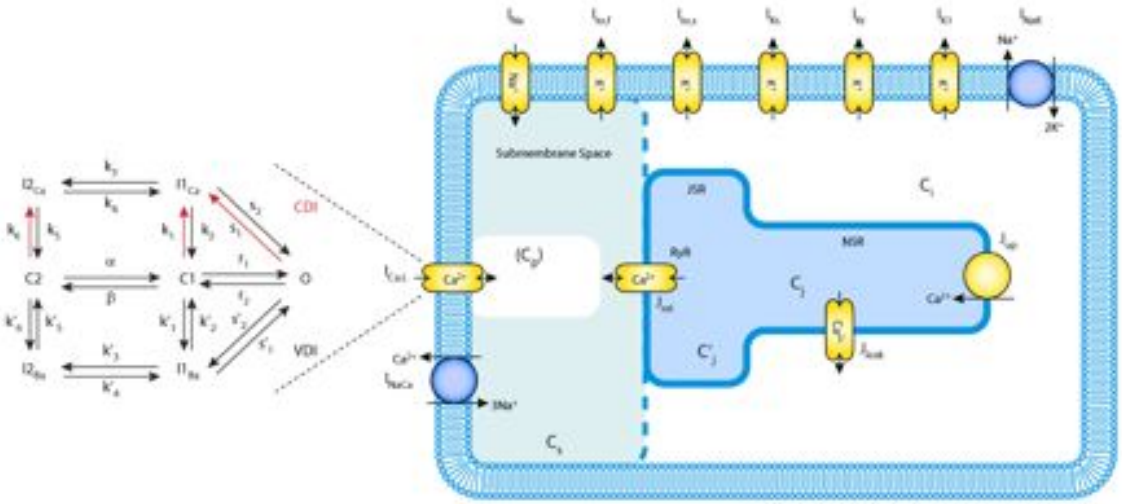


**Fig. 4.3.** Schematic diagram of the Mahajan et al. rabbit ventricular model, showing basic elements of membrane ion currents and Ca cycling machinery, as well as a Markovian model of the L-type Ca channel on the left. Fig. from [71].

The voltage dependence of activation is controlled by transitions between closed states as shown in Fig. 4.3. In this minimal Markovian model, it was found that two closed states (C1 and C2) were sufficient to model this effect, such that the transitions between C2 and C1 are strongly voltage-dependent.
The transitions from C1 to the open state O are voltage-independent and determine the steady-state open probability. Rate constants are adjusted so that the maximum open probability is roughly 5 %. Furthermore, there exist four inactivated states, split in two sets, depending on whether $Ca^{2+}$ is bound to calmodulin (CaM) (states $I1_{Ca}$ and $I2_{Ca}$) or not (states $I1_{Ba}$ and $I2_{Ba}$).
The inactivation of $I_{Ca,L}$ is modeled as occurring via two pathways, the voltage-dependent inactivation gate (VDI) and the Ca-dependent inactivation gate (CDI). With $Ba^{2+}$ as the charge carrier, inactivation occurs only via the VDI pathway, and a single time constant of inactivation is observed (Fig 4.3, states labeled with subscript Ba). When $Ca^{2+}$ is the charge carrier, two distinct time constants of inactivation, corresponding to VDI and CDI, respectively, are observed. According to this, the VDI and CDI components physically reflect channels in which $Ca^{2+}$ is not (VDI) or is (CDI) interacting with CaM.

*The $Ca_i$ cycling model*

The $Ca^{2+}$-induced inactivation of $I_{Ca,L}$ depends on $Ca^{2+}$ flowing through the pore of the channel as well as $Ca^{2+}$ released from the sarcoplasmic reticulum (SR).
To account for the complex spatiotemporal distribution of $Ca^{2+}$ during release from the SR, Shiferaw et al. [76] used a phenomenological approach to model the spatially averaged $Ca^{2+}$ concentrations within four different essential compartments of the cell (Fig. 4.3). This takes into account the recruitment of discrete release events ($Ca^{2+}$ sparks). Differential equations describe the average $Ca^{2+}$ concentration within each compartment separately.

*The AP model*

The two new formulations of $I_{Ca,L}$ and $Ca_i$ cycling were added to the model of Shannon et al. [75], tuned to replicate experimentally measured APD and $Ca_i$ transient properties. For describing $V_m$, the ordinary differential equation 3.3 is used. This leads to a system of 26 differential equations.

## 4.2 Models of Fibroblasts

Compared to models of myocytes, mathematical descriptions of fibroblasts are rare. Measurement of their electrophysiology is hindered, since fibroblasts have a thin and elongate shape.
Simple passive models describe the fibroblast membrane as a capacitor without active ionic channels or pumps (section 4.2.1). However, experimental studies in rat [77, 78] and human fibroblasts [79] suggest a number of ion channels - demanding for a more complex active model (sections 4.2.2 and 4.2.3).

### 4.2.1 Passive Models

Descriptions of fibroblasts as passive membranes have been used to incorporate the capacitive influence of fibroblasts on electrophysiology [10, 11, 80]. Here, no active currents through the membrane were taken into account. The models consist of a membrane capacitance and an ohmic resistance connected in parallel. Typical values for capacitance and resistance are 6.3 pF and 10.7 G$\Omega$, respectively [80].

### 4.2.2 McCannell et al. Model

Based on the passive model described in section 4.2.1, McCannell et al. developed an active model of fibroblasts including four ionic membrane currents [80]: a time- and voltage-dependent $K^+$ current ($I_{Kv}$), an inward-rectifying $K^+$ current ($I_{K1}$), an $Na^+$-$K^+$ pump current ($I_{NaK}$) and a background $Na^+$ current ($I_{b,Na}$).
$I_{Kv}$ has been found to be expressed in a large fraction of acutely isolated cardiac fibroblasts [77] and is modeled as

$$I_{Kv} = g_{Kv} r_{Kv} s_{Kv} (V - E_k) \tag{4.17}$$

where $E_k$ is -87 mV and $g_{kv}$, the maximum conductance of $I_{Kv}$, is 0.25 nS/pF. The activation parameter $r_{Kv}$ initially equals 0, the inactivation parameter $s_{Kv}$ initially equals 1. Their time dependence is given by

$$\frac{dr_{Kv}}{dt} = \frac{r_{Kv} - r_\infty}{\tau_r} \tag{4.18}$$

$$\frac{ds_{Kv}}{dt} = \frac{s_{Kv} - s_\infty}{\tau_s} \tag{4.19}$$

$\tau_r$ and $\tau_s$ were fitted to experimental data [77] and are merely dependent on the transmembrane voltage V:

$$\tau_r = 20.3 + 138 \exp\left(-\left(\frac{V + 20.0}{25.9}\right)^2\right) \tag{4.20}$$

$$\tau_s = 1574 + 5268 \exp\left(-\left(\frac{V + 23.0}{22.7}\right)^2\right) \tag{4.21}$$

The steady-state activation and inactivation parameters $r_\infty$ and $s_\infty$ are given by the following Boltzmann functions:

$$r_\infty = \frac{1}{1 + \exp\left(\frac{V+20.0}{11}\right)} \tag{4.22}$$

$$s_\infty = \frac{1}{1 + \exp\left(\frac{V+23.0}{7}\right)} \tag{4.23}$$

The majority of fibroblasts from the ventricles of adult rats express the $I_{K1}$ current [78]. To simulate this $K^+$ current in the fibroblast model, the ten Tusscher et al. [81] equation for this nonlinear inward-rectifying $K^+$ current was rescaled to approximate the much smaller capacitance.

$$I_{K1} = \frac{g_{K1}\alpha_{K1}(V - E_k)}{\alpha_{K1} + \beta_{K1}} \tag{4.24}$$

with the maximal conductance $g_{K1} = 482.2$ pS/pF and the voltage-dependent coefficients

$$\alpha_{K1} = \frac{0.1}{1 + \exp(0.06(V - E_k - 200))} \tag{4.25}$$

$$\beta_{K1} = \frac{3 \exp(0.0002(V - E_k + 100)) + \exp(0.1(V - E_k - 10))}{1 + \exp(-0.5(V - E_k))} \tag{4.26}$$

A $Na^+$-$K^+$ pump has neither been identified in cardiac fibroblasts nor in myofibroblasts. However, $K^+$ would seem to require this type of active transport. The pump current is modeled by the equation

$$I_{NaK} = \bar{I}_{NaK}\left(\frac{[K^+]_0}{[K^+]_0 + K_{mK}}\right)\left(\frac{[Na^+]_i^{(3/2)}}{[Na^+]_i^{(3/2)} + K_{mNa}^{(3/2)}}\right)\frac{V - V_{rev}}{V - B} \tag{4.27}$$

where $V_{rev}$ = -150 mV is the reversal potential of this electrogenic pump, and B = -200 mV is an empirically determined constant. The value $\bar{I}_{NaK} = 2.002$ pA/pF is the maximum current generated. $K_{mK} = 1.0$ mmol/L and $K_{mNa} = 11.0$ mmol/L are binding constants. To balance $Na^+$ efflux associated with $Na^+$-$K^+$ pump activity, a linear background $Na^+$ conductance was added to the model, leading to the current $I_{b,Na}$:

$$I_{b,Na} = G_{b,Na}(V - E_{Na}) \tag{4.28}$$

the leak conductance $G_{b,Na}$ is 0.0095 nS/pF, $E_{Na}$ is the Nernst potential for $Na^+$ ions.

### 4.2.3 Sachse et al. Model

To study the interactions between ventricular fibroblasts and myocytes, Sachse et al. developed a mathematical model of fibroblasts [43, 82]. It describes the transmembrane voltage and currents of fibroblasts on basis of electrophysiological and PCR studies of isolated ventricular cells from adult male rats. A diagram of the model is shown in Fig 4.4. Only active currents that have been measured in experiments, as well as an unspecific background current were included.

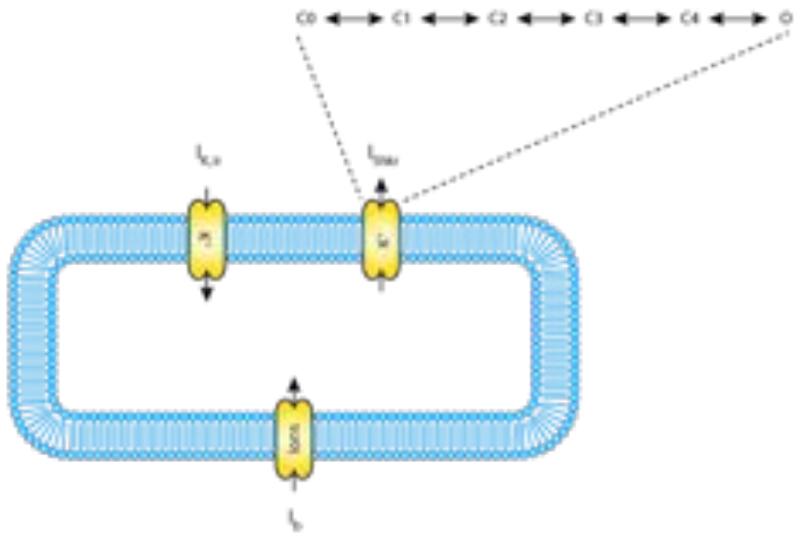

**Fig. 4.4.** Schematic diagram of the Sachse et al. rat fibroblast cell model. A Markovian formulation for the time and voltage dependent outward current ($I_{Shkr}$) is embedded within an electrophysiological cell model. Fig. from [71].

Two $K^+$ currents, an inwardly rectifying current $I_{Kir}$ and a time- and voltage dependent outward current $I_{Shkr}$, are major determinants of the fibroblast's voltage-current relationship. In this model, an unspecific background current $I_b$ responsible for maintaining the resting transmembrane voltage is introduced.
The fibroblast membrane has the membrane capacity $C_m$ and, as originally described by Hodgkin and Huxley [1], the transmembrane voltage $V_m$ is a function of the transmembrane currents:

$$\frac{dV_m}{dt} = -\frac{I_{Kir} + I_{Shkr} + I_b + I_{stim}}{C_m} \tag{4.29}$$

Experimental studies have shown that the inwardly rectifying current $I_{Kir}$ is nearly instantaneous and modulated by the external $K^+$ concentration. Channels consisting of Kir subunits are supposed to be the major carrier of this current. $I_{Kir}$ is described as follows

$$I_{Kir} = G_{Kir} O_{Kir} \sqrt{[K^+]_o}(V_m - E_K) \tag{4.30}$$

where $G_{Kir}$ is the conductance and $E_K$ is the reversal voltage. The channel open probability $O_{Kir}$ is defined as

$$O_{Kir} = \frac{1}{a_{Kir} + exp(b_{Kir}(V_m - E_K)\frac{F}{RT})} \tag{4.31}$$

with the constants $a_{Kir}$ and $b_{Kir}$. The Nernst equation 3.2 for $K^+$ defines the reversal voltage $E_K$.
The outward current $I_{Shkr}$ is assumed to be time- and voltage dependent. Measurements suggest that this current passes through channels consisting of subunits in the Kv 1.x family (Shaker). It is reconstructed based on the Goldman-Hodgkin-Katz current equations [83] and a Markovian model of delayed rectifier $K^+$ currents and its parameterization for shaker channels in neurons

$$I_{Shkr} = P_{Shkr} O_{Shkr} \frac{V_m F^2}{RT} \frac{[K^+]_i - [K^+]_o exp(-\frac{V_m F}{RT})}{1 - exp(-\frac{V_m F}{RT})} \tag{4.32}$$

where $P_{Shkr}$ is the permeability and $O_{Shkr}$ is the probability of the open state.
The Markovian model includes five closed states, $C0_{Shkr}$... $C4_{Shkr}$, and one open state $O_{Shkr}$ (Fig. 4.4):

$$\frac{\partial}{\partial t} C0_{Shkr} = -4k_v C0_{Shkr} + k_{-v} C1_{Shkr} \tag{4.33}$$
$$\frac{\partial}{\partial t} C1_{Shkr} = 4k_v C0_{Shkr} - (3k_v + k_{-v}) C1_{Shkr} + 2k_{-v} C2_{Shkr} \tag{4.34}$$
$$\frac{\partial}{\partial t} C2_{Shkr} = 3k_v C1_{Shkr} - (2k_v + 2k_{-v}) C2_{Shkr} + 3k_{-v} C3_{Shkr} \tag{4.35}$$
$$\frac{\partial}{\partial t} C3_{Shkr} = 2k_v C2_{Shkr} - (k_v + 3k_{-v}) C3_{Shkr} + 4k_{-v} C4_{Shkr} \tag{4.36}$$
$$\frac{\partial}{\partial t} C4_{Shkr} = k_v C3_{Shkr} - (k_o + 4k_{-v}) C4_{Shkr} + k_{-o} O_{Shkr} \tag{4.37}$$
$$\frac{\partial}{\partial t} O_{Shkr} = k_o C4_{Shkr} - k_{-o} O_{Shkr} \tag{4.38}$$

Both rate coefficients are dependent only on the transmembrane voltage and constants:

$$k_v = k_{v0} exp(\frac{V_m z_v F}{RT}) \tag{4.39}$$
$$k_{-v} = k_{-v0} exp(\frac{V_m z_{-v} F}{RT}) \tag{4.40}$$

with the coefficients $k_{v0} = k_v(V_m = 0mV)$ and $k_{-v0} = k_{-v}(V_m = 0mV)$. $z_v$ and $z_{-v}$ are the states between which the charge is moved. $k_o$ and $k_{-o}$ are constants.
The background current $I_b$ was described as in previous ohmic models of kidney and cardiac fibroblasts [84, 85].

$$I_b = G_b(V_m - E_b) \tag{4.41}$$

## 4.3 Models of Electrical Conduction in Tissue

Electrical conduction in cardiac tissue can be described by micro- as well as macroscopic models. A large number of cardiac cells require macroscopic modeling, since the computational effort of microscopic modeling (doing justice to the discrete distribution of gap junctions and discontinuity of electrical flow) is huge [86]. Those macroscopic descriptions model cardiac tissue as a functional syncytium and allow anisotropic excitation conduction in combination with electrophysiologically accurate ionic models (explained in sections 4.1, 4.2.3). More complex models are needed to include the influence of fibroblasts (section 4.3.2 and 4.3.3).

### 4.3.1 Bidomain Model

As explained, the discrete electrical interaction of the cells in tissue can be approximated by the continuous bidomain model [25, 87, 88, 89, 90, 91]. It was first described by Tung in 1978 [92].

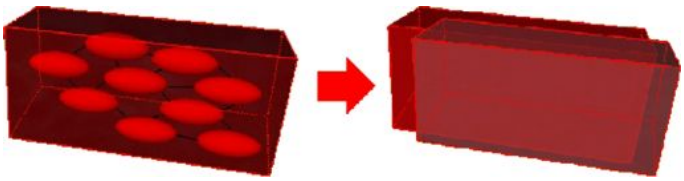

**Fig. 4.5.** Schematic of the bidomain model. Cells, connected via gap junctions, are embedded within the extracellular space. In the macroscopic approximation, both domains are assumed to be continuous. Fig. from [93].

Current flows in the two domains are considered independently, separated by the cellular membrane, which allows certain ionic currents to pass, according to the cell model. Therefore, the intercellular stimulus current driving the conduction of excitation takes into account influences of both domains.
To consider the anisotropic electrical properties of cardiac tissue and the ambient medium, for both the intra- and the extracellular domain a conductivity tensor is defined. The intracellular anisotropic conductivity tensor $\sigma_i$ is determined by distribution and density of gap junctions and the orientation of intracellular structures with respect to the myocyte orientation. The extracellular anisotropic conductivity tensor $\sigma_e$ reflects the conductivity of the extracellular fluid and its arrangement in tissue. All conductivity values are averaged over space to get a macroscopic anisotropy.
The bidomain model is based on Poisson's equation for stationary electrical fields (which can be derived by Maxwell's equations), describing the diffusion process for each domain during one time step:

$$\nabla(\sigma_e \nabla \phi_e) = -\beta I_m - f_{se} \tag{4.42}$$

$$\nabla(\sigma_i \nabla \phi_i) = \beta I_m - f_{si} \tag{4.43}$$

where the indices i and e stand for the intra- and extracellular domains, respectively, and $\phi$ is the accordant potential. $I_m$ is the transmembrane current density, $\beta$ the membrane

surface to cell volume ratio and $f_s$ the applied current sources.
The transmembrane voltage $V_m$ is defined by the potential difference of the two domains:

$$V_m = \phi_i - \phi_e \tag{4.44}$$

Due to the conservation of charge, $I_m$ vanishes in the summation of the two Poisson's equations

$$\nabla(\sigma_i \nabla \phi_i) + \nabla(\sigma_e \nabla \phi_e) = f_{si} - f_{se} \tag{4.45}$$

Assuming that no externally applied current sources exist ($f_{si} = f_{se} = 0$) and using 4.44, this leads to

$$\nabla(\sigma_i \nabla \phi_i) = -\nabla(\sigma_e \nabla \phi_e) \tag{4.46}$$
$$\nabla(\sigma_i \nabla (V_m + \phi_e)) = -\nabla(\sigma_e \nabla \phi_e) \tag{4.47}$$
$$\nabla((\sigma_i + \sigma_e) \nabla \phi_e) = -\nabla(\sigma_i \nabla V_m) \tag{4.48}$$

This equation describes the influence of the transmembrane voltage on the extracellular potential and is considered as the first part of the bidomain model. The second part consists of equation 4.43 and 4.44:

$$\nabla(\sigma_i \nabla \phi_i) = \nabla(\sigma_i \nabla (V_m + \phi_e)) \tag{4.49}$$
$$= \nabla(\sigma_i \nabla V_m) + \nabla(\sigma_i \nabla \phi_e) \tag{4.50}$$
$$= \beta I_m - f_{si} \tag{4.51}$$
$$= \beta \left( C_m \frac{dV_m}{dt} + I_{mem} \right) \tag{4.52}$$

where $I_m$ describes the overall flow through the membrane, determined by the cell model. The second part of the bidomain model, describing the intercellular stimulus current in dependence of intra- and extracellular space as an input for the electrophysiological models, is thus given by

$$\nabla(\sigma_i \nabla V_m) + \nabla(\sigma_i \nabla \phi_e) = \beta \left( C_m \frac{dV_m}{dt} + I_{mem} \right) \tag{4.53}$$

Cardiac tissue is usually modeled in a bath medium, e. g. in blood, to reconstruct realistic experimental conditions. In the bidomain model, bath and extracellular space build a continuous domain, but hold different conductivity tensors due to distinctions of the conduction properties. The bath is considered as isotropic and its conductivity gets a scalar value assigned. For considering different media, boundary conditions need to be included.

In case that $\sigma_i$ and $\sigma_e$ are linearly dependent, the computational effort can be reduced significantly. However, different anisotropies and bath loading effects cannot be considered. The model is then called monodomain model [25].

Models of these kinds do not take the a specific microstructure into account but see the tissue as a homogeneous continuum. Moreover, they hold the approximation of static electric fields, which is a good approximation for low frequencies of field changes with respect to the current densities, as in normal working myocardium.

### 4.3.2 Multidomain Model

Extending the bidomain model by a third domain, which is another intracellular space, leads to a multidomain model [8]. In the case of studying the influence of fibroblasts, the two intracellular domains are affiliated with myocytes and fibroblasts.

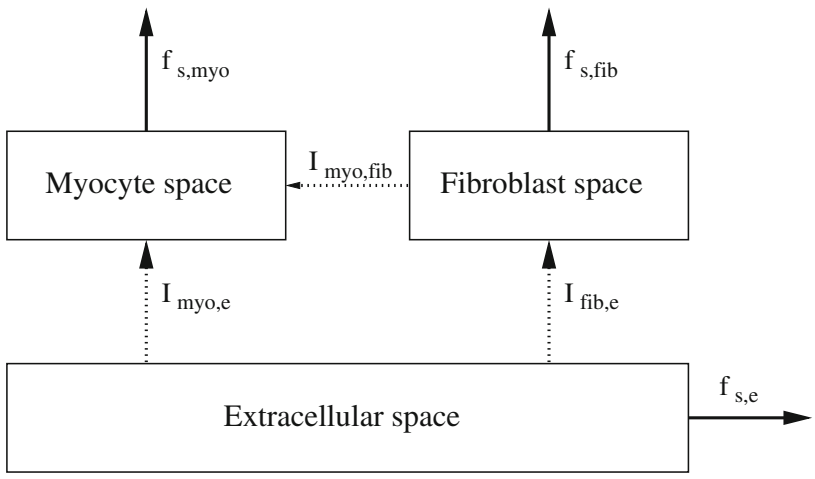


**Fig. 4.6.** Schematic of the multidomain model. It consists of two intracullarlar domains for myocytes and fibroblasts and an extracellular domain. Fig. from [8].

Fig. 4.6 shows the main ideas of the multidomain model. As in the bidomain model, each domain is described by Poisson's equation for fields of a stationary electrical current. For the intracellular space of the myocytes, equation 4.53 is used as a basis and a term considering the current flow from fibroblasts to myocytes is added:

$$\nabla(\sigma_{myo}\nabla\phi_{myo}) = -f_{s,myo} + \beta_{myo}I_{myo,e} + \beta_{myo,fib}I_{myo,fib} \tag{4.54}$$

where $\phi_{myo}$ is the intracellular potential of the myocytes, $\sigma_{myo}$ is the intracellular conductivity tensor, which lumps together conductivities of the myocyte interior and gap junction channels between the myocytes. $f_{s,myo}$ is the intracellular stimulus current source density, $\beta_{myo}$ is the myocyte per volume ratio, $I_{myo,e}$ is the transmembrane current of single myocytes, $\beta_{myo,fib}$ is the myocyte-fibroblast gap junction channels per volume ratio and

$I_{myo,fib}$ is the myocyte-fibroblast current per gap junction channel.
Analogous to that, the electrical field in the intracellular space of fibroblasts is defined as

$$\nabla(\sigma_{fib}\nabla\phi_{fib}) = -f_{s,fib} + \beta_{fib}I_{fib,e} - \beta_{myo,fib}I_{myo,fib} \tag{4.55}$$

$\phi_{fib}$ is the intracellular potential of the fibroblasts, $\sigma_{fib}$ is the intracellular conductivity tensor (lumping together conductivities of the fibroblast interior and gap junction channels between fibroblasts), $f_{s,fib}$ is the intracellular stimulus current source density, $\beta_{fib}$ is the fibroblast per volume ratio and $I_{fib,e}$ is the transmembrane current of single fibroblasts.
In the extracellular space, the electrical field is described in a similar way:

$$\nabla(\sigma_e\nabla\phi_e) = -f_{s,e} - \beta_{myo}I_{myo,e} - \beta_{fib}I_{fib,e} \tag{4.56}$$

with $\phi_e$ as the extracellular potential, $\sigma_e$ as the extracellular conductivity tensor (including intestinal and vascular spaces) and $f_{s,e}$ as the extracellular stimulus current source density.
The transmembrane currents $I_{myo,e}$ and $I_{fib,e}$ couple intra- and extracellular space:

$$I_{myo,e} = C_{myo}\frac{\partial V_{myo}}{\partial t} + I_{ion,myo} \tag{4.57}$$

$$I_{fib,e} = C_{fib}\frac{\partial V_{fib}}{\partial t} + I_{ion,fib} \tag{4.58}$$

where $C_{myo}$ and $C_{fib}$ are the membrane capacitors, and both $I_{ion,myo}$ and $I_{ion,fib}$ are the ionic currents (dependent of the transmembrane voltage).
The transmembrane voltages of myocytes and fibroblasts are defined as in the bidomain model:

$$V_{myo} = \phi_{myo} - \phi_e \tag{4.59}$$

$$V_{fib} = \phi_{fib} - \phi_e \tag{4.60}$$

The current $I_{myo,fib}$ through myocyte-fibroblast gap junction channels couples the two intracellular domains:

$$I_{myo,fib} = \frac{\phi_{myo} - \phi_{fib}}{R_{myo,fib}} \tag{4.61}$$

with gap junction channel resistor $R_{myo,fib}$.

### 4.3.3 Further Models of Tissue Including Fibroblasts

Computational studies have been performed in order to explore the effects of fibroblast-myocyte coupling by gap junction channels. In 1996, Kohl and Noble showed an increase of the spontaneous pacemaker rate due to fibroblasts by simulating a sinoatrial node pacemaker cell coupled to a single fibroblast [84]. This simulation consisted only of a myocyte and a fibroblast; no tissue structure was considered.

Jacquemet and Henriquez demonstrated in 2007 and 2008 that CV first increased and then decreased with increasing gap junction conductance between myocytes and fibroblasts [94, 95]. They used a two-dimensional micro-structural tissue model with fibroblasts attached to myocytes, developed to represent a monolayer culture of cardiac cells covered by a layer of fibroblasts.
On the other hand, Zlochiver et al. simulated in 2008 coupled fibroblasts inserted into a 2D layer of myocytes, showing that CV first decreased and then increased as the gap junction conductance increased, which agreed with their experimental observations [96]. Sachse et al. studied in 2008 and 2009 the effects of fibroblasts, inserted between myocytes, on CV in a one-dimensional monodomain cable and a two-dimensional multidomain model [8, 43], that has been described in section 4.3.2. The study suggests that fibroblast coupling becomes relevant for small intra-myocyte and/or large intra-fibroblast conductivity. Sachse et al. showed, using models of rat myocytes and fibroblasts, that coupling to fibroblasts has only a minor impact on the myocyte's resting and peak transmembrane voltage, but leads to significant changes of APD and upstroke velocity, as well as coupled fibroblasts reduce conduction and upstroke velocity [43]. In their simulations of plane waves, increased myocyte-fibroblast coupling and fibroblast-myocyte ratio reduced peak voltage and maximal upstroke velocity of myocytes. Also amplitudes and maximal downstroke velocity of extracellular potentials decreased.
In 2007 and 2008, Tanaka et al. and Zlochiver et al. showed the affection of wave breaks in two-dimensional tissue models by different fibroblast distributions [96, 97].
Using a passive fibroblast model, Xie et al. developed in 2009 computational models of two-dimensional tissue with fibroblast-myocyte coupling, indicating that fibroblast coupling elevates myocyte resting potential, causing CV to first increase and then decrease as fibroblast content increases, until conduction failure occurs [98]. Also, an enhancement of conduction by connecting uncoupled myocytes was detected. In this study, functional fibroblast-myocyte coupling prolonged the myocyte refractory period, which is suspected to facilitate induction of re-entry in fibrotic cardiac tissue. Xie et al. support the hypothesis that the cell models used do not have high impacts on coupling effects. They thus used passive cell models for fibroblasts and a simplified myocyte model.
Also in 2009, Maleckar et al. studied the effects of electrotonic coupling between human atrial myocytes and fibroblasts on myocyte excitability and repolarization [11]. Their model, consisting of one myocyte connected with a varying number of fibroblasts, shows that myocyte resting potential and AP waveform are modulated strongly by the properties and number of coupled fibroblasts, the degree of coupling and the pacing frequency. By using a passive and two different active models of fibroblasts, the hypothesis was supported that those effects change significantly with the used fibroblast model.
Based on the research of Malecker et al., Tveito et al. developed in 2011 a monodomain model in order to find out how conductivity and fibroblast density affect the stability of the solution [12]. They gave mathematical arguments for the nonexistence of a stationary solution for certain parameter choices. Numerical simulations also demonstrate that there is a region of instability. However, the monodomain model includes only coupling of a fibroblast to one myocyte and ignores coupling in-between fibroblasts. It also does not take account of loading effects in fibroblasts and the extracellular space.
McDowell et al. [13] investigated in 2011 the effects of myofibroblasts in an infarcted heart. They simulated a whole rabbit heart by using the monodomain model, including a fibroblast model in the myocyte model. The geometry of the scar and the whole heart

were segmented out of an MRI data set. Myofibroblast density was a determinant of the induction of arrhythmias.
To investigate the arrhythmic influence of fibroblasts and myofibroblasts, Nguyen et al. [99] coupled a rabbit ventricular myocyte electrotonically to a virtual fibroblast or myofibroblast in 2011. A promotion of early afterdepolarization due to fibroblasts or myofibroblasts was observed.
However, those studies do not take realistic, experimentally determined values of tissue parameters into account. Parameters were estimated or varied over a wide range. An exception is the study of Zlochiver et al. [96], which is based on optical mapping of cells in culture.

# 5

# Confocal Microscopy and Image Processing

Computational modeling needs to be based on experimental evidence. In particular simulations of tissue including fibroblasts experience a lack of data such as volume fractions of myocytes, fibroblasts and extracellular space as well as coupling and conductivity parameters. Confocal microscopy has the capability to image cardiac micro-structure in a sub-micrometer resolution and is therefore an appropriate tool to estimate a number of parameters in cardiac tissue (section 5.1). Labeling techniques are used to make certain components of the tissue visible (section 5.2). It is necessary to improve the quality of the data by image processing including deconvolution (section 5.3). In some cases in this work this is hindered because of cross-talk between the channels (section 5.4).

## 5.1 Confocal Microscopy

Confocal microscopy has the capability to image the 3D structure of biological tissues with sub-micrometer resolution [100, 101]. It is commonly applied to fluorescently labeled preparations, which allows identification of tissue compartments and cell types [102]. It enables studies even on living cells. However, it uses visible light with a spectrum of about 400 nm – 800 nm. The resolution without special additional techniques or image processing is thus strongly limited: for confocal microscopy, the lateral resolution $res_{lat}$ (orthogonal to the optical axis) is approximately [103]

$$res_{lat} = 0.4\frac{\lambda_{em}}{NA} \tag{5.1}$$

$res_{lat}$ depends on the numerical aperture NA of the lens. In the axial direction (along the optical axis), the resolution $res_{ax}$ is in general worse [103]:

$$res_{ax} = 1.4\frac{\lambda_{em}}{NA^2} \tag{5.2}$$

The specimen is marked with different fluorescent dyes. Excitation of electrons in the dye by externally applied light with the appropriate frequency leads to emission of light having a lower frequency (larger wavelength), which can be detected (Fig. 5.1). This phenomenon is called luminescence. In the case of fluorescence, the emission takes place immediately after excitation (about $10^{-7}$ s). The excitation and emission spectra are characteristic for each dye.

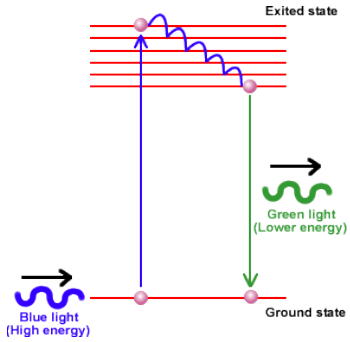


**Fig. 5.1.** The basic principle of fluorescence. Absorbed photons elevate electrons to a state with higher energy level. When relaxing to the primary state, the electrons each send out a photon having a lower frequency compared to the activating photon. Fig. from [104].

In confocal microscopy, a special construction is needed in order to detect only the light from one spot in the specimen (Fig. 5.2).

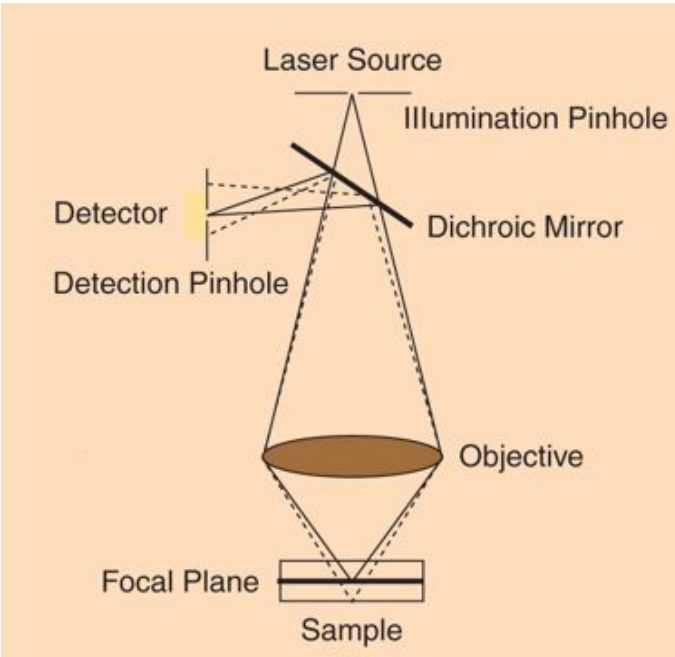


**Fig. 5.2.** The construction of a confocal microscope. Only light from a specific location is collected, avoiding the detection of blurred light. Fig. adapted from [105].

In most cases, laser light is used for the excitation, since the spectrum of laser light is very small. The light is focussed on a certain dot. Using a pinhole, light coming from other locations is suppressed for detection. This leads to a better resolution compared to widefield microscopy, especially in the direction of the optical axis. The high resolution is obtained at the cost of a low signal-to-noise ratio (SNR) in the image, since only light that passes through the pinhole is collected [105]. The SNR can be elevated by raising the laser power or the illumination time — however, this may lead to bleaching artifacts.
By focusing the excitation light iteratively at every spot in each plane, the three-dimensional image of the specimen is acquired.

One of the main characteristics of the imaging system in matters of a specific wavelength in confocal microscopy is the point spread function (PSF), which is the detected three-dimensional image of a point source. This image is usually not a point. The finite lens aperture introduces diffraction ring patterns in radial planes and phase aberration is present with symmetric features in radial planes and asymmetric features along the optical direction [105]. Fig. 5.3 shows a numerical calculation of a PSF in the meridional section (plane along the optical axis). The PSF in confocal microscopy has a prolate shape, whereas the one in wide field microscopy is closer to an "X" shape.
The three-dimensional PSF can be obtained experimentally, analytically and computationally. In the experimental methods, images of point-like objects (beads) are used to assess the PSF. They have the advantage that the PSF closely matches the experimental setup.

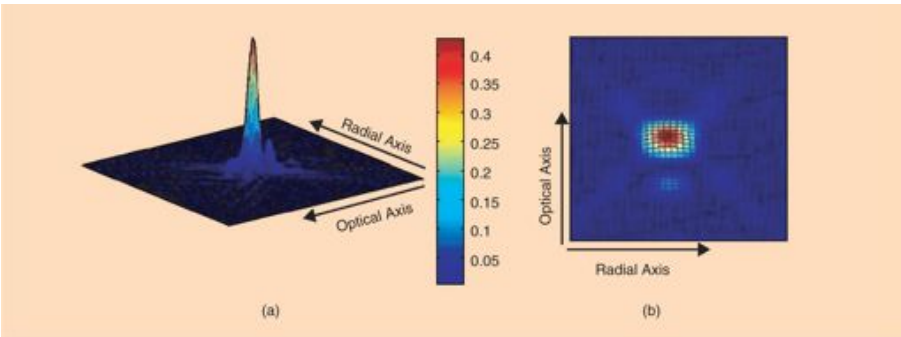


**Fig. 5.3.** A numerically calculated PSF. (a) Meridional section with the signal intensity represented by height. (b) Projected top view in the meridional section of the signal intensity. Fig. from [105].

The object (the specimen) and its image are mathematically related by an operation called convolution [106]. Assuming spatial invariance and linearity, the procedure of microscopy can be modeled as a linear shift-invariant system. Spatial invariance means, for every point of the object, the same PSF is measured, differing only in the location. Linearity expresses the predicate that the image of several points is the sum of their PSFs. During imaging, every point of the object is imaged by a blurred point. The object is convoluted with the PSF and, including noise, leads to the blurred image.
Deconvolution restores the image to an image with improved resolution and yields a better SNR by reassigning the blurred light to its origin [105] (section 5.3). Fig. 5.4 visualizes this process. The imaging process can be expressed analytically as

$$g(x, y, z) = f(x, y, z) \otimes h(x, y, z) + b(x, y, z); \quad x, y, z \in \mathbb{R} \tag{5.3}$$

where g(x, y, z) is the measured data, f(x, y, z) is the object, h(x, y, z) is the PSF and b(x, y, z) is the background noise.
Fourier transforming both sides of 5.3 leads to a linear transformation:

$$FT[g(x, y, z)] = FT[f(x, y, z) \otimes h(x, y, z) + b(x, y, z)] \tag{5.4}$$
$$= FT[f(x, y, z)] \cdot FT[h(x, y, z)] + FT[b(x, y, z)] \tag{5.5}$$

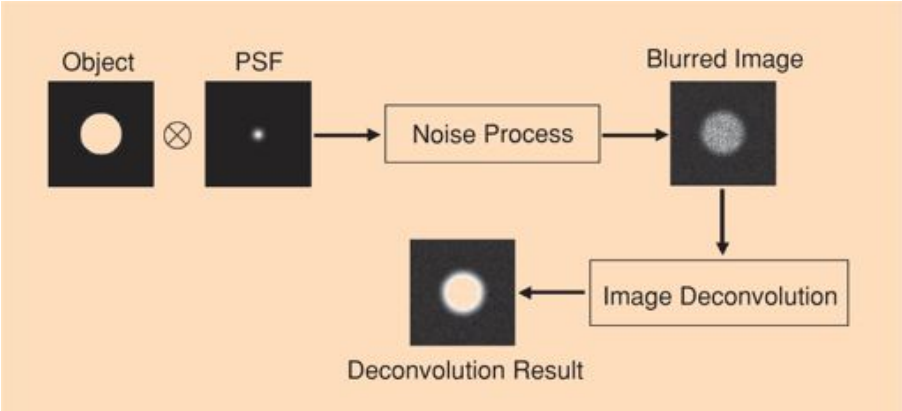


**Fig. 5.4.** Schematic of the general convolution and deconvolution process. In the convolution step, the object is convoluted with the PSF and (including noise) leads to the blurred image. Deconvolution seeks to rebuild the object by reassigning the blurred light to its origin. Fig. from [105].

## 5.2 Fluorescent Labeling

Different components of tissue are labeled with a dye having specific excitation and emission spectra. These spectra of excitation and emission should preferably not overlap and be constant with respect to excitation intensity, temperature and time. If the excitation or emission spectra overlap or there is a crossreaction of different dyes, this is referred to cross-talk [103].

For this work, four different methods of labeling are important [107, 108]:
– *Direct fluorochrome antigen binding* holds the idea that the fluorescent dye binds initially to the desired cell structure.
– *Fluorescent lectins* bind to sugar residues and are conjugated to the fluorescent dye.
– *Primary antibodies* bind to their specific antigen which is found in the cell component of interest.
– *Secondary antibodies labelled with fluorochromes* bind to the first (primary) antibody. Several secondary antibodies can bind to one primary antibody and therefore intensify the received signal.

Antibodies are specific with respect to antigen, host, type, subtype and chains. Normally, antibodies with different chains are mixed, and they are only characterized by antigen, host, type and subtype. The antigen is the protein to which the antibody binds, e. g. vimentin. The host specifies the species, in which the antibody was raised, e. g. mouse. Type and subtype define the immunoglobulin (Ig) itself and its function in immunology, e. g. IgG (type), IgG1 (subtype).
In the scope of this study, the following dyes were used: Wheat germ agglutinin (WGA), anti-vimentin, anti-Cx43, anti-Cx45, anti-NC, $\alpha$ smooth muscle anti-actin (anti-$\alpha$SMA) and 4',6-diamidino-2-phenylindole (DAPI). WGA is a lectin [109]. It detects glycoconjugates associated with the extracellular space and selectively binds to N-acetylglucosamine and N-acetylneuraminic acid (sialic acid) residues. It is available with fluorochromes of the excitation wavelengths 488 nm, 555 nm and 633 nm.
Anti-vimentin recognizes vimentin, one of the major groups of intermediate filament

proteins [110]. It localizes vimentin in fibroblasts, but also in lipocytes, endothelial cells, some lymphoid cells, melanocytes, macrophages and chondrocytes. The myocardium mainly shows vimentin in fibroblasts and endothelial cells. The used anti-vimentin is already bound to a fluorochrome that can be excited with a 555 nm laser, Cyanine3.18 (Cy3).
Anti-Cx43 binds to Cx43 and therefore recongnizes a prevalent type of gap junctions in the rabbit ventricle [111]. Different subtypes (IgG1 and IgM) were used in this work. Appropriate secondary antibodies can have any desired wavelength, but they need to be of the same subtype.
Anti-Cx45 targets a different type of gap junctions, composed of Cx45. Those gap junctions are also reported to occur in ventricular tissue [30], but seem to be rarer than gap junctions of the Cx43 type. Different conductances and gating behaviors are reported for the two types [112]. Only the subtype IgG1 is used here, requiring a secondary antibody of the same subtype with the needed wavelength.
Anti-NC locates NC in adherens juncitons of cells. It is responsible for the mechanical cohesion of the cells. Cadherins in general are calcium dependent cell adhesion proteins [113]. Colocalization of Cx and NC gives rise to a high probability of functional gap juncitons, since a stable mechanical environment is provided. Again, the subtype IgG1 is used, deciding the secondary antibody.
Anti-$\alpha$SMA recognizes $\alpha$SMA present in smooth muscle cells. In the myocardium, those are myofibroblasts and smooth muscle cells in vessels. It can therefore help to distinguish fibroblasts and myofibroblasts [114]. To avoid cross-reactions, the subtype IgG2a was chosen. The secondary antibody therefore also has to be IgG2a.
DAPI is a fluorochrome binding to the DNA and therefore stains nuclei of every cell type [115]. This labeling helps to discriminate cells from each other and gives evidence for the existence of smaller cells. Fibroblasts have in general one nucleus, whereas myocytes can have multiple nuclei.

In the labeling protocol, the incubation times, concentrations of the antibodies, lectins and fluorochromes as well as methods like rinsing, applying filters or addition of other substances are described. The protocols for this thesis can be found in the appendix A.

## 5.3 Deconvolution

In spite of detecting only light that passes the pinhole, the image in confocal microscopy is not free of blurred light and the PSF has a finite extension. Each point of a light wave, especially on a lens, can then be considered as a single light source that emitts a circular wave front. This is called Huygens' principle [103]. Therefore, when placing a screen after a lens, a diffraction pattern can be recognized. This results from interferences between adjacent waves. The pattern defines a two-dimensional diffraction figure, which consists of concentric rings alternating between light and dark. The first light disc is called the Airy disc.
The measured image is not only distored due to out-of-fokus light, but also because of spatial fluctuation of illumination in the specimen, excitation generated by the lamp flicker, attenuation of areas in the image because of self absorption, bleaching effects, geometrical effects and a Poisson noise originated by the background photon emission

[105].
Reconstruction of the original data seeks to invert the process of convolution during imaging (described in section 5.1). Due to several effects, this is impeded and limited [116].
Primarily, the background noise b(x,y,z) cannot be neglected as a significant poisson noise is present. This noise is higher than in wide-field microscopy because of a very little spot in the sample being excited and emitting light. Small numbers of detected photons lead to an increased relative standard deviation, thus noise.
Moreover, the PSF is estimated by measurement, which itself causes mistakes like misalignment or translation invariance.
Furthermore, it is not possible to reconstruct higher frequencies that were not detected due to the limited sampling rate.

Algorithms for deconvolution are for example based on Fourier filtering, least-squares regularization or Bayesian interference.
In this work, a Bayesian-based iterative method of image restoration, the Richardson-Lucy algorithm [117], is used. This Bayesian method searches for the most likely state of the original image, given the measured image and the PSF. A Poisson distribution for the detection of photons is assumed.
Bayes' theorem gives a relation between the probability for the state f given the state g, P(f|g), and the probabilities for f and g, P(f) and P(g):

$$P(f|g) = \frac{P(g|f) \cdot P(f)}{P(g)} \tag{5.6}$$

For the case of deconvolution image data, f is the original image and g the measured (blurred) image.
Light emission can be seen as a Poisson point process with the general description for the probability of an event

$$P_\lambda(X = k) = \frac{\lambda^k}{k!} exp(-\lambda) \tag{5.7}$$

with the randomized variable X underlying the Poisson process, $\lambda$ the value of expectation (and also the variance) and a natural number k.
Including the Poisson process (equation 5.7) in Bayes' theorem (equation 5.6) yields

$$P(g|f) = \prod_x \frac{(f \star h(x)\Delta x)^{(g(x))}}{g(x)!} exp(-(f \star h(x)\Delta x)) \tag{5.8}$$

being $\Delta$ x one volume element and h(x) the PSF.
Given the measured image g and the PSF f, we seek to reconstruct the original image f. The Maximum a priori estimate now searches for the original image f leading to a maximal probability P(f | g), thus the most likely f. Since P(f) and P(g) are assumed to be known, also a maximization of P(g | f) is possible.

This maximization is in this work performed iteratively with the Richardson-Lucy algorithm [117]:

$$f_{n+1} = f_n \frac{g}{f_n \star h} \otimes h \tag{5.9}$$

where $\otimes$ is the cross-correlation operator. The initial state of $f_n$ needs to be estimated.

## 5.4 Cross-Talk

Spectra of excitation and emission of fluorescent dyes should be as small as possible. The spectra of two different dyes should not overlap - otherwise, it is not immediately possible to separate the signals of the referring channels. Sometimes, the separation of spectra does not work properly due to large spectra of emission or excitation or certain imaging conditions, and so-called cross-talk between the channels is available. A cross-reaction of dyes during labeling can cause a similar phenomenon.
Fig. 5.5 visualizes bleed-through in different occurrences.

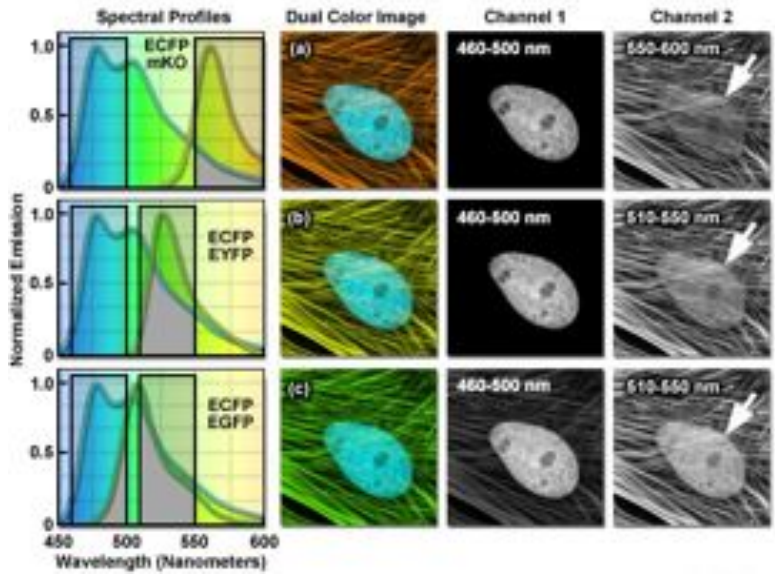


**Fig. 5.5.** Visualization of cross-talk due to overlap of the emission spectra. (a) Slight overlap of the spectra. Whereas the first channel shows only the desired dye, in the second channel parts of the unwanted dye are visible. (b) Significant overlay of the spectra. The first channel still shows only the desired dye, the second channel shows clearly both dyes. (c) High overlap of the spectra. Both channels show both dyes due to inseparable spectra. Cross-talk from both channels to each other is available. Fig. adapted from [118].

Mathematically, one can describe the process of imaging as a linear transformation.
Being $I_1$, $I_2$, $I_3$ and $I_4$ the measured fluorescence intensities of channel 1 to 4 as well as $C_1$, $C_2$, $C_3$ and $C_4$ the concentrations of the four corresponding dyes, the relation between them can be described as

$$\begin{bmatrix} I_1 \\ I_2 \\ I_3 \\ I_4 \end{bmatrix} = \begin{bmatrix} w_{11} & w_{12} & w_{13} & w_{14} \\ w_{21} & w_{22} & w_{23} & w_{24} \\ w_{31} & w_{32} & w_{33} & w_{34} \\ w_{41} & w_{42} & w_{43} & w_{44} \end{bmatrix} \begin{bmatrix} C_1 \\ C_2 \\ C_3 \\ C_4 \end{bmatrix} + \begin{bmatrix} B_1 \\ B_2 \\ B_3 \\ B_4 \end{bmatrix} \tag{5.10}$$

where $B_1$, $B_2$, $B_3$, $B_4$ is the baseline caused by the background. The measured intensity of each of the four wavelengths is a linear combination of the contributions from four dye concentrations. W = $(w_{ij})$ is called weight matrix or cross-talk matrix. If cross-talk is present, non-diagonal elements of the matrix are available.
Cross-talk correction has the aim to reconstruct the original dye concentration or a multiple of it. This is done by inverting the cross-talk matrix and requires the determination of the latter.
For the special case of singly cross-talk e. g. from channel 2 to channel 1, the transformation is reduced to

$$\begin{bmatrix} I_1 \\ I_2 \end{bmatrix} = \begin{bmatrix} w_{11} & 0 \\ w_{21} & w_{22} \end{bmatrix} \begin{bmatrix} C_1 \\ C_2 \end{bmatrix} + \begin{bmatrix} B_1 \\ B_2 \end{bmatrix} \tag{5.11}$$

# 6

# Methods

A main part of the present work is the new methodology, which is described in this section. The focus are the approaches for quantitative analyses, described in section 7.3.
Tissue preparation, sectioning, fluorescent labeling, image acquisition, general image processing as well as the assessment of Cx43 distribution on myocytes summarized here have already been described in literature and are widely recognized. The methods for cross-talk correction, estimation of PSF size, segmentation, estimation of extracellular conductivity and assessment of Cx43 distribution on fibroblasts have been developed within the scope of this work.

## 6.1 Tissue Preparation and Sectioning

Tissue was obtained from adult New Zealand White rabbits (2.5 kg) by Natalia Torres, CVRTI. The animals were anesthetized with an intravenous administration of sodium pentobarbital (50 mg/ml). The heart was excised quickly and the aorta cannulated. The heart was retrograde perfused with a $Ca^{2+}$-free HEPES-buffered saline solution containing (in mmol/l): 4.4 KCl, 128 NaCl, 5 $MgCl_2$, 1 $CaCl_2$, 22 dextrose, 24 HEPES, 20 taurine, 5 creatinine, 0.5 Na-pyruvate (pH 7.2 with NaOH). After 5 minutes, the solution was changed to an identical solution including WGA at a concentration of 50 $\mu$g/ml. After 15 minutes, a $Ca^{2+}$-free HEPES-buffered saline solution containing 2 % of paraformaldehyde (PFA) was used. Finally the heart was removed and submerged in that solution for additional 20 minutes, and stored at 4°C in phosphate buffered saline (PBS) with 30 % sucrose and 0.05 % azide. This procedure was performed with two types of animals, a control group and an MI group. The MI in the latter group was caused by ligation of the circumflex artery [119].
Fig. 6.1 shows the processes of taking biopsies and sectioning. In the healthy hearts, round shaped biopsies with a diameter of 5 mm were taken from the middle of the left ventricle. Several biopsies in different distances from the scar were taken from the infarcted hearts. All biopsies were frozen at -24°C in tissue-freezing medium (Triangle Biomedical Sciences, Durham, NC). Immediately after freezing, the biopsies were sectioned in slices of 80–100 $\mu$m using a cryostat (Leica CM1950, Wetzlar, Germany). Tissue sections were produced parallel to the epicardial surface. Serial sections were obtained through the entire thickness of the ventricular wall. Division into three groups specified epicardial, mid-myocardial, and endocardial sections. Only mid-myocardial sections were characterized in this work.

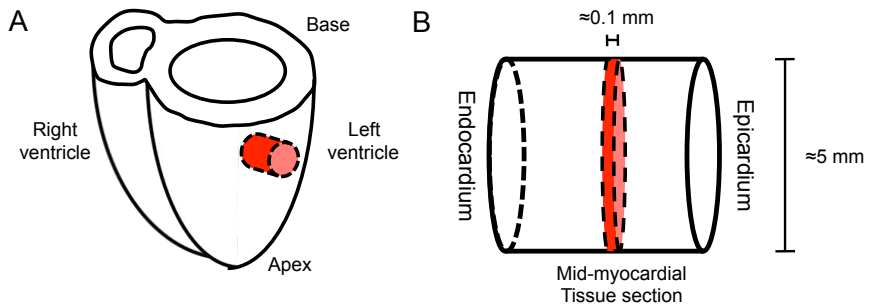


**Fig. 6.1.** (a) Biopsies with a diameter of 5 mm were taken from the left ventricle. (b) After freezing, they were cut in slices of 80 - 100 $\mu$m. Only mid-myocardial sections were taken into account. Fig. from [32].

Tissue from different regions in two infarcted hearts was obtained. Heart 1 was taken out after 8 days of infarction, heart 2 after 19 days. Biopsies in four distances from the infarct were taken in heart 2: Region 1 (directly adjacent to the scar), region 2 (in 2 mm distance to the scar), region 3 (in 3 mm distance to the scar) and region 4 (in 7-8 mm distance to the scar). In heart 1, only biopsies from regions 3 and the scar itself were collected. The scar was located on the epicardium.

## 6.2 Fluorescent Labeling

In this work, a number of different cellular structures are aimed to be displayed. The used laser scanning confocal microscope (Zeiss LSM 5 Duo confocal microscope) is able to excite and detect four different wavelengths. Therefore, several combinations of up to four dyes were used to show all important relations.
The incubations for labeling were conducted on a laboratory platform rocker at room temperature (Thermo Fisher Scientific, Waltham, MA). Between incubation steps, samples were rinsed three to five times with PBS for 15 minutes per rinse. Primary and secondary antibody incubations were 12 and 6 hours, respectively. In the appendix A, all labeling procedures are described in detail. The interstitial space was identified by incubating with WGA-conjugated to Alexa Fluor 488, 555 or 633 (Invitrogen, Carlsbad, California) at a concentration of 40 $\mu$g/ml. After labeling with WGA, tissue samples were permeabilized with 0.5 % Triton-X for 1hour. Nuclei were identified by staining with 4',6-diamidino-2-phenylindole (DAPI) (365 nm) in a 1:500 dilution. To visualize protein distributions, samples were labeled with antibodies for Cx43, Cx45, vimentin, N-Cadherin (NC) and $\alpha$-smooth muscle actin ($\alpha$SMA). Cx43 was identified by labeling with mouse monoclonal GJA1 IgM or IgG1 anti-Cx43 (Abcam, Cambridge, UK) in a 1:100 dilution, followed by goat anti-mouse IgG1 or IgM, respectively, conjugated to Alexa Fluor 488, 555 or 633 (Invitrogen, Carlsbad, CA) in the same dilution. Similarly, Cx45 was identified by labeling with mouse monoclonal GJA7 IgG1 anti-Cx45 (Abcam, Cambridge, UK) in a 1:100 dilution, followed by goat anti-mouse IgG1 conjugated to Alexa Fluor 488, 555 or 633 (Invitrogen, Carlsbad, CA) in the same dilution. Mouse monoclonal IgG1 anti-vimentin (Sigma, St. Louis, MO) conjugated to Cy3 (555 nm) was used in a 1:20 dilution to stain the cytoskeleton of fibroblasts. NC is a glycoprotein that mediates calcium-dependent adhesion of cells [26]. For its staining, a 1:25 dilution of mouse monoclonal anti-N-Cadherin

IgG1 (Abcam, Cambridge, UK) and goat anti-mouse IgG1 conjugated to Alexa Fluor 488, 555 or 633 (Invitrogen, Carlsbad, CA) in a 1:100 dilution was used. $\alpha$SMA is present in smooth muscle cells, especially in myofibroblasts and endothelial cells [120]. We applied mouse monoclonal IgG2a $\alpha$-smooth muscle anti-actin (Sigma, St. Louis, MO) in a 1:200 dilution in combination with goat anti-mouse IgG2a conjugated to Alexa Fluor 488, 555 or 633 (Invitrogen, Carlsbad, CA) in the same dilution. In case of multiple labeling with IgG1 antibodies, the antibody to the protein that is suspected to have the least fluorescence intensity in tissue was applied first (e. g. anti-Cx45 was applied before anti-vimentin). Samples were stored in PBS until imaging.
DAPI has a fixed wavelength for emission of 365 nm. WGA is available in forms with fluorochromes of the emission wavelenghts 488 nm, 555 nm and 633 nm. All other dyes can be combined with a secondary antibody bound to a fluorochrome of the desired wavelength. However, the wavelength of 365 nm was never used but for labeling with DAPI, since lens errors are here more severe.

## 6.3 Confocal Image Acquisition

Imaging of tissue and beads was performed using a Zeiss LSM 5 Duo confocal microscope (Zeiss, Jena, Germany) equipped with a 40x and 63x oil immersion lens as well as a 2.5x, 10x and 20x lens. The available wavelengths of excitation are 365 nm, 488 nm, 555 nm and 633 nm.

### 6.3.1 Acquisition of Raw Tissue Data

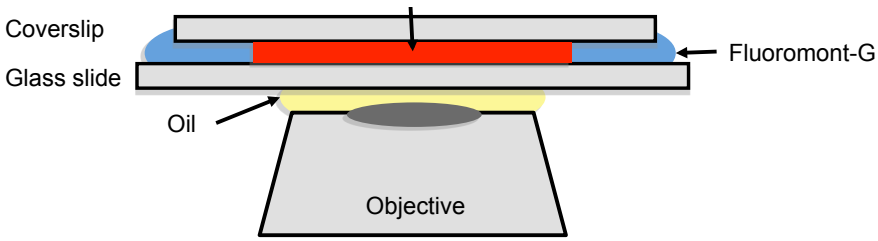


**Fig. 6.2.** Preparation of labeled sections for imaging. The tissue was placed in Fluoromont-G on a glas slide and under a coverslip. Both Fluoromont-G and the oil on the lens preserve the refractory index to prevent loss of intensity by reflection. Fig. adapted from [32].

Fig. 6.2 illustrates the imaging setup. Tissue sections were placed on a glass slide and surrounded by Fluoromont-G (Electron Microscopy Science, Hatfield, USA) to reduce mismatches of the refractive index of glass, tissue and fluid. A coverslip was placed on top. The x-axis of the image stacks was aligned with myocyte orientation via visual inspection and adjustment of the scanning direction. Three-dimensional image stacks were acquired with a typical size of 1024 x 768 x 200 voxels. With the 40x lens, the voxel size was 0.2 $\mu$m x 0.2 $\mu$m x 0.2 $\mu$m in x-, y- and z-direction. When imaging with the 63x lens, the voxel size was 0.1 $\mu$m x 0.1 $\mu$m x 0.1 $\mu$m, respectively. The z-axis was parallel to the laser beam

direction. For all imaging with the Zeiss LSM 5 Duo, a multi-track protocol was applied for quasi-simultaneous slice-wise imaging of two to four labels. The dwell time per voxel was typically 9 $\mu$s.

### 6.3.2 Assessment of Point Spread Functions

3D PSFs were estimated by imaging fluorescent beads with a diameter of 100 nm or 200 nm embedded in agar. The protocol for preparing the beads can be found in the appendix A.
For both the 40x and the 63x oil immersion lens, PSFs for three wavelengths were measured before by Gustavo Lenis. In this work, the PSF of the UV wavelength (365 nm) and the 40x lens was measured. The 3D image stacks typically have sizes of 1024 $\times$ 1026 $\times$ 100 voxels and a voxel size of 0.1 $\mu$m $\times$ 0.1 $\mu$m $\times$ 0.1 $\mu$m in x-, y-, and z-direction. From those stacks, only PSFs with certain criteria were used for analysis: symmetry, ratios of main axes, angles of main axis, maximum value and mean value. Those parameters were adjusted for each wavelength and lens. The final PSF was calculated as the average over at least 15 measured, cropped and rescaled PSFs. For other resolutions than 0.1 $\mu$m $\times$ 0.1 $\mu$m $\times$ 0.1 $\mu$m, resampling to the desired resolution was necessary.

## 6.4 Image Processing

### 6.4.1 General Image Processing

The raw image data was processed using background removal, depth-dependent attenuation correction and deconvolution.
The background was reduced by subtracting the most frequent intensity value of the image (mode) plus one standard deviation in the whole image stack. The attenuation in deeper slices was corrected via an exponential amplification of the signal with the depth in z-direction (section 6.4). This amplification of lower z slices does not improve the signal to noise ratio. Deconvolution was carried out with the Richardson-Lucy algorithm (section 5.3). Fig. 6.3 shows the image data before (a) and after (b) processing. A significant improvement of image quality is visible.

### 6.4.2 Cross-Talk Correction

Antibodies raised in rabbit are very common and frequently applied. However, they cannot be used in rabbit tissue, since unspecific labeling is very high in this case. Different antibodies are often raised in mouse. For the simultaneous imaging of four labels, it is sometimes unavoidable to use antibodies with the same host and the same subtype, for example anti-vimentin and anti-Cx43, that are both raised in mouse and of subtype IgG1. Here, cross-reactions can occur, similar to the case of bleed-through. Fig. 6.4 (top) shows the vimentin channel (left) and an overlay of vimentin and Cx43 channels (right) in an example of bleed-through. It can be clearly seen that the vimentin channel also detects the Cx43 signal, which appears in the overlay as yellow or orange.
The cross-talk from Cx43 to vimentin can be clearly seen in the scatter plot, showing each pixel as a point defined by two intensity values of the two channels (Fig. 6.5a).
In case of cross-talk from only one channel to a second channel and subtracted background signal, the imaging process can be described as:

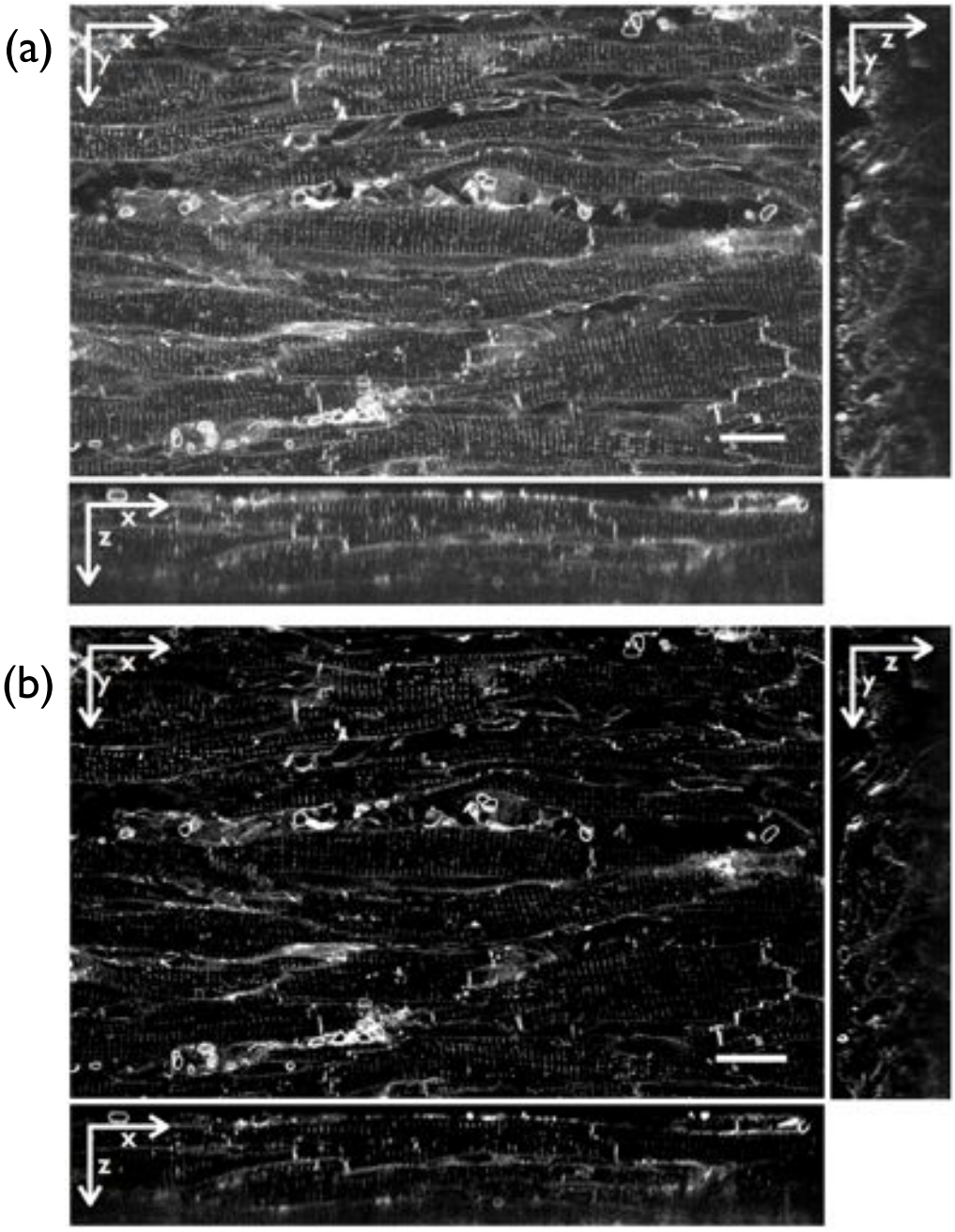


**Fig. 6.3.** (a) Raw image data of WGA. (b) Processed WGA image data. Deeper slices are better visible thanks to attenuation correction. The background has successfully been removed and resolution improved due to deconvolution. Scale bars: 20 $\mu$m.

$$\begin{bmatrix} I_1 \\ I_2 \end{bmatrix} = \begin{bmatrix} w_{11} & 0 \\ w_{21} & w_{22} \end{bmatrix} \begin{bmatrix} C_1 \\ C_2 \end{bmatrix} = \begin{bmatrix} w_{11}C_1 \\ w_{21}C_1 + w_{22}C_2 \end{bmatrix} \tag{6.1}$$

and all other channels are linearly dependent only on the concentration of the referring dye. Cross-talk can be corrected by multiplying the measured intensities with the inverse transformation matrix, leading to the original dye concentrations plus a background signal.

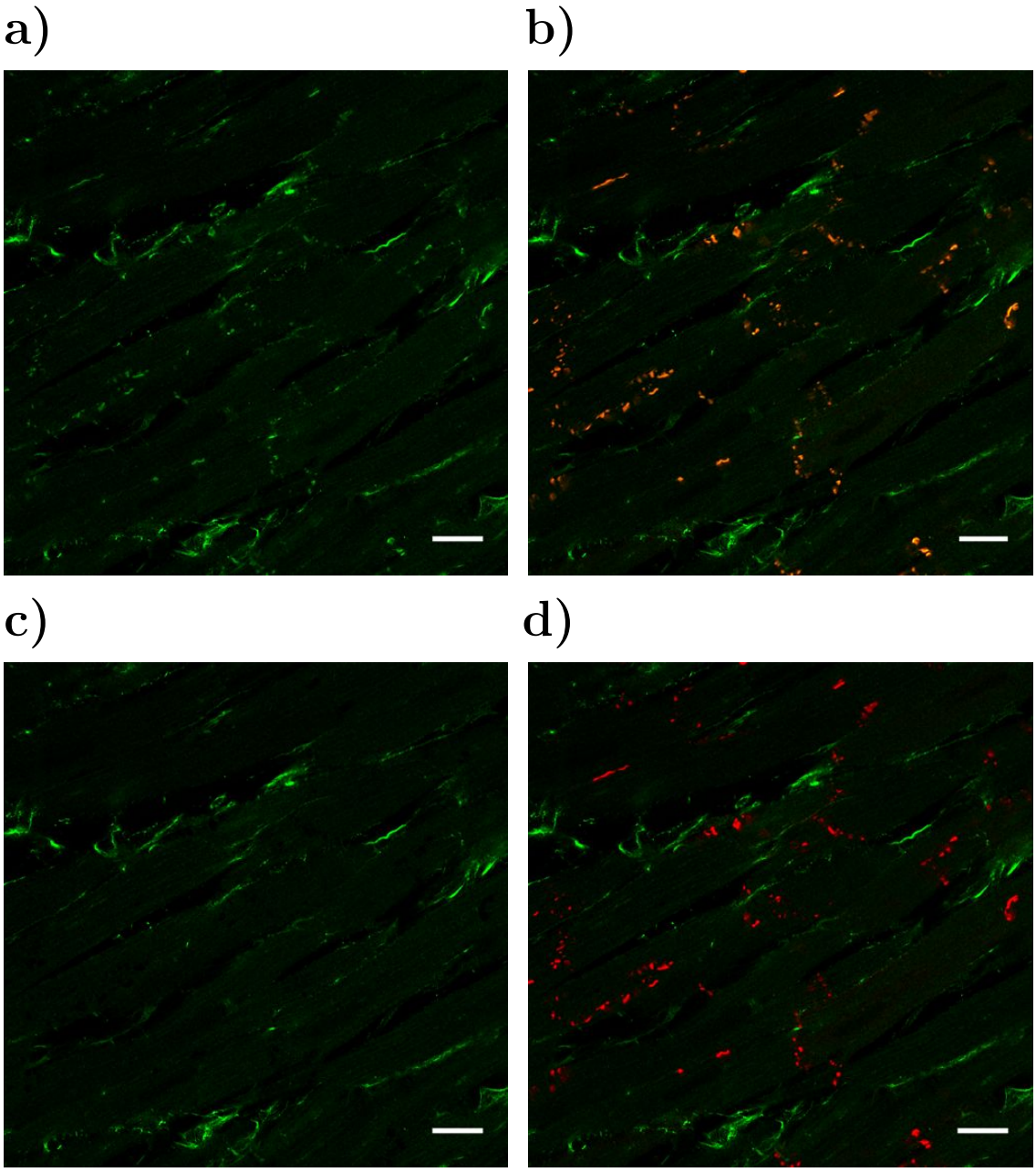


**Fig. 6.4.** (a) Vimentin channel without cross-talk correction, showing both vimentin and Cx43. (b) Overlay of vimentin (green) and Cx43 (red) channels without cross-talk correction. Cross-talk from vimentin to Cx43 appears yellow or orange. (c) Vimentin channel after cross-talk correction. (d) Overlay of vimentin (green) and Cx43 (red) channels after cross-talk correction. No obvious cross-talk can be seen anymore. Scale bars: 20 $\mu$m.

However, diagonal values of the transformation matrix only scale the linear dependency of the measured signal strength of the belonging dye concentration and are therefore not relevant. The correction process merely involves subtraction of the cross-talk in the second channel:

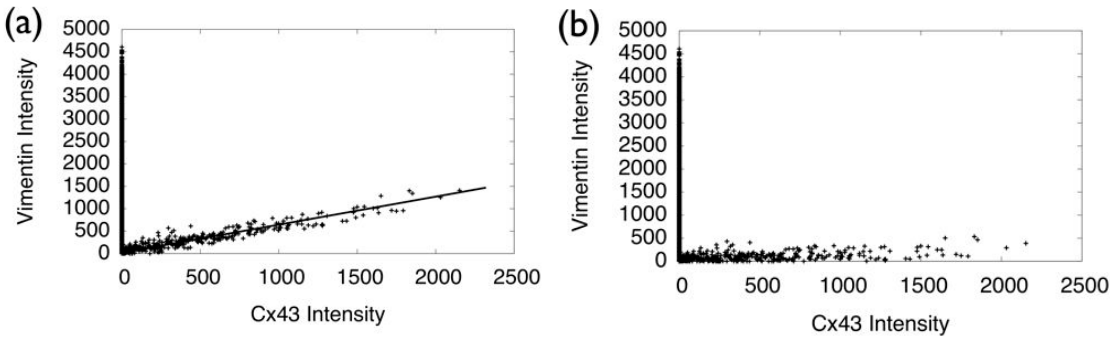


**Fig. 6.5.** (a) Scatter plot of Cx43 and vimentin intensity values before cross-talk correction. (b) Same scatter plot after correction. A clear separation of the channels is visible.

$$\begin{bmatrix} I_{1,corr} \\ I_{2,corr} \end{bmatrix} = \begin{bmatrix} I_1 \\ I_2 \end{bmatrix} - \begin{bmatrix} 0 \\ w_{21}C_1 \end{bmatrix} = \begin{bmatrix} I_1 \\ I_2 \end{bmatrix} - \begin{bmatrix} 0 \\ \frac{w_{21}}{w_{11}}I_1 \end{bmatrix} \tag{6.2}$$

with the corrected intensities $I_{1,corr}$ and $I_{2,corr}$. Estimation of the transformation matrix was thus reduced to the detection of $\frac{w_{21}}{w_{11}}$. In a scatter plot with the intensities of channel 1 and 2, the cross-talk line was visible as skewed scatter, showing a fraction of the intensity in channel 1 proportional to the intensity in channel 2. As the coefficient of this proportional relationship, $\frac{w_{21}}{w_{11}}$ is the slope of the scatter line. In the example in Fig. 6.5, an exemplary scatter plot with bleed-through from the Cx43 associated channel to the vimentin associated channel is shown (a) before and (b) after cross-talk correction. Its slope $\frac{w_{21}}{w_{11}}$ was extracted via a linear fit. In this example, the value for $\frac{w_{21}}{w_{11}}$ was about 0.6. Fig. 6.4 (bottom) shows the results of the cross-talk correction. No significant amount of Cx43 can be seen in the vimentin channel.

### 6.4.3 Estimation of Point Spread Functions

The deconvolution method described in section 5.3 requires PSFs for each lens of each microscope used. This is described in section 6.3.2.
Since the PSF is the image of a point source, it is sought to be measured using a point like object. The PSFs were measured with a resolution of 100 nm in each direction. A precise PSF needs to be caused by an object smaller than one voxel in this resolution, e. g. a spheroid with a diameter of 100 nm or even smaller, if the detected PSF is not completely centered. In this work, beads of 100 nm and 200 nm were used. This is due to the impeded imaging of 100 nm beads in some cases. However, the usage of 200 nm beads may lead to an overestimation of the PSFs.
To assess the influence on the PSF size caused by the finite size of a bead, an error estimation was carried out. First, the resolution of the measured PSF was increased to 25 nm. Afterwards, the PSF is deconvoluted with a sphere having a diameter of 200 nm and scaled to a maximum of one and a minimum of zero. The deconvolution process is described in section 5.3. This deconvoluted PSF was compared to the non-deconvoluted one in the same resolution.

## 6.5 Quantitative Analysis

### 6.5.1 Segmentation of Myocytes, Fibroblasts and Extracellular Matrix

For estimation of volume fractions of myocytes, fibroblasts and extracellular matrix, the pre-processed image stacks of WGA, vimentin and DAPI were segmented using a threshold approach. The threshold was set to the mode of the intensity distribution plus one standard deviation. The thresholded WGA image stack served for reconstruction of the extracellular space. The intracellular space of fibroblasts was segmented by processing and thresholding of the vimentin and DAPI signals. Therefore, a median filter was applied to the pre-processed vimentin images to reduce noise. To eliminate openings in the interior of fibroblasts, the morphological dilation operator (6-neighborhood, 10 iterations) was applied. For distinguishing nuclei from fibroblasts to nuclei of other cells, the colocalization of the dilated vimentin segmented image was calculated by thresholding with the threshold-segmented DAPI signal. The observed distribution is referred to segmented fibroblast-associated DAPI signal. Afterwards, the morphological erosion operator (6-neighborhood, 10 iterations) was applied on the dilated vimentin image. This image was segmented using the threshold described above. Fibroblast distribution was defined as the union of segmented vimentin signal and segmented fibroblast-associated DAPI signal. To calculate the volume fractions, identified voxels were counted and divided by the overall number of voxels. It is assumed that cardiac tissue is composed only of fibroblasts, myocytes and extracellular space. Thus the volume fraction of myocytes $V_{myo}$ was estimated as

$$V_{myo} = 1 - V_{fibro} - V_e \tag{6.3}$$

with $V_{fibro}$ and $V_e$ referring to the volume fractions of fibroblasts and extracellular space, respectively.

### 6.5.2 Estimation of Extracellular Conductivity

Based on the WGA image intensity $I_{WGA}$, conductivity tensors of the extracellular space were estimated. Image stacks of $I_{WGA}$ in normal and infarcted tissue were sampled at a resolution of 800 nm in each direction. As described above, a threshold intensity of WGA $t_{WGA}$ was calculated as the mode plus one standard deviation. Voxel with intensities equal or above $t_{WGA}$ were related to 2 S/m, which is a common value for the conductivity of extracellular fluid [121, 122]. An estimation of this value based on its chemical composition leads to a similar value [123]. Intensity values of the WGA signal less than $t_{WGA}$ were related to a conductivity $\sigma_e$ proportional to $I_{WGA}$:

$$\sigma_e = 2\ S/m \frac{I_{WGA}}{t_{WGA}} \text{ for } I_{WGA} < t_{WGA} \tag{6.4}$$

$$\sigma_e = 2\ S/m \text{ for } I_{WGA} \geq t_{WGA} \tag{6.5}$$

For the measurement, electrodes were modeled by setting two planes on opposite sides of the image stack to a conductivity of 200 S/m. On these electrodes, Dirichlet boundary conditions were defined by setting a constant electrical potential. The other sides of the image stack were impermeable for electric currents, which implies Neumann boundary conditions. The finite element method (FEM) was used to solve Poisson's equation for

stationary electrical fields for the given boundary conditions. The homogenized conductivity of the extracellular space $\sigma_{E,dir}$ for a given direction $dir$ was defined as

$$\sigma_{E,dir} = \frac{J_{dir}}{E_{dir}} \tag{6.6}$$

The scalar $J_{dir}$ refers to the current density through one plane parallel to the electrodes, the scalar $E_{dir}$ to the applied electrical field strength. For each image stack, the scalar conductivity was calculated in the direction along the myocytes (longitudinally) and in two orthogonal directions (transversely), allowing use to define an extracellular conductivity tensor. The described approach to calculate the extracellular conductivity is based on the assumption that no current passes through the cell interior. This assumption is also made in the bidomain model, where intra- and extracellular space are modeled separately.

### 6.5.3 Cx43 Distribution

The analysis of Cx43 distribution on myocyte membranes was performed as described in [32]. In short, myocytes were segmented manually by application of interactive deformation of 3D surface meshes. The thresholded WGA image data was used to refine the segmentation. For each segmented myocyte, volume and image moments were determined. A bounding box around each myocyte, spanned by the calculated eigenvectors, was created and served to determine myocyte length, width and height. The spatial distribution of Cx43 on myocyte membranes was analyzed by projection and summation of Cx43 signal intensities on the myocyte eigenvectors. Profiles were normalized with respect to the total Cx43 intenstiy. Along the first principal component, the polarizations of $Pol_{10\%}$ and $Pol_{25\%}$ were calculated, referring to the fraction of Cx43 on the ends of myocytes. Skewness $\gamma_1$ and kurtosis $\gamma_2$, quantifying asymmetry and peakedness, respectively, were characterized:

$$\gamma_1 = \frac{\mu_3}{\mu_2^{1.5}} \tag{6.7}$$

$$\gamma_2 = \frac{\mu_4}{\mu_2^2} - 3 \tag{6.8}$$

For estimating the degree of coupling between myocytes and fibroblasts as well as in-between fibroblasts, the amount of Cx43 associated with fibroblasts was calculated. A distance map from the segmented vimentin signal was calculated and the Cx43 signal densities in certain intervals of the distance to vimentin were summed. The summed Cx43 signal for different distance ranges was divided by the total amount of Cx43 of the image stack and by the volume of all voxels in this distance to vimentin. The analysis underlies the assumption of a proportional relationship between Cx signal intensity and the amount of gap junctions.

A necessary condition for stable gap junctions is the mechanical cohesion of two cells. NC is responsible for adhesion of cells [26] and thus provides mechanically stable conditions for gap junctions. Previous studies had demonstrated colocalization of Cx43 and NC [124, 125].

To quantify the colocalization of Cx43 with NC, Mander's first coefficient $k_1$ can be calculated [126]:

$$k_1 = \frac{\sum_i (Cx43_i NC_i)}{\sum_i (Cx43_i^2)} \tag{6.9}$$

with the intensity values $Cx43_i$ and $NC_i$ at pixel i.
This overlap coefficient shows how much of the total Cx43 is colocalizing with NC. NC without Cx43 in the same region has no impact on this coefficient.

# 7

# Results

The obtained results of this work are listed and described in this chapter. The quantitative analysis (section 7.3) provides data that can be applied in simulations of cardiac tissue including fibroblasts.

## 7.1 Cell Models

### 7.1.1 Implementation of the Mahajan et al. Model

Based on the CellML version of the Mahajan et al. model [71], it was implemented in the simulation framework of the Institute of Biomedical Engineering, KIT.
The implemented model required a time step of 0.1 $\mu$s for numerical stability. A detailed analysis yielded that this is due to the Markov chain describing the L-Type $Ca^{2+}$ current. For being able to use a time step of 10 $\mu$s, which is computationally affordable, a Runge-Kutta method was applied to the Markov chain.

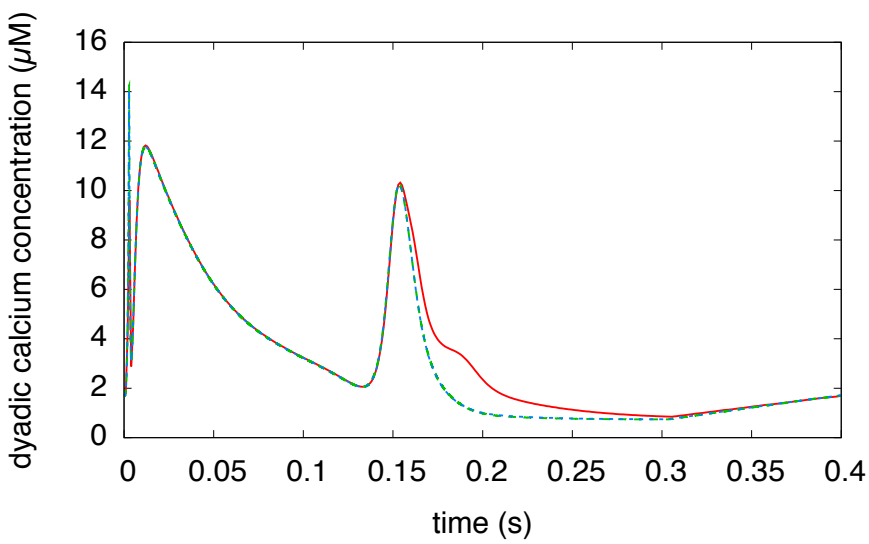


**Fig. 7.1.** The dyadic calcium concentration in dependence of the time at a time step of 10 $\mu$s. Blue-dashed: CellML implementation, red: using Euler method, green-dashed: using Runge-Kutta method. It is clearly visible how the Runge-Kutta method improves accuracy.

Fig. 7.1 shows the dyadic calcium concentration, which is characteristic for the Markov chain, for a time step of 10 $\mu$s. The blue-dashed curve represents the CellML implementation. This curve is seen as the optimal implementation. The red line shows the implementation with the Euler method (root-mean-square difference to CellML implementation: 0.5387 $\mu$M) and the green-dashed line the implementation with the Runge-Kutta method for the Markov chain (root-mean-square difference to CellML implementation: 0.0118 $\mu$M). As Fig. 7.1 shows, the accuracy of the latter implementation is clearly improved.
Although the Runge-Kutta method is computationally more expensive for a certain time step compared to the Euler method, the implementation of the Runge-Kutta method considerably improved the simulation time via resulting in a larger time step for the main part of the computation.

### 7.1.2 Evaluation of the Myocyte Models

The two models of rabbit myocytes, Mahajan et al. and Puglisi et al. (described in section 4.1) show significant differences in the reproduced resting membrane potential (RMP), action potential amplitude (APA), action potential duration (APD), ionic currents $I_I$, effective refractory period (ERP) and conduction velocity (CV). In table 7.1, table 7.2 and table 7.3, they are compared to experimental data from different literature at pacing cycle lengths (PCLs) of 500 ms, 333 ms (350 ms for some parameters) and without knowledge of the PCL. In the two computational models, RMP, APA and ionic currents were simulated in a single cell. ERP und CV are the result of a one-dimensional tissue simulation. The value of CV at a PCL of 333 ms was adjusted to the experimental data by choosing the value of the conductivity in tissue $\kappa$ appropriately.
It is visible that the values in experimental literature vary strongly. There exist significant dependencies on the cell type (i. e. the region in the heart, e. g. endo-/epi-/midmyocardial) [136], temperature [137] and rabbit age [136]. Furthermore, it can be assumed that those values also differ with the technique of data acquisition and experimentalist.
In the scope of uncertainty, both models seem to reproduce cardiac physiology well.
At a PCL of 500 ms, RMP, APA, CV and ionic currents show different deviations to the experimental data, varying with the literature. Mainly [127] matches better with the simulation results of Puglisi et al., while other sources confirm the results of Mahajan et al. in a stronger way. The ERP is better reconstructed in the model of Puglisi et al.
Using a PCL of 333 ms or 350 ms, no significant differences in the two computational models are present in RMP and APA. The APA better fits to the simulation of Mahajan et al., the ERP a trifle better to the one of Puglisi et al.
One ionic current from a source without the knowlegde of the PCL was considered. It matches better with the results of Mahajan et al.
The physiological heart rate of rabbits is about 3 Hz [134], marking table 7.2 the main criterion. In addition to that, values of APD und ERP are more significant for simulations than other parameters.
All in all, it can be abstracted that the model of Mahajan et al. reproduces the rabbit electrophysiology at physiological heart rates slightly more accurate than the one of Puglisi et al. It is appropriate for studying arrhythmias and tachycardia, since it takes the Ca cycling machinery into account. It is therefore suggested to use the latter model for simulation studies.

**Table 7.1.** Comparison of experiment and the ventricular myocyte rabbit models of Mahajan et al. and Puglisi et al. at a PCL of 500 ms. The relative deviations of the computational models relative to the experimental data are given in parentheses.

| | Experiment | Mahajan et al. | Puglisi et al. |
|---|---|---|---|
| RMP (mV) | -79.7 [127] | -87.3 (10 %) | -85.68 (8 %) |
| | -84 [128] | -87.3 (4 %) | -85.68 (2 %) |
| APA (mV) | 127.3 [127] | 123.1 (-3 %) | 125.6 (-1 %) |
| | 116 [128] | 123.1 (6 %) | 125.6 (8 %) |
| $APD_{25}$ (ms) | 169.2 [127] | 104.0 (-39 %) | 155.5 (-8 %) |
| $APD_{30}$ (ms) | 117 [129] | 117.7 (1 %) | 168.6 (44 %) |
| $APD_{50}$ (ms) | 238.2 [127] | 152.2 (-36 %) | 190.8 (-20 %) |
| $APD_{60}$ (ms) | 109 - 135 [130] | 164.5 (22 %) | 197.5 (46 %) |
| $APD_{80}$ (ms) | 165 [129] | 186.2 (13 %) | 208.0 (26 %) |
| $APD_{90}$ (ms) | 323.2 [127] | 196.7 (-39 %) | 212.8 (-34 %) |
| | 195 [131] | 196.7 (1 %) | 212.8 (9 %) |
| | 128 - 156 [130] | 196.7 (26 %) | 212.8 (36 %) |
| | 162 [128] | 196.7 (21 %) | 212.8 (31 %) |
| $APD_{95}$ (ms) | 198.5 [132] | 204.6 (3 %) | 216.0 (9 %) |
| $I_{ks,20mV}$ (pA/pF) | 0.43 - 1.1 [130] | 0.42 (-2 %) | 0.45 (0 %) |
| $I_{kr,20mV}$ (pA/pF) | 0.31 - 0.36 [130] | 0.29 (-6 %) | 1.17 (225 %) |
| $I_{K1,-60mV}$ (pA/pF) | 2.4 [128] | 1.1 (-54 %) | 3.2 (33 %) |
| ERP (ms) | 175 [133] | 208 (19 %) | 171 (-2 %) |
| CV (cm/s) | 76 [133] | 76.4 (1 %) | 74.8 (-2 %) |

**Table 7.2.** Comparison of experiment and the ventricular myocyte rabbit models of Mahajan et al. and Puglisi et al. at a PCL of 333 ms for RMP, APA and APD as well as a PCL of 350 ms for ERP and CV. The relative deviations of the computational models relative to the experimental data are given in parentheses.

| | Experiment | Mahajan et al. | Puglisi et al. |
|---|---|---|---|
| RMP (mV) | -78.7 [134] | -86.9 (10 %) | -84.8 (8 %) |
| APA (mV) | 125.2 [134] | 121.7 (-3 %) | 124.5 (-1 %) |
| $APD_{50}$ (ms) | 138.5 [134] | 133.8 (-3 %) | 162.2 (17 %) |
| $APD_{90}$ (ms) | 169.8 [134] | 179.6 (6 %) | 187.5 (10 %) |
| | 180 [131] | 179.6 (0 %) | 187.5 (4 %) |
| ERP (ms) | 147 [133] | 192 (31 %) | 190 (29 %) |
| CV (cm/s) | 76 [133] | 76.0 (0 %) | 75.9 (0 %) |

**Table 7.3.** Comparison of experiment and the ventricular myocyte rabbit models of Mahajan et al. and Puglisi et al. at a not available PCL. The relative deviations of the computational models relative to the experimental data are given in parentheses.

| | Experiment | Mahajan et al. | Puglisi et al. |
|---|---|---|---|
| $I_{Ca,20mV}$ (pA/pF) | -7.71 [135] | -5.70 (-26 %) | -2.55 (-67 %) |

## 7.2 Confocal Imaging

### 7.2.1 Point Spread Functions

PSFs for the wavelengths of 488 nm, 555 nm and 633 nm have already been measured by Gustavo Lenis. In this work, the PSFs for the UV wavelength of 365 nm had to be collected in order to deconvolute the images of all channels. Measurement of the UV PSF is impeded, since the UV beads used for PSF measurement bleach very soon and the lenses of the microscope have more severe mistakes due to chromatic aberration. For the UV wavelength, the PSFs were not exactly symmetrical in the x-y-plane. This can be explained by lens failure and variance of the PSFs with space.

As described in section 6.4.3, an estimation of the error caused by the finite size of the beads was carried out. A measured PSF (wavelength 633 nm, 63x lens, bead size 200 nm) was sampled at a resolution of 25 nm in each direction and deconvoluted with a sphere of 200 nm diameter. Table 7.4 shows the full width half maxima (FWHMs) of the non-deconvoluted (measured) and deconvoluted (corrected) PSFs in each direction.
Visual inspection and the quantitative comparison of the FWHMs demonstrate only minor changes due to deconvolution in this high resolution of 25 nm. Even though the intensity is strongly dependent on the size of the bead, the form of the PSF does not significantly change with a slightly larger bead.
Since the correction process itself may induce errors, it was chosen not to correct the PSFs that arise from 200 nm beads. Usually, a resolution of 100 or 200 nm of the image stacks was used, which minimized the error due to finite bead size.
Tests for correction with a 400 nm diameter bead and a resolution of 25 nm showed significant changes in the FWHMs of the corrected PSF (data not shown). The suggestion of this study therefore is to use 200 nm beads without any correction up to an image resolution of 25 nm, but to avoid larger beads.

**Table 7.4.** Comparison of the FWHMs in each direction of the measured and corrected PSF. Both PSFs are in a 25 nm resolution in each direction. Relative deviations are not more than 5 %.

| | FWHM in x direction | FWHM in y direction | FWHM in z direction |
|---|---|---|---|
| measured PSF | 359 nm | 405 nm | 1 174 nm |
| corrected PSF | 341 nm | 390 nm | 1 131 nm |
| relative deviation | -5.0 % | -3.7 % | -3.7 % |

### 7.2.2 Processed Tissue Data

The following sections show samples of the final processed tissue image stacks. 2D images from three orthogonal planes are provided for each stack, visualizing each recorded channel in a separate color. This color is not referring to the excitation or absorption wavelength.
The image data involved up to four labels per tissue preparation. A maximum of three different labels per image stack are shown, making additive RGB images possible. The colors used do not refer to excitation or emission wavelengths. For the quantitative analysis, a number of stacks (n) of each kind were taken into account.

#### 7.2.2.1 Normal Myocardium

Fig. 7.2 shows an overlay of DAPI (in blue), vimentin (in green) and WGA signal (in red) in normal myocardial rabbit tissue. Myocytes lie straight aligned, fibroblasts can be found in the space between myocytes. They have an elongated shape.

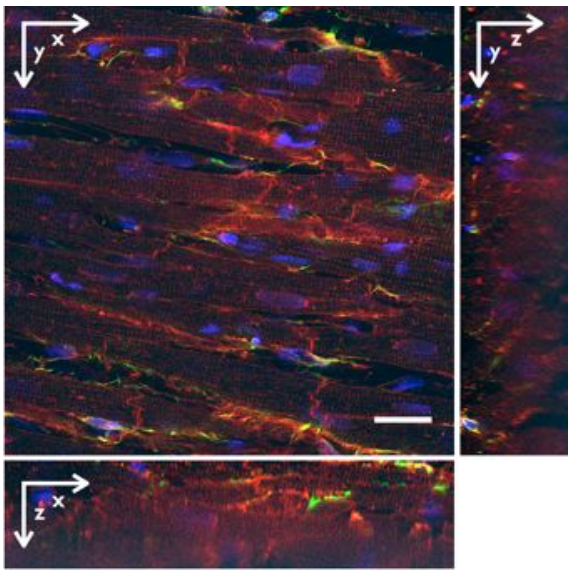


**Fig. 7.2.** Tissue of healthy rabbit myocardium in the left ventricle. The extracellular matrix is labeled via WGA (red), vimentin in green shows fibroblasts and DAPI in blue the nuclei. Scale bar: 20 $\mu$m.

Fig. 7.3 shows the same image stack as 7.2, but including the signals of WGA (in red), Cx43 (in blue) and vimentin (in green). Cx43 can be found in the intercalated discs of myocytes as well as on their lateral sides. Fibroblasts do not seem to express Cx43. Noticeable is the large amount of lateral Cx43 that is not located at intercalated discs. To distinguish this from unspecific labeling, three different antibodies were tested (data not shown), all showing the same lateral labeling. Furthermore, image stacks with WGA, NC and Cx43 signals were collected (Fig. 7.4). A very good colocalization of Cx43 signal with NC signal is visible, indicating both specific labeling and a high probability of gap junction functionality.
Labeling of vimentin, Cx45 and WGA in the normal myocardium (Fig. 7.5a) shows not

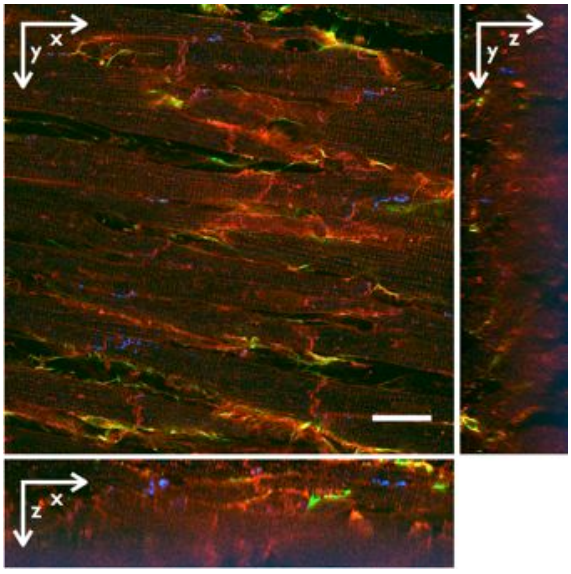


**Fig. 7.3.** Tissue of healthy rabbit myocardium in the left ventricle. The extracellular matrix is labeled via WGA (red), vimentin in green shows fibroblasts and Cx43 in blue the gap junctions of the Cx43 type. Scale bar: 20 $\mu$m.

**a)**

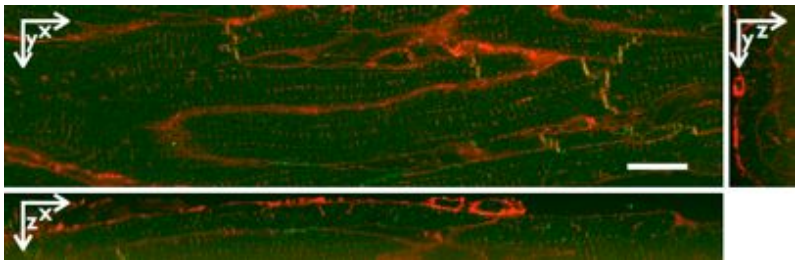


**b)**

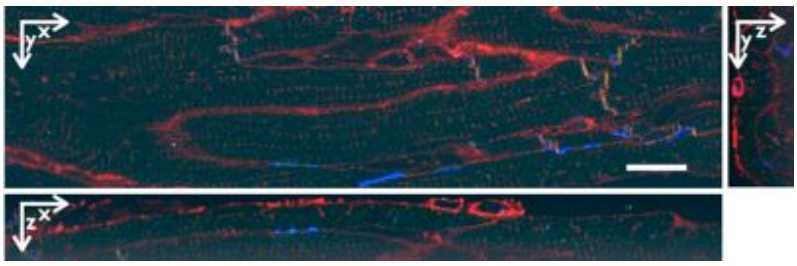


**Fig. 7.4.** (a) Labeling with WGA (red) and anti-NC (green). NC localizes on the membrane of myocytes, especially in the intercalated discs. (b) Same tissue section including WGA in red, NC in green and Cx43 in blue. Cx43 is only found in regions near NC, supporting the hypothesis of specific Cx43 labeling and potentially functional gap junctions. Scale bars: 20 $\mu$m.

a significant amount of Cx45. Few spots are visible but may be explained by unspecific labeling. As a positive control for the Cx45 antibody, atrial tissue near the sinus node was

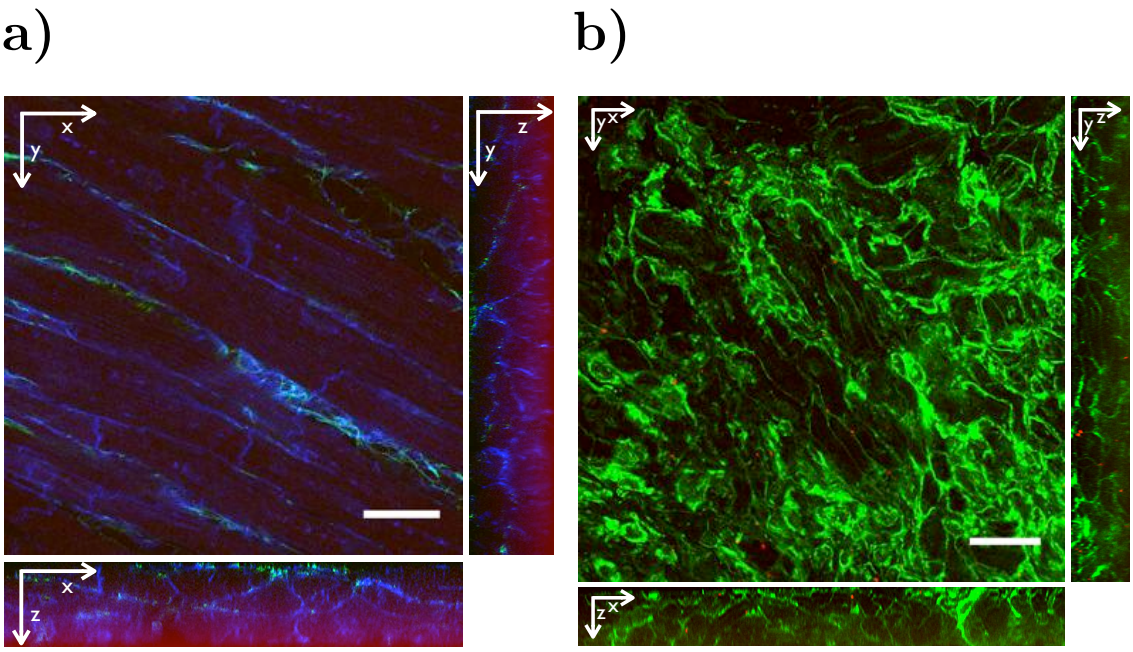


**Fig. 7.5.** (a) Tissue of healthy rabbit myocardium in the left ventricle. The extracellular matrix is labeled via WGA in blue, Cx45 in red via the correspondent antibody, and vimentin in green shows fibroblasts. No significant amount of Cx45 is visible. (b) Atrium near the sinoatrial node labeled with WGA (green) and anti-Cx45 (red) serving as a positive control for the Cx45 labeling. A considerable amount of Cx45 can be seen. Scale bars: 20 $\mu$m.

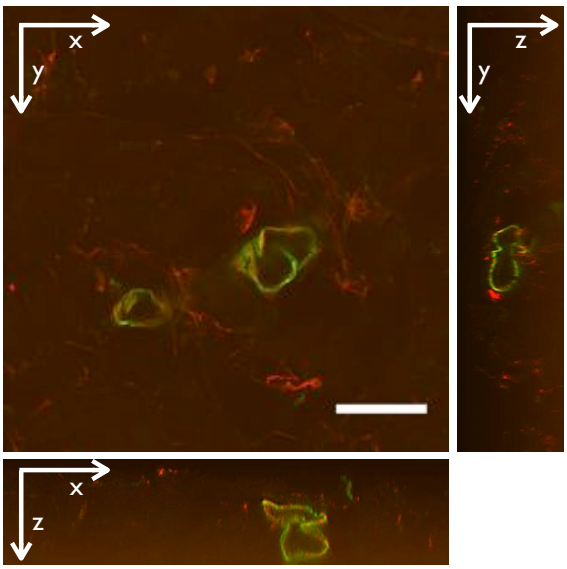


**Fig. 7.6.** Tissue of healthy rabbit myocardium in the left ventricle. Anti-vimentin (red) labels fibroblasts and endothelial cells, smooth muscle cells (myofibroblasts and endothelial cells) are labeled by anti-$\alpha$SMA (green). No considerable amount of myofibroblasts can be found. Vessels are clearly labeled by anti-$\alpha$SMA. Scale bar: 20 $\mu$m.

labeled with anti-Cx45 and WGA (Fig 7.5b). A considerable amount of Cx45 is shown. The Cx45 in working myocardium sits on the membrane of the myocytes, indicating specific

labeling.
For distinguishing fibroblasts and myofibroblasts (both labeled by anti-vimentin), some sections were labeled with anti-vimentin and anti-$\alpha$SMA (Fig. 7.6). However, only blood vessels were visible in the $\alpha$SMA channel. Vessels were identified by the characteristics branching, absent isolation and form. Images that were recorded with the 2.5x lens clearly showed the characteristics of vessels (data not shown).

#### 7.2.2.2 Infarcted Myocardium

Image stacks of different regions in two infarcted hearts were collected. Heart 1 was taken out after 8 days of infarction, heart 2 after 19 days.
In this section, only image stacks from heart 2 are shown. The analysis (section 7.3.1) took both hearts separately into account.
Some of these images show spheres in the WGA channel with a diameter of some $\mu$m. They are referred to red blood cells that were not washed out due to occlusion in vessels.
Fig. 7.7a shows vimentin, Cx43 and WGA signal in region 1 (directly adjacent to the scar). Differences to the healthy myocardium are visible. Myocytes partly lose their ordered, straight aligned structure. The number of fibroblasts and their volume fraction seem to increase. The amount of Cx43 increases and it spreads out even more to the lateral sides of the myocyte membranes.
Some fibroblasts show Cx43 sitting on the membrane. A number of Cx43 spots between myocytes and fibroblasts can be found. Visual inspection therefore suggests a possible coupling of myocytes and fibroblast clusters via Cx43 in infarcted tissue.
Region 2 (about 2 mm distance to the scar) is shown in Fig. 7.7b. It shows similar characteristics as region 1, intense differences to the healthy myocardium are visible.
Fig. 7.7c refers to region 3 in the infarcted heart (about 3 mm distance to the scar). Compared to regions 1 and 2, the distribution of Cx43 seems to go back to some extent to the case of healthy myocardium, the amount of lateral Cx43 decreases. The structure of myocytes changes partly to the aligned structure. Still, some differences to the healthy myocardium can be seen.
Region 4 (about 7-8 mm distance to the scar) shows data almost similar to the healthy tissue (Fig. 7.7d). Most myocytes are straight aligned, Cx43 was found in the intercalated discs and on the lateral sides of myocyte membranes. A slight remodeling however is still present.
Imaging infarcted tissue in heart 1 and 2, including all regions, suggested only few gap junctional coupling of the Cx45 type. Fig. 7.8 shows a small region of a labeling with WGA in blue, anti-vimentin in green (bad quality) and anti-Cx45 in red in region 2. In this image, a cluster of some fibroblasts with Cx45 is visible. The Cx45 sits on the fibroblast membrane, a hint for specific labeling. However, cases like the one shown are rare. In the quantitative analysis, it was thus concentrated on the distribution of Cx43.
In order to estimate the extent of myofibroblasts in infarcted tissue, again labeling with anti-$\alpha$SMA was used.
Both in heart 1 and 2, no significant amount of myofibroblasts could be found. In Fig. 7.9, vimentin is shown in red and $\alpha$SMA in green. Only vessels can be seen in the $\alpha$SMA channel.
In heart 1 (8 days old), image stacks of the scar itself were collected. They mainly showed dead tissue. One stack at the border zone of the scar is shown in Fig. 7.10. No working

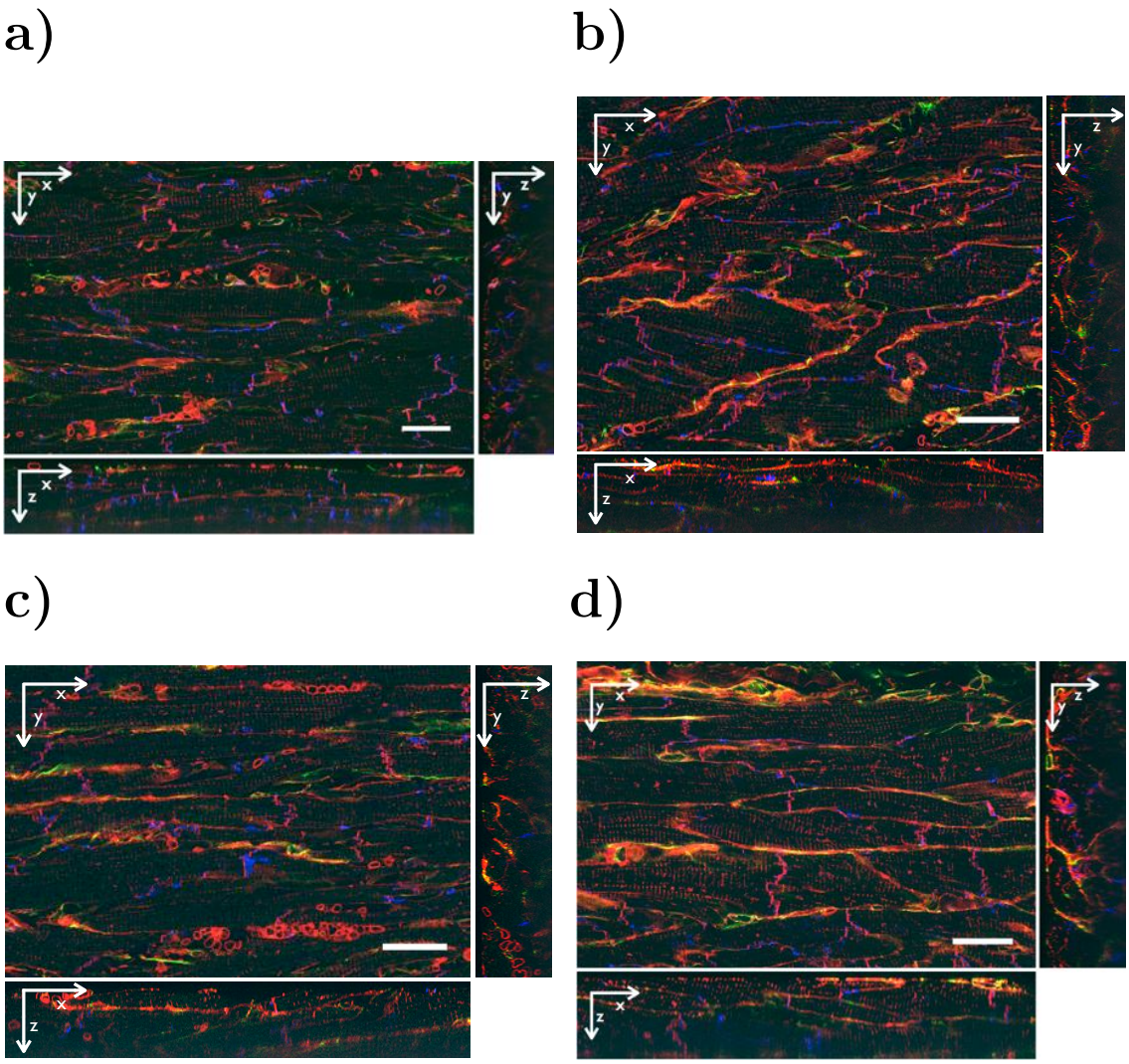


**Fig. 7.7.** (a) Infarcted tissue in region 1 (directly adjacent to the scar). WGA (red) labels the extracellular matrix, vimentin (green) indicates fibroblasts and endothelial cells, Cx43 (blue) is labeled via the correspondent antibody. Clear differences to healthy myocardium are visible, mainly structural remodeling of myocytes, fibroblasts and Cx43. (b) Infarcted tissue in region 2 (about 2 mm distance to the scar). WGA (red) labels the extracellular matrix, vimentin (green) indicates fibroblasts and endothelial cells, Cx43 (blue) is labeled via the correspondent antibody. There are still intense differences to the healthy myocardium visible. (c) Infarcted tissue in region 3 (about 3 mm distance to the scar). WGA (red) labels the extracellular matrix, vimentin (green) indicates fibroblasts and endothelial cells, Cx43 (blue) is labeled via the correspondent antibody. Compared to regions 1 and 2, the distribution of Cx43 seems to go back to some extent to the case of healthy myocardium. The structure of myocytes changes partly to the aligned structure. (d) Infarcted tissue in region 4 (about 7-8 mm distance to the scar). WGA (red) labels the extracellular matrix, vimentin (green) indicates fibroblasts and endothelial cells, Cx43 (blue) is labeled via the correspondent antibody. Strong differences to the healthy myocardium cannot be seen. Scale bars: 20 $\mu$m.

myocardium was available in this case, but a large number of fibroblasts with Cx43 could be found.

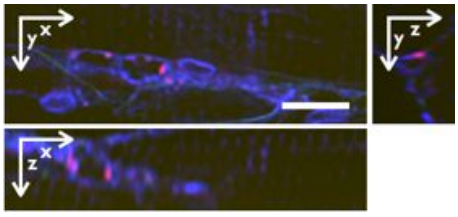


**Fig. 7.8.** Small region in infarcted tissue of region 2 (in 2 mm distance the scar). WGA (blue) labels the extracellular matrix, vimentin (green, bad quality) indicates fibroblasts and endothelial cells, Cx45 (red) is labeled via the correspondent antibody. The WGA signal mainly covers the vimentin signal. While Cx45 normally is sparse, a cluster of fibroblasts with Cx45 can be found here. Scale bar: 20 $\mu$m.

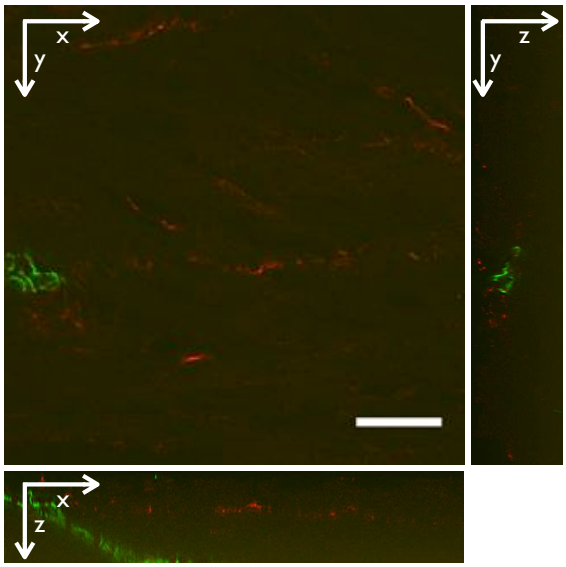


**Fig. 7.9.** Infarcted tissue in region 1 (directly adjacent to the scar region). Vimentin in red indicates fibroblasts and endothelial cells, myofibroblasts and endothelial cells in green are labeled via anti-$\alpha$SMA. $\alpha$SMA signal shows only vessels, no myofibroblasts are visible. Scale bar: 20 $\mu$m.

## 7.3 Quantitative Analysis

### 7.3.1 Volume Fractions of Myocytes, Fibroblasts and Extracellular Space

Table 7.5 summarizes the calculated volume fractions of fibroblasts $V_{fibro}$, extracellular space $V_e$ and myocytes $V_{myo}$, respectively. $V_{fibro}$ was smaller in normal tissue than in regions 1, 2 and 3 in MI. Region 4 had almost the same $V_{fibro}$ as normal tissue. $V_e$ was lower in normal tissue than in tissue from region 1. $V_e$ increased with decreasing distance to the scar in MI tissue. $V_{myo}$ was larger in normal tissue than in region 1. In MI tissue a decreasing $V_{myo}$ was found with decreasing distance to the scar.
In heart 1 (8 days of infarction) and the scar region, only very few image stacks were available. These data did not lead to reliable results. Especially in the scar region, the approximation of presence of only myocytes, fibroblasts and extracellular matrix might be wrong, since other cell types can be increased here. Thus, $V_{myo}$ might be overestimated.

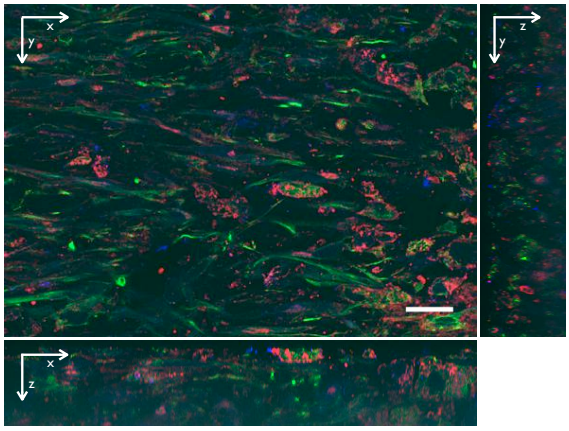


**Fig. 7.10.** Scar border zone tissue in heart 1 (8 days old). WGA (red) labels the extracellular matrix, vimentin (green) indicates fibroblasts and endothelial cells, Cx43 (blue) is labeled via the correspondent antibody. The considerable amount of Cx43 on the large number of fibroblasts might be responsible for the propagation of electrical activation through the scar border zone. Scale bar: 20 $\mu$m.

**Table 7.5.** Estimated volume fractions of fibroblasts, extracellular space and myocytes.

| Tissue | $V_{fibro}$ (%) | $V_e$ (%) | $V_{myo}$(%) |
|---|---|---|---|
| Normal | 4.83 ± 0.42 (n=4) | 18.97 ± 9.47 (n=12) | 76.20 ± 9.89 |
| Region 1 | 5.12 ± 0.55 (n=4) | 24.66 ± 11.11 (n=2) | 70.22 ± 11.66 |
| Region 2 | 6.05 ± 0.46 (n=4) | 17.12 ± 1.74 (n=4) | 76.83 ± 2.20 |
| Region 3 | 6.51 ± 0.38 (n=4) | 14.73 ± 2.37 (n=4) | 78.76 ± 2.75 |
| Region 4 | 4.87 ± 0.76 (n=6) | 14.37 ± 1.20 (n=5) | 80.76 ± 1.96 |
| Heart 1 | 13.40 (n=1) | 31.65 ± 8.02 (n=3) | 54.95 ± 8.02 |
| Scar | 12.6 (n=1) | 14.56 (n=1) | 72.84 |

### 7.3.2 Extracellular Conductivity

The calculated extracellular conductivities are listed in table 7.6. For each image stack, the conductivity was calculated in three directions: longitudinally ($\sigma_{e,long}$, x-direction) and transversally ($\sigma_{e,trans1}$, y-direction, and $\sigma_{e,trans2}$, z-direction). As previously mentioned, the x-direction is aligned with the myocyte orientation, and the z-direction is transmural. Compared to normal tissue, $\sigma_{e,long}$ in infarcted tissue was increased in region 2 and slightly increased in regions 3 and 4. With some exceptions in the second transversal direction, $\sigma_{e,trans1}$ and $\sigma_{e,trans2}$ increased in infarcted tissue. The anisotropy ratio $\frac{\sigma_{e,long}}{\sigma_{e,trans1}}$ was decreased in all regions of infarcted tissue, but mostly in region 2. Taking the second transversal direction into account, the anisotropy ratio $\frac{\sigma_{e,long}}{\sigma_{e,trans2}}$ was slightly different in all regions. Normal and infarcted tissue were similar in this parameter.
Data for heart 1 were sparse and therefore not significant.

### 7.3.3 Cx43 Distribution

In an attempt to support the Cx43 labeling, an additional labeling with anti-NC was performed. NC is responsible for adhesion of cells [26] and thus provides mechanically stable conditions for gap junctions. Previous studies have demonstrated colocalization of

**Table 7.6.** Calculated extracellular conductivity in the longitudinal direction ($\sigma_{e,long}$) and both transversal directions ($\sigma_{e,trans1}$ and $\sigma_{e,trans2}$).

| Tissue | $\sigma_{e,long}$ (S/m) | $\sigma_{e,trans1}$ (S/m) | $\sigma_{e,trans2}$ (S/m) | $\frac{\sigma_{e,long}}{\sigma_{e,trans1}}$ | $\frac{\sigma_{e,long}}{\sigma_{e,trans2}}$ |
|---|---|---|---|---|---|
| Normal (n=4) | 0.264 ± 0.082 | 0.126 ± 0.056 | 0.217 ± 0.073 | 2.095 ± 1.11 | 1.217 ± 0.06 |
| Region 1 (n=2) | 0.264 ± 0.029 | 0.172 ± 0.029 | 0.200 ± 0.031 | 1.535 ± 0.09 | 1.320 ± 0.06 |
| Region 2 (n=4) | 0.400 ± 0.051 | 0.309 ± 0.061 | 0.291 ± 0.116 | 1.295 ± 0.09 | 1.375 ± 0.31 |
| Region 3 (n=4) | 0.284 ± 0.022 | 0.174 ± 0.027 | 0.269 ± 0.111 | 1.632 ± 0.15 | 1.056 ± 0.29 |
| Region 4 (n=4) | 0.284 ± 0.075 | 0.169 ± 0.065 | 0.187 ± 0.065 | 1.681 ± 0.32 | 1.519 ± 0.19 |
| Heart 1 (n=1) | 0.429 | 0.190 | 0.440 | 1.580 | 0.975 |

Cx43 and NC [124, 125]. Mander's coefficient $k_1$ (section 6.5.3) for the overlap of NC signal with Cx43 signal was calculated. A value of $k_1$=0.979 was observed in normal tissue. In infarcted tissue, no labeling with both anti-Cx43 and anti-NC was carried out. Nevertheless, in image stacks with NC in infarcted tissue, plaques of NC on the lateral myocytes membranes were clearly visible (Data not shown. This labeling was done by Eike Wülfers, CVRTI). These findings supported the hypothesis of specific gap junction labeling on lateral membranes even in myocytes from infarcted tissue.

#### 7.3.3.1 Cx43 Distribution on Myocytes

Fig. 7.11 shows the Cx43 distribution on an exemplary myocyte in healthy tissue. The amount of Cx43 is plotted against one of the main myocyte axes. Most significant is the distribution of Cx43 along the x-axis, showing the amount of Cx43 at the ends of the cell and on the lateral sides. Compared to the Cx43 distribution on healthy rat myocytes [32], this plot shows high Cx43 labeling on the lateral sides.
Similarly, an example of the Cx43 distribution on a myocyte in infarcted tissue (region 1) is shown in Fig. 7.12. The distribution of Cx43 along the x-axis is only slightly different to the one in healthy tissue (Fig. 7.11).
In all tissues, myocytes were segmented manually. Some of the myocytes were segmented by Eric Carruth, CVRTI. The statistical analysis [32] was performed with all segmented cells. Table 7.7 and 7.8 list the results of polarizations as well as skewness and kurtosis.

**Table 7.7.** Cx43 distribution on myocytes. Two types of polarization ($Pol_{10\%}$ and $Pol_{25\%}$) along the main axis are calculated. n is the number of segmented myocytes.

| Tissue | $Pol_{10\%}$(%) | $Pol_{25\%}$(%) |
|---|---|---|
| Healthy (n=11) | 12.0±1.9 | 44.1±3.7 |
| Region 1 (n=3) | 12.3±0.4 | 42.6±0.3 |
| Region 2 (n=2) | 9.86±2.0 | 39.8±3.5 |
| Region 3 (n=3) | 12.4±0.6 | 44.8±1.8 |
| Region 4 (n=2) | 10.7±2.3 | 40.7±1.5 |
| Heart 1 (n=3) | 12.9±0.2 | 44.4±3.6 |

The number of segmented cells (n) is very low in all cases. Therefore, no definite statement can be made with these data. However, in these sparse data, the differences between

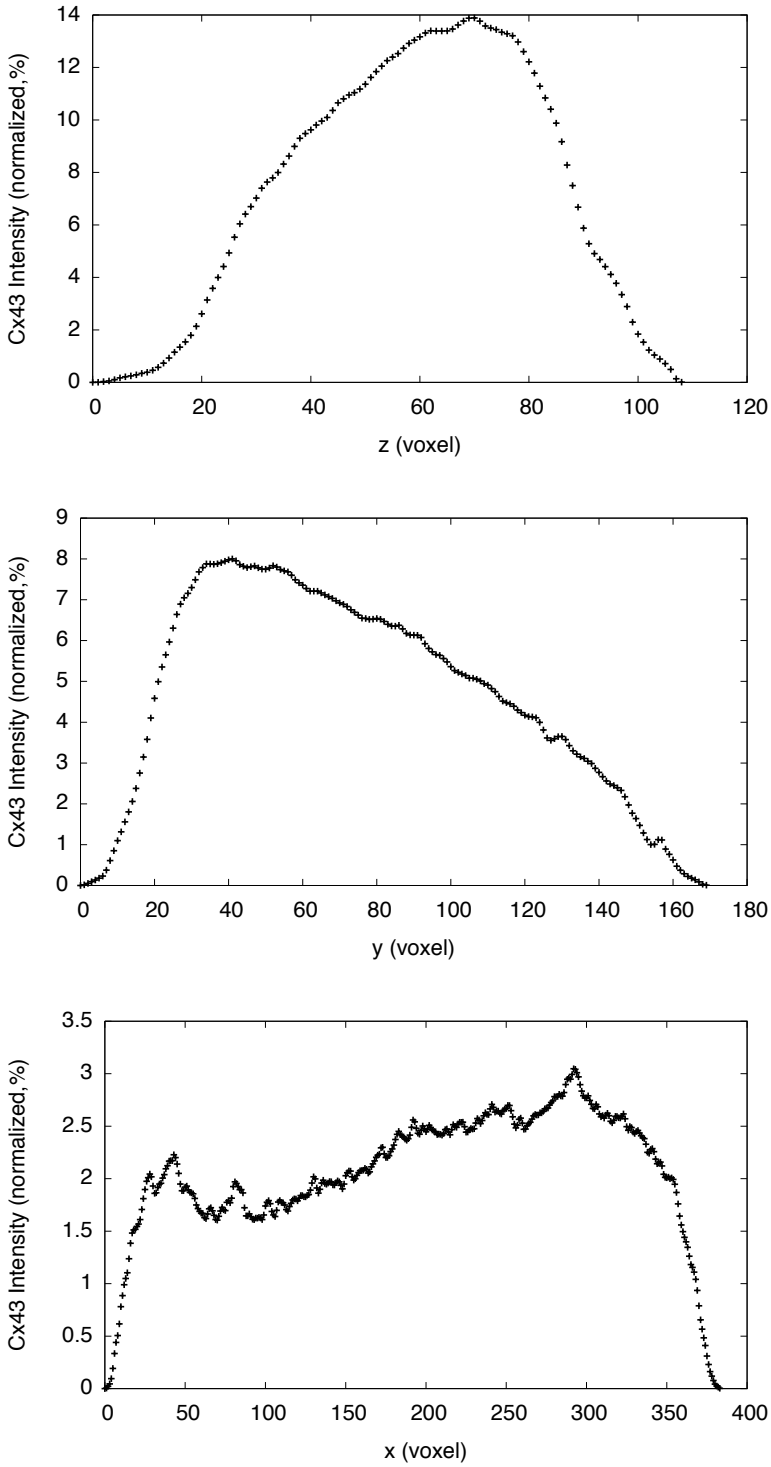


**Fig. 7.11.** Distribution of Cx43 on a myocyte from healthy tissue. The relative amount of Cx43 is plotted along all three axes.

healthy and infarcted tissue do not seem to be very large. Only in regions 2 and 4, a slight

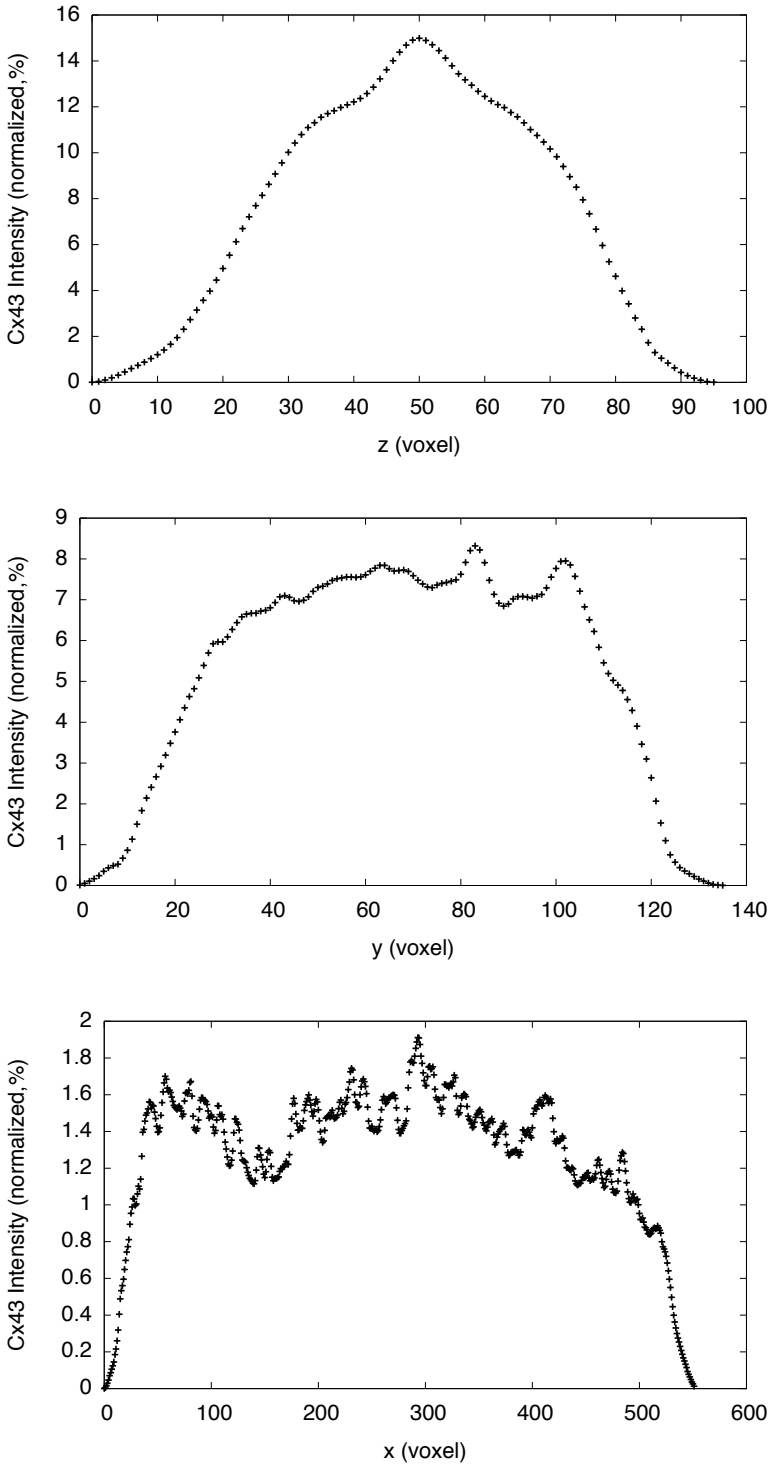


**Fig. 7.12.** Distribution of Cx43 on a myocyte from infarcted tissue (region 1). The relative amount of Cx43 is plotted along all three axes.

decrease of both polarizations was observed. In a comparison with data on healthy rat myocytes [32], a much smaller polarization of the cells in x-direction was found.

**Table 7.8.** Cx43 distribution on myocytes. Skewness and kurtosis in all three directions are listed. n is the same as in table 7.7.

| Tissue | $\gamma_{1,e_1}$ | $\gamma_{2,e_1}$ | $\gamma_{1,e_2}$ | $\gamma_{2,e_2}$ | $\gamma_{1,e_3}$ | $\gamma_{2,e_3}$ |
|---|---|---|---|---|---|---|
| Healthy | -0.093±0.20 | -1.06±0.09 | 0.211±0.18 | -0.803±0.17 | -0.001±0.13 | -0.778±0.09 |
| Region 1 | -0.008±0.10 | -1.080±0.03 | 0.001±0.08 | -0.85±0.23 | -0.035±0.09 | -0.803±0.08 |
| Region 2 | 0.084±0.09 | -1.05±0.03 | 0.135±0.02 | -0.882±0.00 | -0.084±0.01 | -0.798±0.04 |
| Region 3 | -0.042±0.03 | -1.16±0.06 | 0.003±0.10 | -0.786±0.07 | -0.016±0.10 | -0.862±0.02 |
| Region 4 | -0.247±0.01 | -0.946±0.01 | -0.090±0.12 | -0.732±0.04 | -0.028±0.04 | -0.841±0.01 |
| Heart 1 | 0.003±0.13 | -1.11±0.09 | 0.028±0.10 | -0.819±0.06 | 0.018±0.05 | -0.753±0.14 |

#### 7.3.3.2 Cx43 Distribution on Fibroblasts

Fig. 7.13 shows the distribution of Cx43 signal relative to the segmented vimentin signal in normal and MI tissue. On the x-axis, the distance to vimentin is given. The fraction of Cx43 per volume is plotted. The summed intensity of Cx43 in a certain distance to vimentin was divided by the total sum of Cx43 signal intensity in the image stack and by the volume of total voxels in a certain interval of distance to vimentin. In normal tissue (Fig. 7.13a, n=4), the fraction of Cx43 per volume increased with increasing distance to vimentin. However, in all regions of the MI heart (Figs. 7.13b-d, n=4,3,3,2 in regions 1-4), a decrease of Cx43 per volume with increasing distance to vimentin was found. In some histograms, high standard deviations are present at higher distances to vimentin. However, the main information was taken out of the Cx43 distribution close to vimentin, where standard deviations are low.
In table 7.9, the fraction of Cx43 density of a distance up to 0.4 $\mu$m $F_{0.4}$ is summarized. This value is equal to the sum of the first two values in the histograms in Fig. 7.13. In MI tissue, this parameter was found to be about twice larger than in normal tissue. When comparing the regions in infarcted tissue, a smaller $F_{0.4}$ near the scar was observed, but other regions exhibited an almost equal $F_{0.4}$.
Due to a lack of data, this analysis was not performed for heart 1.

**Table 7.9.** Fraction of Cx43 density up to a distance of 0.4 $\mu$m to vimentin $F_{0.4}$ for normal and infarcted tissue.

| Tissue | $F_{0.4}$ ($\frac{\%}{mm^3}$) |
|---|---|
| Normal (n=4) | 8.16 ± 2.61 |
| Region 1(n=4) | 14.22 ± 0.51 |
| Region 2 (n=3) | 17.11 ± 1.98 |
| Region 3 (n=3) | 17.70 ± 1.02 |
| Region 4 (n=2) | 16.55 ± 0.20 |

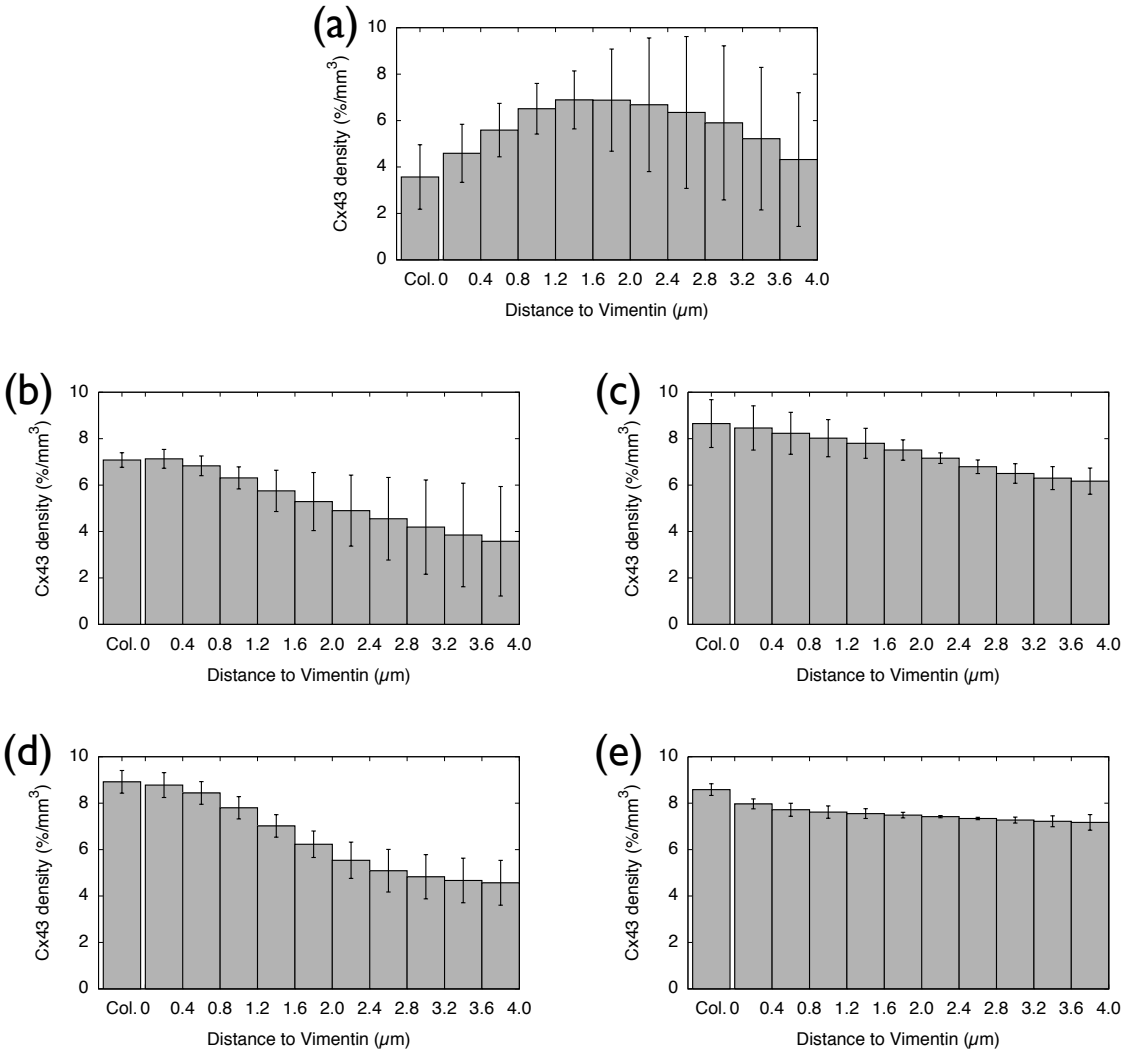


**Fig. 7.13.** Fraction of Cx43 density in certain distances to vimentin in (a) normal and (b-e) region 1-4 of infarcted rabbit tissue. The summed Cx43 intensity in a certain distance to vimentin is divided by the total amount of Cx43 intensity in the image stack and by the volume of all voxels in this distance to vimentin. The first bar in the histogram refers to direct colocalization (Col.) of Cx43 with vimentin. Error bars mark the standard deviation, where each image stack is seen as one event. An increase of Cx43 density with increasing distance to vimentin is visible in normal tissue. In all regions of infarcted tissue, Cx43 intensity decreased with distance to vimentin.

# 8

# Discussion and Limitations

This work gives an overview of fibroblast-myocyte coupling as a target of current research. Appropriate cell and tissue models for quantitative computational study were described. As the main part, confocal microscopy and quantitative analysis were introduced as a tool for estimation of different tissue characteristics. The observed parameters can quantify computational studies of cardiac tissue including fibroblasts.

An approach for quantitative characterization of cardiac tissue was developed, based on scanning confocal microscopy, image reconstruction and analysis. The approach relies on computational methods for processing of high-volume multi-dimensional image data. The approach was applied to tissues from normal and MI hearts to reconstruct tissue micro-structure. Remodeling in MI and normal tissue was analyzed and quantified. The aim was to derive structural parameters that are relevant for computational modeling of electrophysiology of cardiac tissue including fibroblasts.

The developed approaches for estimating volume fractions of myocytes, fibroblasts and the extracellular space as well as the electrical conductivity of the extracellular space are novel. Table 8.1 summarizes the results of different studies concerning the volume fractions of myocytes, fibroblasts and extracellular space. The observed $V_e$ in normal tissue is in agreement with the study in normal rat tissue [17]. However, Bridge et al. [138] found significantly higher values for normal rabbit cardiac tissue. $V_{myo}$ in normal tissue in this study agrees well with the results of Frank and Langer [16] and Lasher et al. [139]. Data on $V_{fibro}$ are sparse in literature. Camelliti et al. [3] estimated the volume fraction of connective tissue to 5 %. This is in good agreement with the findings of this study for $V_{fibro}$. Similar values for $V_{fibro}$ were found after 30 days of infarction in the sheep heart [30]. This is in agreement with the present study of tissue from rabbit hearts after 19 days of infarction. Only a slight increase of this parameter was observed in MI tissue. Furthermore, no significant amounts of Cx45 were found in normal tissue, similar to Teunissen et al. [140] in human, rat and mouse tissue. Camelliti et al. [30] found increased Cx45 in sheep tissue after infarction. Moreover, no myofibroblasts were seen in the MI tissue preparations of this study. Those had been suggested by other studies [141, 56]. However, the development and density of myofibroblasts might change with the region in the MI heart and the age of the MI.

A focus of this study was on electrical anisotropy of cardiac tissue conductivity, which is a major determinant of epicardial potential distribution in simulations [142]. Direct measurements of conductivity are sparse and exhibit high variability [143, 144, 145]. Different modeling approaches have been developed to estimate conductivities [121, 146]. These are

**Table 8.1.** Comparison of estimated volume fractions in normal and infarcted tissue to other studies.

| Parameter | This study (%) | Different Study (%) |
|---|---|---|
| $V_e$ | 18.97 ± 9.47 | 19 ± 0.2 (rat) [17] |
| | | 29 ± 5.2 [138] |
| | | 30.3 ± 5.1 [138] |
| $V_{fibro}$ | 4.83 ± 0.42 | 5.0 (c. t.) [3] |
| $V_{myo}$ | 76.20 ± 9.89 | 75.4 [16] |
| | | 79.7 ± 4.7 [139] |
| $V_{fibro}$ (MI) | 5.12 ± 0.55 (r. 1) | 18.1 ± 0.9 (3d) [30] |
| | 6.05 ± 0.46 (r. 2) | 14.5 ± 0.8 (12d) [30] |
| | 6.51 ± 0.38 (r. 3) | 8.0 ± 0.7 (30d) [30] |
| | 4.87 ± 0.76 (r. 4) | |

c. t.: connective tissue, r.: region, d: days.

based on micro-structural descriptions of tissue.
Table 8.2 summarizes different experimental and computational studies that estimated the conductivity of the extracellular space in normal tissue. The results are in the range of previously reported measurements and the results of modeling studies. In this study, only the anisotropy comparing longitudinal and the first transversal conductivity was taken into account. The extension of the image stacks in z-direction was small and included only a small number of cell layers, which impeded the reliable estimation of the associated conductivity.

**Table 8.2.** Extracellular conductivities in experimental and modeling studies for healthy tissue.

| Reference | $\sigma_{e,long}$ (S/m) | $\sigma_{e,trans}$ (S/m) | $\frac{\sigma_{e,long}}{\sigma_{e,trans}}$ |
|---|---|---|---|
| Clerc* [143] | 0.62 | 0.24 | 2.58 |
| Roberts* [145] | 0.22 | 0.13 | 1.69 |
| Roberts* [147] | 0.12 | 0.08 | 1.50 |
| Stinstra [121] | 0.21 | 0.06 | 3.50 |
| Hand [146] | 0.300 | 0.156 | 1.923 |
| This Study | 0.264 | 0.126 | 2.095 |

*: experimental study.

The approach for quantification of the three-dimensional distribution of gap junctions in relation to fibroblasts is novel. Three-dimensional reconstructions were used to assess the coupling of fibroblasts and myocytes in normal and MI tissue. In normal tissue, no evidence of significant myocyte-fibroblast gap junctional coupling was found. The data suggest significant coupling of myocytes and fibroblasts in MI tissue via Cx43 gap junctions channels.

Elevated Cx43 intensities on fibroblast membranes are interpreted as a sign for coupling between myocytes and fibroblasts and/or in-between fibroblasts. The results do not support hypotheses of high fibroblast-myocyte coupling in normal tissue. However, the possibility that even in normal tissue fibroblasts are to a minor extent coupled by Cx43

cannot be excluded. Cx occurrence in fibroblasts is dependent on the species [47]. In a study with isolated murine ventricular cells [48], fibroblasts were found to express both Cx43 and Cx45. Since Cx45 is sparse in the samples of this study, these data propose a primary fibroblast-myocyte coupling via Cx43.
The parameter $F_{0.4}$ was chosen as a value for the density of Cx43 on the fibroblast membrane and in its neighborhood up to a distance of 0.4 $\mu$m to vimentin. The value of 0.4 $\mu$m was chosen, since this was approximately the resolution of the processed image stacks. However, other parameters might be more representative for the coupling strength of myocytes and fibroblasts, e. g. the slope in the histogramms 7.13 in small distances to vimentin.

It is suggested that the approach provides an improved basis for computational modeling of fibroblast-myocyte interactions in diseased tissue by providing quantitative data on the tissue remodeling. In particular, the developed approach has clinical relevance. Remodeling in MI, especially of gap junctions, is associated with an increased risk of potentially fatal arrhythmia [4]. It has been hypothesized that the increased risk is due to coupling of fibroblasts to myocytes and dependent on the coupling strength [10]. Structural remodeling of myocytes, fibroblasts and extracellular matrix as well as alterations of electrical conductivities during MI might reflect fundamental mechanisms of this disease.

Several limitations must be considered in this study.
Structures with dimensions below the image resolution cannot be resolved. For instance, confocal microscopy cannot distinguish separate gap junctions but only give evidence for the amount of Cx. The small expansion of the image stacks in z-direction affected the estimation of extracellular anisotropy, which is based on the measured geometry of the extracellular space.

Only tissues from two normal and two MI hearts with an MI age of 8 days and 19 days have been analyzed. Data of heart 1 (8 days old) are rare. Infarct geometry might strongly change with each infarcted heart. However, the focus of this study was to introduce methodology. For a statistical analysis, a larger number of preparations has to be considered.
Some of the presented data are sparse and therefore cannot lead to direct conclusions. Those are especially the data on heart 1 (8 days old) and the Cx43 distribution on myocytes.

The focus of this study was on micro-structure only and no functional properties were measured, e.g. gap junction conductances. The existence of Cx on cell membranes merely provides evidence for gap junction coupling. Especially plaques of Cx43 on the lateral sides of myocytes have been found that can be suspected not to mark functional gap junction coupling. However, labeling with NC indicated that the detected Cx is located in a mechanically stable environment, an important requirement for functionality. In culture, a rise of Cx43 on fibroblasts from MI hearts has been shown to be associated with increased functional coupling of those [148]. Moreover, the conductance of gap junctions can change during and after injury [149]. The exclusive detection of Cx in MI

tissue is therefore not a sufficient basis for estimating coupling strengths.

Anti-vimentin labels both the cytoskeleton of fibroblasts, endothelial cells and other very small populations of cells in the heart. In the present study, the amount of fibroblasts therefore might be overestimated. However, a labeling with anti-$\alpha$SMA showed only insignificant amounts of smooth muscle cells.

Limitations were related to antibodies available for identifying proteins in rabbit tissue. A method for correction of cross-talk was applied in the case of multi-labeling in confocal microscopy, caused by bleed-through, cross-talk or cross-reactions of antibodies. Similar approaches will be important when applying multiple labeling under impeded conditions as in rabbit tissue, where the various antibodies raised in rabbit cannot be used.

Intracellular conductivities of myocytes and fibroblasts were not estimated. As stated above, the conductance of gap junctions can change during MI [149], which impedes this estimation in the MI case. In the present approach, it is hard to determine the number of gap junctions between two cells, since only the amount of Cx related signal strength can be measured.

The approach for the estimation of extracellular conductivity is ambiguous. Other scalings of the local conductivities are possible. However, this affects less the calculation of anisotropy ratios and the differences between normal and infarcted tissue. Furthermore, the ionic concentration in the extracellular fluid might change during infarction, which may lead to a conductivity of pure extracellular fluid different to 2 S/m in the case of infarcted tissue.

Only mid-myocardial tissue sections have been analysed. Single samples of epi- or endocardial tissue sections did not show strong visible differences in tissue architecture. However, the distribution of Cx might be different.

This study concentrates on the direct electrical coupling of cells via gap junction channels, which is important for cardiac electrophysiology. Other types of interaction between myocytes and fibroblasts have been proposed [51]. Those have been suggested to be signaling through components of the extracellular matrix or integrins, paracrine signals from fibroblasts impacting myocytes such as cytokines or growth factors as well as paracrine factors like calcium or adenosine-5'-triphosphate.

# 9

# Outlook

Fibrosis, especially after MI, is of important clinical relevance. Investigating possible mechanisms of fibrillation and the interactions of myocytes and fibroblasts are an increasing field in current research.
During the last years, a large number of computational studies investigated the influence of fibroblasts on cardiac electrophysiology. At the same time, different experimental studies aimed to find evidence and to determine the possible occurence and characteristics of the coupling between myocytes and fibroblasts as well as in-between fibroblasts. However, direct proof of this coupling is difficult and there is still a lack of evidence for this coupling in-vivo. Furthermore, the available experimental data is mainly qualitative and does not provide comprehensive quantitative measures for in-silico studies.

One of the main goals for future studies is bringing together experimental data and quantitative computational models. It is important to choose an in-silico model fitting to the observed experimental findings. Here, the rare gap junctional coupling between myocytes and fibroblasts found in healthy tissue suggests modeling fibroblasts as passive electrical barriers. In infarcted tissue, the coupling could be strong enough to apply models such as the multidomain model. Since this model is based on the assumption of static electrical fields, it might be a bad approximation for the case of low coupling strengths.
In an in-silico study, the susceptibility to arrhythmias of myocyte-fibroblast coupling can be investigated. This is mainly relevant for infarcted tissue. Due to the computational effort, it is proposed to start with a simulation of only small parts of the myocardium (in the mm or cm range). Whole heart simulations should be adjourned to later stages. 3D simulations have the advantage of realistical incorporating a scar region and the behavior of electrical excitation waves relative to it. More exact simulations require the direct integration of cardiac microstructure. This might be crucial for the incorporation of fibroblasts, since fibroblasts and their coupling seems to vary strongly within cardiac tissue.
A direct clinical application of the method is thinkable. Biopsies of cardiac tissue from patients could be analyzed, yielding a direct personalized quantification of the patient's cardiac micro-structure. This may give insights into the patient's disease. However, this application would be very time-consuming: Biopsies from different heart regions would need to be analysed. The material for this approach is comparably expensive.
Extension and refinement of the experimental data is needed in order to statistically verify the results of this study. In particular, the vimentin labeling is poor and should be re-

placed for instance by a DDR2 or by a better vimentin labeling. Data of different tissues in a large amount is needed. The MI age should be varied to see differences with the development in time. The immediate results of cell geometry, volume fractions and Cx distribution after a statistically proofed analysis are also of large interest in fundamental medicine and physiology.
The approach for quantitative characterization of cardiac tissue is also relevant for other cardiac modeling studies that do not include fibroblasts. In particular, the estimation of extracellular conductivity is relevant for the majority of all cardiac modeling studies.

# A

# Appendix

## A.1 Protocol: Beads in Agar

1) Measure 2 g of low melting point agar for every 100 ml of distilled water.

2) Mix well and heat up to 50°C until the agar is dissolved (approximately 1 hour).

3) Let the solution slightly cool down to 30°C. It should not solidify.

4) Add the beads to the agar solution in a ratio of 1:625. This is a measure of 3.2 $\mu$l of beads for every 2 ml of agar solution.

5) Mix the beads in the solution on the vortex device for a few seconds. The solution should not solidify.

6) Put a drop of the solution on a glass slide and cover it with a cover slip before solidifying.

7) Put the sample in a case to protect it from light and evaporation. Add a wet tissue slice to keep the humidity high.

8) Store in refrigerator.

## A.2 Protocol: Labeling with WGA, Anti-Cx43, Anti-Vimentin and DAPI

Hearts not perfused with WGA

DAPI – UV
Cx43 – 633 nm (abcam Mouse monoclonal GJA1 IgM (ab11369))
Vimentin – 555 nm (Sigma C9080)
WGA – 488 nm

*Day 1*
**WGA**
Incubate with WGA 488 (Invitrogen) 40 $\mu$g/ml (room temp, on rocker)
Wrap in parafilm and aluminum foil, place on rocker at room temp. for one day.

*Day 2*
Rinse 5 times in PBS, 20 min/rinse (rocker). Remove PBS
**Cx43 and DAPI**
Incubate with Cx43 (abcam Mouse monoclonal GJA1 IgM), room temp., rocker, 1:100 dilution, DAPI 1:500
Parafilm, aluminum foil, room temp., rocker overnight

*Day 3*
Rinse 5 times (15 min), rocker, aluminum foil. Remove PBS.
Incubate with secondary antibody for 6 hours at room temp.
Alexa Fluor 633 goat anti-mouse IgM (1:100 dilution)
Parafilm, aluminum foil, rocker, room temp. for 6 hours
Rinse 3 times in PBS (15 min).

**Vimentin**
Incubate with Vimentin overnight (Sigma C9080, monoclonal Anti-Vimentin-Cy3 antibody produced in mouse)(room temp, rocker). 1:20 dilution
Wrap in parafilm and aluminum foil. Rocker, room temp. overnight.

*Day 4*
Rinse 3 times with PBS (15 min). Rocker, alu foil.
Store in PBS.
Parafilm, aluminum foil, store at 4°C.

## A.3 Protocol: Labeling with WGA, Anti-Cx45, Anti-Vimentin and DAPI

Hearts not perfused with WGA

DAPI – UV
Cx45 – 633 nm (GJA7 Monoclonal Antibody raised in mouse ab78408)
Vimentin – 555 nm (Sigma C9080)
WGA – 488 nm

*Day 1*
**WGA**
Incubate with WGA 488 (Invitrogen) 40 $\mu$g/ml (room temp, on rocker)
Wrap in parafilm and aluminum foil, place on rocker at room temp. for one day

*Day 2*
Rinse 5 times in PBS, 20 min/rinse (rocker). Remove PBS
**Cx45 and DAPI**
Incubate with Cx45 (GJA7 Monoclonal Antibody raised in mouse ab78408), room temp., rocker, 1:100 dilution, DAPI 1:500
Parafilm, aluminum foil, room temp., rocker overnight

*Day 3*
Rinse 5 times (15 min), rocker, aluminum foil. Remove PBS.
Incubate with secondary antibody for 6 hours at room temp.
Alexa Fluor 633 goat anti-mouse IgG1 (1:100 dilution)
Parafilm, alu foil, rocker, room temp. for 6 hours
Rinse 3 times in PBS (15 min).

**Vimentin**
Incubate with Vimentin overnight (Sigma C9080, monoclonal Anti-Vimentin-Cy3 antibody produced in mouse)(room temp, rocker). 1:20 dilution
Wrap in parafilm and aluminum foil. Rocker, room temp. overnight.

*Day 4*
Rinse 3 times with PBS (15 min). Rocker, alu foil.
Store in PBS.
Parafilm, aluminum foil, store at 4°C.

## A.4 Protocol: Labeling with DAPI, WGA, Anti-Cx43 and Anti-NC

Hearts not perfused with WGA

DAPI – UV
Cx43 – 633 nm (abcam Mouse monoclonal GJA1 IgM (ab11369))
N-Cadherin – 555 nm (mouse monoclonal anti-NC IgG1)
WGA – 488 nm

*Day 1*
**WGA**

Incubate with WGA 488 (Invitrogen) 40 $\mu$g/ml (room temp, on rocker)
Wrap in parafilm and aluminum foil, place on rocker at room temp. for one day

*Day 2*
Rinse 5 times in PBS, 20 min/rinse (rocker). Remove PBS
**Cx43 and DAPI**
Incubate with Cx43 (abcam Mouse monoclonal GJA1 IgM (ab11369)),
room temp., rocker, 1:100 dilution, DAPI 1:500
Parafilm, aluminum foil, room temp., rocker overnight

*Day 3*
Rinse 5 times (15 min), rocker, aluminum foil. Remove PBS.
Incubate with secondary antibody for 6 hours at room temp.
Alexa Fluor 633 goat anti-mouse IgM (1:100 dilution)
Parafilm, alu foil, rocker, room temp. for 6 hours
Rinse 3 times in PBS (15 min).

**NC**
Incubate with NC (mouse monoclonal anti-NC IgG1) overnight (room temp, rocker). 1:25 dilution (4 $\mu$g/ml)
Wrap in parafilm and aluminum foil. Rocker, room temp. overnight.

*Day 4*
Rinse 3 times with PBS (15 min). Rocker, alu foil.
Incubate with secondary antibody for 6 hours at room temp.
Alexa Fluor 555 goat anti-mouse IgG1(1:100 dilution)
Store in PBS.
Parafilm, aluminum foil, store at 4°C.

## A.5 Protocol: Labeling with Anti-$\alpha$SMA, Anti-Vimentin, Anti-Cx43 and DAPI

DAPI – UV
Cx43 – 633 nm (abcam Mouse monoclonal GJA1 IgM (ab11369))
Vimentin – 555 nm (Sigma C9080)
$\alpha$SMA – 488 nm (A 5228)

*Day 1*
**Vimentin**
Incubate with Vimentin overnight (Sigma C9080, monoclonal Anti-Vimentin-Cy3 antibody produced in mouse)(room temp, rocker). 1:20 dilution

Wrap in parafilm and aluminum foil. Rocker, room temp. overnight.

*Day 2*
Rinse 5 times in PBS, 20 min/rinse (rocker). Remove PBS
**αSMA**
Incubate with SMA, room temp., rocker, 1:200 dilution. DAPI 1:500
Parafilm, alu foil, room temp., rocker overnight

*Day 3*
Rinse 5 times (15 min), rocker, aluminum foil. Remove PBS.
Incubate with secondary antibody for 6 hours at room temp.
Anti-mouse 488 nm IgG2a secondary (1:200 dilution)
Parafilm, alu foil, rocker, room temp. for 6 hours
Rinse 3 times in PBS (15 min).

**Cx43**
Incubate with Cx43 (abcam Mouse monoclonal GJA1 IgM (ab11369)),
room temp., rocker, 1:100 dilution, DAPI 1:500
Parafilm, aluminum foil, room temp., rocker overnight

*Day 4*
Rinse 5 times (15 min), rocker, aluminum foil. Remove PBS.
Incubate with secondary antibody for 6 hours at room temp.
Alexa Fluor 633 goat anti-mouse IgM (1:100 dilution)
Parafilm, aluminum foil, rocker, room temp. for 6 hours
Rinse 3 times with PBS (15 min). Rocker, aluminum foil.
Store in PBS.
Parafilm, aluminum foil, store at 4°C.

# References


1. A. Hodgkin and A. Huxley, "A quantitative description of membrane current and its application to conduction and excitation in nerve," *Journal of Physioloy*, vol. 177, pp. 500–544, 1952.
2. I. Banerjee, J. W. Fuseler, R. L. Price, T. K. Borg, and T. A. Baudino, "Determination of cell types and numbers during development in the neonatal and adult rat and mouse," *American Journal of Physiology - Heart and Circulatory Physiology*, vol. 293, p. 1883, 2007.
3. P. Camelliti, T. Borg, and P. Kohl, "Structural and functional characterization of cardiac fibroblasts," *Cardiovascular Research*, vol. 65, pp. 40–51, 2005.
4. S. de Jong, T. A. B. van Veen, H. V. M. van Rijen, and J. M. T. de Bakker, "Fibrosis and cardiac arrhythmias," *Journal of Cardiovascular Pharmacology*, vol. 57, pp. 630–638, 2011.
5. M. B. Rook, A. C. G. v. Ginneken, B. d. Jonge, A. E. Aoumari, D. Gros, and H. J. Jongsma, "Differences in gap junction channels between cardiac myocytes, fibroblasts, and heterologous pairs," *American Journal of Physiology*, vol. 263, p. 959, 1992.
6. P. Camelliti, C. R. Green, I. LeGrice, and P. Kohl, "Fibroblast network in rabbit sinoatrial node: Structural and functional identification of homogeneous and heterogeneous cell coupling," *Circulation Research*, vol. 94, pp. 828–835, 2004.
7. F. B. Sachse, A. P. Moreno, and J. A. Abildskov, "Electrophysiological modeling of fibroblasts and their interaction with myocytes," *Annals of Biomedical Engineering*, vol. 36, pp. 41–56, 2008.
8. F. Sachse, A. Moreno, G. Seemann, and J. Abildskov, "A model of electrical conduction in cardiac tissue including fibroblasts," *Annals of Biomedical Engineering*, vol. 37, pp. 874–889, 2009.
9. V. Jacquemet and C. S. Henriquez, "Modulation of conduction velocity by nonmyocytes in the low coupling regime," *IEEE Transactions on Biomedical Engineering*, vol. 56, pp. 893–896, 2009.
10. Y. Xie, A. Garfinkel, J. N. Weiss, and Z. Qu, "Cardiac alternans induced by fibroblast-myocyte coupling: mechanistic insights from computational models," *American Journal of Physiology. Heart and Circulatory Physiology*, vol. 297, pp. H775–84, 2009.
11. M. M. Maleckar, J. L. Greenstein, W. R. Giles, and N. A. Trayanova, "Electrotonic coupling between human atrial myocytes and fibroblasts alters myocyte excitability and repolarization," *Biophysical Journal*, vol. 97, pp. H2931–H2939, 2009.
12. A. Tveito, G. Lines, R. Artebrant, O. Skavhaug, and M. M. Maleckar, "Existence of excitation waves for a collection of cardiomyocytes electrically coupled to fibroblasts," *Mathematical Biosciences*, vol. 1230, pp. 79–86, 2011.
13. K. S. McDowell, J. H. Arevalo, M. M. Maleckar, and N. A. Trayanova, "Susceptibility to arrhythmia in the infarcted heart depends on myofibroblast density," *Biophysical Journal*, vol. 101, pp. 1307–1315, 2011.
14. B. C. Schwab, G. Seemann, R. A. Lasher, N. S. Torres, E. M. Wülfers, M. Arp, E. D. Carruth, J. H. B. Bridge, and F. B. Sachse, "Quantitative Analysis of Cardiac Tissue Including Fibroblasts Using Three-Dimensional Confocal Microscopy and Image Reconstruction: Towards a Basis for Electrophysiological Modeling," *IEEE Transactions on Medical Imaging*, 2012. Submitted.
15. G. Seemann, H. Ying, D. L. Weiss, F. B. Sachse, and O. Dössel, "Effects of Electrophysiological Remodeling in Human Right Atrium: A Simulation Study," in *Proc. Computers in Cardiology*, vol. 32, pp. 69–72, 2005.
16. J. S. Frank and G. A. Langer, "The myocardial interstitium: its structure and its role in ionic exchange," *Journal of Cell Biology*, vol. 60, pp. 586–601, 1974.

17. P. I. Polimeni, "Extracellular space and ionic distribution in rat ventricle," *American Journal of Physiology*, vol. 227, pp. 676–683, 1974.
18. P. Ahuja, P. Sdek, and W. R. MacLellan, "Cardiac myocyte cell cycle control in development, disease, and regeneration," *Physiological Reviews*, vol. 87, pp. 521–544, 2007.
19. J. A. Hill and E. N. Olson, "Cardiac plasticity," *New England Journal of Medicine*, vol. 358, pp. 1370–1380, 2008.
20. J. Dudel, *Physiologie des Menschen*, ch. Grundlagen der Zellphysiologie, pp. 3–19. Berlin, Heidelberg, New York: Springer, 2000.
21. S. Silbernagl and A. Despopoulos, *Taschenatlas der Physiologie*, ch. Grundlagen, Zellphysiologie, pp. 6–19. Thieme, 2003.
22. E. Marbán, T. Yamagishi, and G. Tomaselli, "Structure and function of voltage-gated sodium channels," *Journal of Physiology*, vol. 508, pp. 647–657, 1998.
23. M. Wilhelms and Institute of Biomedical Engineering, *Analysis of cardiac ischemia regarding ECG and stability in a computer model of the human ventricles*. PhD thesis, Karlsruhe, 2009.
24. R. F. Schmidt, *Physiologie kompakt*, ch. Informationsvermittlung durch elektrische Erregung, pp. 11–18. Berlin, Heidelberg, New York: Springer, 1999.
25. G. Seemann, *Modeling of electrophysiology and tension development in the human heart*. PhD thesis, Universitätsverlag Karlsruhe, 2005.
26. U. Tepass, K. Truong, D. Godt, M. Ikura, and M. Peifer, "Cadherins in embryonic and neural morphogenesis," *Nature Reviews*, vol. 1, pp. 91–102, 2000.
27. H. J. Jongsma and M. B. Rook, *Cardiac Electrophysiology. From Cell to Bedside*, ch. Biophysics of cardiac gap junction channels, pp. 119–125. Philadelphia: W. B. Saunders Company, 1999.
28. M. Yeager, *Cardiac Electrophysiology. From Cell to Bedside*, ch. Molecular biology and Structure of cardiac gap junction intercellular channels, pp. 31–40. Philadelphia: W. B. Saunders Company, 1999.
29. T. A. B. van Veen, H. V. M. van Rijen, and T. Opthof, "Cardiac gap junction channels: modulation of expression and channel properties," *Cardiovascular Research*, vol. 51, pp. 217–229, 2001.
30. P. Camelliti, G. P. Devlin, K. G. Matthews, P. Kohl, and C. R. Green, "Spatially and temporally distinct expression of connexins after sheep ventricular infarction," *Cardiovascular Research*, vol. 62, pp. 415–425, 2004.
31. J. E. Saffitz, D. L. Lerner, and K. A. Yamada, *Cardiac Electrophysiology. From Cell to Bedside*, ch. Gap junction distribution and regulation in the heart, pp. 181–191. Philadelphia: W. B. Saunders Company, 2004.
32. D. P. Lackey, E. D. Carruth, R. A. Lasher, J. Boenisch, F. B. Sachse, and R. B. Hitchcock, "Three-dimensional modeling and quantitative analysis of gap junction distributions in cardiac tissue," *Annals of Biomedical Engineering*, vol. 39, pp. 2683–2694, 2011.
33. W. Bargmann, *Das Herz des Menschen*, ch. Bau des Herzens, pp. 88–164. Stuttgart: Georg Thieme Verlag, 1963.
34. R. G. Gourdie, C. R. Green, N. J. Severs, and R. P. Thompson, "Immunolabelling patterns of gap junction connexins in the developing and mature rat heart.," *Anatomy and Embryology*, vol. 185, pp. 363–378, 1992.
35. N. S. Peters, N. J. Severs, S. M. Rothery, C. Lincoln, M. H. Yacoub, and C. R. Green, "Spatiotemporal relation between gap junctions and fascia adherens junctions during postnatal development of human ventricular myocardium," *Circulation*, vol. 90, pp. 713–725, 1994.
36. M. S. Spach, J. F. Heidlage, R. C. Barr, and P. C. Dolber, "Cell size and communication: Role in structural and electrical development and remodeling of the heart," *Heart Rhythm*, vol. 1, pp. 500–515, 2004.
37. J. E. Saffitz and K. A. Yamada, *Cardiac Electrophysiology. From Cell to Bedside*, ch. Gap Junction Distribution in the Heart, pp. 271–277. Philadelphia: W. B. Saunders Company, 1999.
38. N. J. Severs, A. F. Bruce, E. Dupont, and S. Rothery, "Remodelling of gap junctions and connexin expression in diseased myocardium," *Cardiovascular Research*, vol. 80, pp. 9–19, 2008.
39. F. G. Akar, R. D. Nass, S. Hahn, E. Cingolani, M. Shah, G. G. Hesketh, D. DiSilvestre, R. S. Tunin, D. A. Kass, and G. F. Tomaselli, "Dynamic changes in conduction velocity and gap junction properties during development of pacing-induced heart failure," *American Journal of Physiology - Heart and Circulatory Physiology*, vol. 293, pp. H1223–H1230, 2007.
40. G. Seemann, F. B. Sachse, D. L. Weiß, and O. Dössel, "Quantitative reconstruction of cardiac electromechanics in human myocardium: Regional heterogeneity," *Journal of Cardiovascular Electrophysiology*, vol. 14, pp. S219–S228, 2003.
41. E. C. Goldsmith, A. Hoffman, M. O. Morales, J. D. Potts, R. L. Price, A. McFadden, M. Rice, and T. K. Borg, "Organization of fibroblasts in the heart," *Developmental Dynamics*, vol. 230, pp. 787–794, 2004.

42. M. Eghbali, M. J. Czaja, M. Zeydel, F. R. Weiner, M. A. Zern, S. Seifter, and O. O. Blumenfeld, "Collagen chain mRNAs in isolated heart cells from young and adult rats," *Journal of Molecular and Cellular Cardiology*, vol. 20, pp. 267–276, 1988.
43. F. B. Sachse, A. P. Moreno, and J. A. Abildskov, "Electrophysiological modeling of fibroblasts and their interaction with myocytes," in *Proc. International Gap Junctions Conference*, 2007.
44. L. Chilton, W. R. Giles, and G. L. Smith, "Evidence of intercellular coupling between co-cultured adult rabbit ventricular myocytes and myofibroblasts," *The Journal of Physiology*, vol. 583, pp. 225–236, 2007.
45. S. K. Masur, H. S. Dewal, T. T. Dinh, I. Erenburg, and S. Petridou, "Myofibroblasts differentiate from fibroblasts when plated at low density," *Proceedings of the National Academy of Sciences*, vol. 93, pp. 4219–4223, 1996.
46. R. Wolk, S. M. Cobbe, M. N. Hicks, and K. A. Kane, "Functional, structural, and dynamic basis of elctrical heterogeneity in health and diseased cardiac muscle: implications for arrhythmogenesis and anti-arrhythmic drug therapy," *Pharmacology & Therapeutics*, vol. 84, pp. 207–231, 1999.
47. T. A. Baudino, W. Carver, W. Giles, and T. K. Borg, "Cardiac fibroblasts: friend or foe?," *American Journal of Physiology - Heart and Circulatory Physiology*, vol. 291, p. 1015, 2006.
48. Y. Zhang, E. M. Kanter, J. G. Laing, C. Aprhys, D. C. Johns, E. Kardami, and K. A. Yamada, "Connexin43 expression levels influence intercellular coupling and cell proliferation of native murine cardiac fibroblasts," *Cell Communication and Adhesion*, vol. 15, pp. 289–303, 2008.
49. C. Vasquez, N. Benamer, and G. Morley, "The cardiac fibroblast: Functional and electrophysiological considerations in healthy and diseased hearts," *Journal of Cardiovascular Pharmacology*, vol. 57, pp. 380–388, 2011.
50. E. L. Ongstad and R. G. Gourdie, "Myocyte-fibroblast electrical coupling: The basis of a stable relationship," *Cardiovascular Research*, vol. 93, pp. 215–217, 2012.
51. H. S. Duffy, "Fibroblasts, myofibroblasts, and fibrosis: Fact, fiction, and the future," *Journal of Cardiovascular Pharmacology*, vol. 57, pp. 373–375, 2011.
52. A. Hyde, B. Blondel, A. Matter, J. P. Cheneval, B. Filloux, and L. Girardier, "Homo- and heterocellular junctions in cell cultures: An electrophysiological and morphological study," *Progress in Brain Research*, vol. 31, pp. 283–311, 1969.
53. K. Goshima, "Synchronized beating of and electrotonic transmission between myocardial cells mediated by heterotypic strain cells in a monolayer culture," *Experimental Cell Research*, vol. 58, pp. 420–426, 1969.
54. M. Miragoli, G. Gaudesius, and S. Rohr, "Electronic modulation of cardiac impulse conduction by myofibroblasts," *Circulation Research*, vol. 98, pp. 801–810, 2006.
55. M. Miragoli, N. Salvarani, and S. Rohr, "Myofibroblasts induce ectopic activity in cardiac tissue.," *Circulation Research*, vol. 101, pp. 755–758, 2007.
56. J. R. Baum, B. Long, C. Cabo, and H. S. Duffy, "Myofibroblasts cause heterogeneous Cx43 reduction and are unlikely to be coupled to mycytes in the healing canine infarct.," *American Journal of Physiology - Heart and Circulatory Physiology*, 2011.
57. P. Kohl and P. Camelliti, "Fibroblast-myocyte connections in the heart," *Heart Rhythm*, 2011.
58. Statistisches Bundesamt, "Todesursachen in Deutschland 2008," tech. rep., Statistisches Bundesamt, Wiesbaden, 2010.
59. E. Boersma, N. Mercado, D. Poldermans, M. Gardien, J. Vos, and M. L. Simoons, "Acute myocardial infarction," *The Lancet*, vol. 361, pp. 847–858, 2003.
60. S. Rohr, "Myofibroblasts in diseased hearts: New players in cardiac arrhythmias?," *Heart Rhythm*, vol. 6, pp. 848–856, 2009.
61. N. N., "Myocardial infarction redefined–a consensus document of The Joint European Society of Cardiology/American College of Cardiology Committee for the redefinition of myocardial infarction," *European Heart Journal*, vol. 21, pp. 1502–1513, 2000.
62. Kardiol, "www.kardiol.com," 2011.
63. K. Thygesen, J. S. Alpert, and H. D. White, "Universal Definition of Myocardial Infarction," *Circulation*, vol. 116, pp. 2634–2653, 2007.
64. A. E. Epstein, *Cardiac Electrophysiology. From Cell to Bedside*, ch. Ventricular Fibrillation, pp. 705–710. Philadelphia: W. B. Saunders Company, 2004.
65. F. X. Witkowski, L. J. Leon, P. A. Penkoske, W. R. Giles, M. L. Spano, W. L. Ditto, and A. T. Winfree, "Spatiotemporal evolution of ventricular fibrillation," *Nature*, vol. 392, pp. 78–82, 1998.
66. J. N. Weiss, A. Garfinkel, H. S. Karagueuzian, Z. Qu, and P. Chen, "Chaos and the Transition to Ventricular Fibrillation : A New Approach to Antiarrhythmic Drug Evaluation," *Circulation*, vol. 99, pp. 2819–2826, 1999.

67. A. Garfinkel, Y. H. Kim, O. Voroshilovsky, Z. Qu, J. R. Kil, M. H. Lee, H. S. Karagueuzian, J. N. Weiss, and P. S. Chen, "Preventing ventricular fibrillation by flattening cardiac restitution," *Proceedings of the National Academy of Sciences of the United States of America*, vol. 97, pp. 6061–6066, 2000.
68. S. Niederer, M. Fink, D. Noble, and N. Smith, "A meta-analysis of cardiac electrophysiology computational models," *Experimental Physiology*, vol. 94, pp. 486–495, 2009.
69. J. L. Puglisi and D. M. Bers, "LabHEART: An interactive computer model of rabbit ventricular myocyte ion channels and Ca transport," *American Journal of Physiology*, vol. 281, p. 2049, 2001.
70. A. Mahajan, Y. Shiferaw, D. Sato, A. Baher, R. Olcese, L. Xie, M. Yang, P. Chen, J. Restrepo, A. Karma, A. Garfinkel, Z. Qu, and J. Weiss, "A rabbit ventricular action potential model replicating cardiac dynamics at rapid heart rates," in *Biophysical Journal*, vol. 94, pp. 392–410, 2008.
71. CellML, "www.CellML.org," Apr. 2011.
72. C. Luo and Y. Rudy, "A model of the ventricular cardiac action potential. Depolarization, repolarization, and their interaction," *Circulation Research*, vol. 68, pp. 1501–1526, 1991.
73. C. Luo and Y. Rudy, "A dynamic model of the cardiac ventricular action potential. I. Simulations of ionic currents and concentration changes," *Circulation Research*, vol. 74, pp. 1071–1096, 1994.
74. R. L. Winslow, J. J. Rice, S. Jafri, E. Marbán, and B. O'Rourke, "Mechanisms of altered excitation-contraction coupling in canine tachycardia-induced heart failure, II model studies," *Circulation Research*, vol. 84, pp. 571–586, 1999.
75. F. W. T. Shannon, "A mathematical treatment of integrated Ca dynamics within the ventricular myocyte," in *Biophysical Journal*, vol. 87, pp. 3351–3371, 2004.
76. Y. Shiferaw, M. A. Watanabe, A. Garfinkel, J. N. Weiss, and A. Karma, "Model of intracellular calcium cycling in ventricular myocytes," in *Biophysical Journal*, vol. 85, pp. 3666–3686, 2003.
77. Y. Shibukawa, L. Chilton, K. A. MacCannell, R. B. Clark, and W. R. Giles, "K+ currents activated by depolarization in cardiac fibroblasts," *Biophysical Journal*, vol. 88, pp. 3924–3935, 2005.
78. L. Chilton, S. Ohya, D. Freed, E. George, V. Drobic, Y. Shibukawa, K. A. MacCannel, Y. Imaizumi, R. B. Clark, M. C. Dixon, and W. R. Giles, "K+ currents regulate the resting membrane potential, proliferation, and contractile response in ventricular fibroblasts and myofibroblasts," *American Journal of Physiology - Heart and Circulatory Physiology*, vol. 288, pp. H2931–H2939, 2005.
79. G. Li, H. Sun, J. Chen, Y. Zhou, H. Tse, and C. Lau, "Characterization of multiple ion channels in cultured human cardiac fibroblasts," *PLoS ONE*, vol. 4, p. e7307, 2009.
80. K. A. McCannell, H. Bazzazi, L. Chilton, Y. Shibukawa, R. B. Clark, and W. R. Giles, "A mathematical model of electrotonic interactions between ventricular myocytes and fibroblasts," *Biophysical Journal*, vol. 92, pp. 4121–4132, 2007.
81. K. H. W. J. ten Tusscher, D. Noble, P. J. Noble, and A. V. Panfilov, "A model for human ventricular tissue," *American Journal of Physiology. Heart and Circulatory Physiology*, vol. 286, pp. H1573–89, 2004.
82. F. B. Sachse and J. A. Abildskov, "Electrophysiological modeling of cardiac fibroblasts and their interaction with myocytes," in *Proceedings BMES*, p. 235, 2006.
83. B. Hille, *Ionic channels of excitable membranes*. Sinauer Associates, 1992.
84. P. Kohl and D. Noble, "Mechanosensitive connective tissue: Potential influence on heart rhythm," *Cardiovascular Research*, vol. 32, pp. 62–68, 1996.
85. J. J. Torres, L. N. Cornelisse, E. G. A. Harks, W. P. M. v. Meerwijk, A. P. R. Theuvenet, and D. L. Ypey, "Modeling action potential generation and propagation in NRK fibroblasts," *American Journal of Physiology*, vol. 287, pp. C851–C865, 2004.
86. C. D. Werner, *Simulation der elektrischen Erregungsausbreitung in anatomischen Herzmodellen mit adaptiven zellulären Automaten*. PhD thesis, 2001.
87. R. Plonsey and R. C. Barr, "Mathematical modeling of electrical activity of the heart," *Journal of Electrocardiology*, vol. 20, pp. 219–226, 1987.
88. C. Henriquez and R. Plonsey, "A bidomain model for simulating propagation in multicellular cardiac tissue," in *Proc. of the Annual International Conference of the IEEE Engineering in Medicine and Biology Society*, vol. 4, p. 1266, 1989.
89. N. Sepulveda and J. Wikswo, "Bipolar stimulation of cardiac tissue using an anisotropic bidomain model," *The Journal of Cardiovascular Electrophysiology*, vol. 5, pp. 258–267, 1994.
90. C. Henriquez, A. Muzikant, and C. Smoak, "Anisotropy, fiber curvature and bath loading effects on activation in thin and thick cardiac tissue preparations: Simulations in a three-dimensional bidomain model," *The Journal of Cardiovascular Electrophysiology*, vol. 7, pp. 424–444, 1996.
91. K. Simelius, J. Nenonen, and B. M. Horacek, "Modeling cardiac ventricular activation," *International Journal of Bioelectromagnetism*, vol. 3, pp. 51–58, 2001.

92. L. Tung, *A bidomain model for describing ischemic myocardial d-c potentials.* PhD thesis, 1978.
93. M. Karl and Institute of Biomedical Engineering, *Time and memory efficient implementation of the cardiac bidomain equations.* PhD thesis, Karlsruhe, 2008.
94. V. Jacquemet and C. S. Henriquez, "Modelling cardiac fibroblasts: Interactions with myocytes and their impact on impulse propagation," *Europace*, vol. 9, pp. vi29–vi37, 2007.
95. V. Jacquemet and C. S. Henriquez, "Loading effect of fibroblast-myocyte coupling on resting potential, impulse propagation, and repolarization: insights from a microstructure model," *American Journal of Physiology*, vol. 294, pp. 2040–2052, 2008.
96. S. Zlochiver, V. Munoz, K. L. Vikstrom, S. M. Taffet, O. Berenfeld, and J. Jalife, "Electrotonic myofibroblast-to-myocyte coupling increases propensity to reentrant arrhythmias in two-dimensional cardiac monolayers," *Biophysical Journal*, vol. 95, pp. 4469–4480, 2008.
97. K. Tanaka, S. Zlochiver, K. L. Vikstrom, M. Yamazaki, J. Moreno, M. Klos, A. V. Zaitsev, R. Vaidyanathan, D. Auerbach, S. Landas, G. Guiraudon, J. Jalife, O. Berenfeld, and J. Kalifa, "The spatial distribution of fibrosis governs fibrillation wave dynamics in the posterior left atrium during heart failure," *Circulation Research*, vol. 101, pp. 839–847, 2007.
98. Y. Xie, A. Garfinkel, P. Camelliti, P. Kohl, J. N. Weiss, and Z. Qu, "Effects of fibroblast-myocyte coupling on cardiac conduction and vulnerability to reentry: A computational study," *Heart Rhythm*, vol. 6, pp. 1641–1649, 2009.
99. T. P. Nguyen, R. G. Xie, A. Garfinkel, Z. Qu, and J. N. Weiss, "Arrhythmogenic consequences of myofibroblast-myocyte coupling," *Cardiovascular Research*, 2011.
100. R. Yuste, *Fluorescence microscopy today*, vol. 2, pp. 905–909. Nat. Methods, 2005.
101. N. C. Conchello, P. A. Steinbach, and R. Y. Tsien, *A guide to choosing fluorescent proteins*, vol. 2, pp. 902–904. Nat. Methods, 2005.
102. J. A. Shaner and J. W. Lichtman, *Optical sectioning microscopy*, vol. 2, pp. 920–931. Nat. Methods, 2005.
103. S. Bolte and F. P. Cordelière, "A guided tour into subcellular colocalization analysis in light microscopy," *Journal of Microscopy*, vol. 224, pp. 213–232, 2006.
104. University of Bristol, "www.bristol.ac.uk," Apr. 2011.
105. P. Sarder and A. Nehorai, "Deconvolution methods for 3-D fluourescence microscopy images," *IEEE Signal Processing Magazine*, vol. 23, pp. 32–45, 2006.
106. P. Shaw, "Deconvolution in 3-D optical microscopy," *Histochemical Journal*, vol. 26, pp. 687–694, 1994.
107. G. Howard and M. Kaser, *Making and Using Antibodies.* CRC Press, 1st ed., 2007.
108. B. Alberts, *Molecular Biology of the Cell.* Garland Science, 4th ed., 2002.
109. Invitrogen, "Wheat Germ Agglutinin Conjugated. Product information."
110. SIGMA-ALDRICH, "Monoclonal Anti-Vimentin Cy3 Conjugate. Product information."
111. abcam, "Mouse monoclonal [CXN-6] to Connexin 43 / GJA1. Product information."
112. L. Moreno, D. Piniero, j. L. Sánchez, S. Manas, J. Merino, L. Acosta, and A. Hamilton, "Brain maturation estimation using neural classifier," *IEEE Transactions on Biomedical Engineering*, vol. 42, pp. 428–432, 1995.
113. abcam, "Mouse monoclonal [NC-17] to N Cadherin. Product information."
114. SIGMA-ALDRICH, "Monoclonal Anti-Actin, $\alpha$ Smooth Muscle. Product information."
115. Invitrogen, "DAPI Nucleic Acid Stain. Product information."
116. J. B. d. Monvel, S. L. Calvez, and M. Ulfendahl, "Image restoration for confocal microscopy: improving the limits of deconvolution, with application to the visualization of the mammalian hearing organ," *Biophysical Journal*, vol. 80, pp. 2455–2470, 2001.
117. W. H. Richardson, "Bayesian-based iterative method of image restoration," *Journal of the Optical Society of America*, vol. 62, pp. 55–59, 1972.
118. Nikon, "www.microscopyu.com," July 2011.
119. N. Hu, C. M. Straub, A. A. Garzarelli, K. H. Sabey, J. W. Yockman, and D. A. Bull, "Ligation of the left circumflex coronary artery with subsequent MRI and histopathology in rabbits.," *Journal of the American Association for Laboratory Animal Science*, vol. 49, pp. 838–844, 2010.
120. S. W. M. van den Borne, J. Diez, W. M. Blankesteijn, J. Verjans, L. Hofstra, and J. Narula, "Myocardial remodeling after infarction: The role of myofibroblasts," *Nature Reviews*, vol. 7, pp. 30–37, 2010.
121. J. G. Stinstra, B. Hopenfeld, and R. S. MacLeod, "On the passive cardiac conductivity," *Annals of Biomedical Engineering*, vol. 33, pp. 1743–1751, 2005.
122. K. R. Foster and H. P. Schwan, "Dielectric properties of tissues and biological materials: A critical review," *Critical Reviews in Biomedical Engineering*, vol. 17, pp. 25–104, 1989.

123. J. G. Stinstra and M. J. Peters, "The influence of fetoabdominal tissues on fetal ECGs and MCGs," *Archives of Physiology and Biochemistry*, vol. 110, pp. 165–176, 2002.
124. T. Matsuda, Y. Fujio, T. Nariai, T. Ito, M. Yamane, T. Takatani, K. Takahashi, and J. Azuma, "N-cadherin signals through Rac1 determine the localization of connexin 43 in cardiac myocytes," *Journal of Molecular and Cellular Cardiology*, vol. 40, pp. 495–502, 2006.
125. C. M. Hertig, S. Butz, S. Koch, M. Eppenberger-Eberhardt, R. Kemler, and H. M. Eppenberger, "N-cadherin in adult rat cardiomyocytes in culture. II. Spatio-temporal appearance of proteins involved in cell-cell contact and communication. Formation of two distinct N-cadherin/catenin complexes," *Journal of Cell Science*, vol. 109, pp. 11–20, 1996.
126. E. M. M. Manders, F. J. Verbeek, and J. A. Aten, "Measurement of co-localization of objects in dual-colour confocal images," *Journal of Microscopy*, vol. 169, pp. 375–382, 1993.
127. G. Rozanski, Z. Xu, R. Whitney, H. Murakami, and I. Zucker, "Electrophysiology of rabbit ventricular myocytes following sustained rapid ventricular pacing," in *Journal of Molecular and Cellular Cardiology*, vol. 29, pp. 721–732, 1997.
128. S. Rials, X. Xu, T. Liu, R. Marinchack, and R. R. Kowey, "Restoration of normal ventricular electrophysiology in renovascular hypertensive rabbits after treatment with losartan," in *Journal of Cardiovascular Pharmacology*, vol. 37, pp. 317–323, 2001.
129. I. Kodama, S. Shibata, T. J., and K. Yamada, "Electromechanical effects of Anthopleurin-A (AP-A) on rabbit ventricular muscle: Influence of driving frequency, calcium antagonists, Tetrodotoxin, Lidocaine and Ryanodine," in *British Journal of Pharmacology*, vol. 74, pp. 29–37, 1981.
130. X. Xu, S. Rials, Y. Wu, J. J. Salata, T. Liu, D. Bharucha, R. Marinchak, and P. Kowey, "Left ventricular hypertrophy decreases slowly but not rapidly activating delayed rectifier potassium currents of epicardial and endocardial myocytes in rabbits," in *Circulation*, vol. 103, pp. 1585–1590, 2001.
131. Z. Lu, K. Kamiya, T. Opthof, K. Yasui, and I. Kodama, "Density and kinetics of IKr and IKs in guinea pig and rabbit ventricular myocytes explain different efficacy of IKs blockade at high heart rate in guinea pig and rabbit: Implications for arrhythmogenesis in humans," in *Circulation*, vol. 104, pp. 951–956, 2001.
132. S. Pogwizd, K. Schlotthauer, L. Li, W. Yuan, and D. Bers, "Arrhythmogenesis and contractile dysfunction in heart failure : Roles of sodium-calcium exchange, inward rectifier potassium current, and residual $\beta$-adrenergic responsiveness," in *Circulation Research*, pp. 1158–1167, 2001.
133. M. J. Reiter, M. Landers, Z. Zetelaki, C. J. H. Kirchhof, and M. A. Allessie, "Electrophysiological effects of accute dilation in the isolated rabbit heart," *Circulation*, vol. 96, pp. 4050–4056, 1997.
134. Y. Tsuji, T. Opthof, K. Kamiya, K. Yasui, W. Liu, Z. Lu, and I. Kodama, "Pacing-induced heart failure causes a reduction of delayed rectifier potassium currents along with decreases in calcium and transient outward currents in rabbit ventricle," in *Cardiovascular Research*, vol. 48, pp. 300–309, 2000.
135. S. Pogwizd, M. Qi, W. Yuan, A. M. Samarel, and D. Bers, "Upregulation of Na+/Ca2+ exchanger expression and function in an arrhythmogenic rabbit model of heart failure," in *Circulation Research*, pp. 1008–1019, 1999.
136. C. Antzelevitch, S. Sicouri, S. H. Litovsky, A. Lukas, S. C. Krishman, J. M. D. Diego, G. A. Gintant, and D. W. Liu, "Heterogeneity within the ventricular wall: electrophysiology and pharmacology of epicardial, endocardial, and M-cells," *Circulation Research*, vol. 69, pp. 1427–1449, 1991.
137. J. L. Smeets, M. A. Allessie, W. J. Lammers, F. I. Bonke, and J. Hollen, "The wavelength of the cardiac impulse and reentrant arrhythmias in isolated rabbit atrium. The role of heart rate, autonomic transmitters, temperature, and potassium," *Circulation Research*, vol. 58, pp. 96–108, 1986.
138. J. H. Bridge, M. M. Bersohn, F. Gonzalez, and J. B. Bassingthwaighte, "Synthesis and use of radio cobaltic EDTA as an extracellular marker in rabbit heart," *American Journal of Physiology - Heart and Circulatory Physiology*, vol. 242, pp. H671–H676, 1982.
139. R. A. Lasher, R. W. Hitchcock, and F. B. Sachse, "Towards modeling of cardiac micro-structure with catheter-based confocal microscopy: A novel approach for dye delivery and tissue characterization," *IEEE Transactions on Medical Imaging*, vol. 28, pp. 1156–1164, 2009.
140. B. E. J. Teunissen, H. J. Hongsma, and M. F. A. Bierhuizen, "Regulation of myocardial connexins during hypertrophic remodelling.," *European Heart Journal*, vol. 25, pp. 1979–1989, 2004.
141. S. Rohr, "Cardiac fibroblasts in cell culture systems: Myofibroblasts all along?," *Journal of Cardiovascular Pharmacology*, vol. 57, pp. 389–399, 2011.
142. B. Hopenfeld, J. G. Stinstra, and R. S. Macleod, "Mechanism for ST depression associated with contiguous subendocardial ischemia," *Journal of Cardiovascular Electrophysiology*, vol. 15, pp. 1200–1206, 2004.

143. L. Clerc, “Directional differences of impulse spread in trabecular muscle from mammalian heart,” *Journal of Physiology*, vol. 255, pp. 335–346, 1976.
144. A. G. Kléber and C. B. Riegger, “Electrical constants of arterially perfused rabbit papillary muscle,” *Journal of Physiology*, vol. 385, pp. 307–324, 1987.
145. D. E. Roberts, L. T. Hersh, and A. M. Scher, “Influence of cardiac fiber orientation on wavefront voltage, conduction velocity and tissue resistivity in the dog,” *Circulation Research*, vol. 44, pp. 701–712, 1979.
146. P. E. Hand, B. E. Griffith, and C. S. Peskin, “Deriving macroscopic myocardial conductivities by homogenization of microscopic models,” *Bulletin of Mathematical Biology*, vol. 71, pp. 1707–1726, 2009.
147. D. E. Roberts and S. AM, “Effect of tissue anisotropy on extracellular potential fieds in canine myocardium in situ,” *Circulation Research*, vol. 50, pp. 342–351, 1982.
148. C. Vasquez, P. Mohandas, K. L. Louie, N. Benamer, A. C. Bapat, and G. E. Morley, “Enhanced fibroblast–myocyte interactions in response to cardiac injury,” *Circulation Research*, vol. 107, pp. 1011–1020, 2010.
149. J. Yao, W. Hussain, P. Patel, N. S. Peters, P. A. Boyden, and A. L. Wit, “Remodeling of gap junctional channel function in epicardial border zone of healing canine infarcts,” *Circulation Research*, vol. 92, pp. 437–443, 2003.